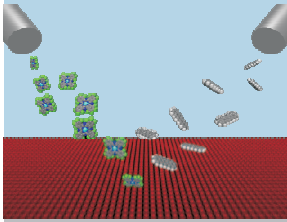
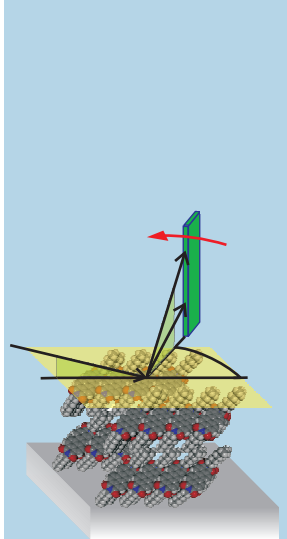
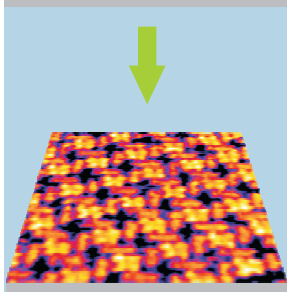


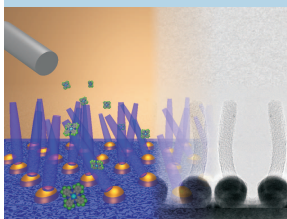
Directed Self-Assembly of Organic Semiconductors in Different Dimensionalities



Tobias N. Krauss
Stuttgart, 2009



Max-Planck-Institut
für Metallforschung
in Stuttgart



Institut für Theoretische
und Angewandte Physik
der Universität Stuttgart



Directed Self-Assembly of Organic Semiconductors in Different Dimensionalities

Von der Fakultät Mathematik und Physik der Universität Stuttgart
zur Erlangung der Würde eines Doktors der
Naturwissenschaften (Dr. rer. nat.) genehmigte Abhandlung

Vorgelegt von

TOBIAS NIKO KRAUSS

aus Stuttgart Bad-Cannstatt

Hauptberichter: Prof. Dr. Helmut Dosch
Mitberichter: Prof. Dr. Jörg Wrachtrup

Eingereicht am: 30.07.2009
Tag der mündlichen Prüfung: 18.09.2009

Institut für Theoretische und Angewandte Physik
der Universität Stuttgart
Max-Planck-Institut für Metallforschung
in Stuttgart

2009

Contents

1	Deutsche Zusammenfassung	v
1.1	Motivation	v
1.2	Experimentelle Ergebnisse	vi
1.2.1	3D Selbstaggregation von PTCDI-C ₈ -Mehrfachschichten auf schwach wechselwirkenden Oberflächen	vii
1.2.2	2D Selbstaggregation von Pentacen, F ₁₆ CuPc und deren gemischten Einzelschichten auf Kupfer (100)	ix
1.2.3	1D Selbstaggregation von Phthalocyanin-Derivaten	ix
1.3	Schlussfolgerungen	x
2	Motivation	1
3	Organic Semiconductors	5
3.1	Fundamentals of Thin Film Growth	6
3.1.1	Inorganic Thin Film Growth	6
3.1.2	Organic Thin Film Growth	9
3.2	Organic Semiconducting Molecules	11
3.2.1	PTCDI-C ₈	12
3.2.2	Phthalocyanines	13
3.2.3	Pentacene	18
4	Experimental Techniques	19
4.1	X-ray Scattering	19
4.1.1	X-ray Diffraction	20
4.1.2	X-ray Reflectivity	22
4.1.3	Grazing Incidence X-ray Diffraction	26
4.1.4	Synchrotron Radiation	27
4.2	Scanning Probe Microscopy	28
4.2.1	Scanning Tunneling Microscopy	28
4.2.2	Atomic Force Microscopy	32
4.3	Electron Microscopy	35
4.3.1	Transmission Electron Microscopy	36
4.3.2	Scanning Electron Microscopy	38

5	Experimental Details	41
5.1	Substrate Preparation	41
5.1.1	Al ₂ O ₃ (11 $\bar{2}$ 0) and Si(100)/SiO ₂	41
5.1.2	Si(100)/SiO ₂ modified by Au, Pt, and Pd nanoparticles	42
5.1.3	Cu(100)	43
5.1.4	Nanopatterned Gold Films	43
5.2	Organic Molecules	44
5.3	Organic Molecular Beam Deposition	44
5.3.1	Omicron UHV chamber	44
5.3.2	JEOL UHV chamber	46
5.3.3	Portable UHV chamber	47
5.4	AFM in Air	47
5.5	Synchrotron Beamlines	48
5.5.1	MPI-MF Surface Diffraction Beamline at ANKA	48
5.5.2	ID10B at the ESRF	49
6	3D Self-Assembly of PTCDI-C₈ Multilayer Films on Weak Interacting Surfaces	51
6.1	PTCDI-C ₈ on SiO ₂	52
6.1.1	Morphology and Growth Mode	52
6.1.2	Structure and Molecular Packing	53
6.1.3	Temperature Dependent Studies	60
6.2	PTCDI-C ₈ on Al ₂ O ₃	63
6.2.1	Structure and 3D Molecular Packing	64
6.2.2	Temperature Related Properties	72
6.3	Conclusions	72
7	2D Self-Assembly of Pentacene and F₁₆CuPc on Cu(100)	75
7.1	Self-Assembly of Pentacene	77
7.2	Self-Assembly of F ₁₆ CuPc	78
7.3	Self-Assembly of Pentacene and F ₁₆ CuPc in a Mixing Ratio 2:1	81
7.4	Conclusions	83
8	1D Self-Assembly of Phthalocyanine Derivatives	85
8.1	1D Self-Assembly of Phthalocyanine Derivatives on Gold Nanoparticles	86
8.1.1	Growth Mode and Structure	86
8.1.2	Influence of Particle Size and Shape	93
8.2	Role of the Gold Substrate	96
8.3	Influence of Substrate Temperature	98
8.4	How General Is This Phenomenon?	106
8.5	Conclusions	108

9 Summary and Outlook	111
A Transformation from Real Space to Reciprocal Space	115
B Correction Factors	117
B.1 Offset Scan and Footprint	117
B.2 Geometrical Correction Factors	118
C Relevant Parameters of the Fits	119
C.1 Fit Parameters of the PTCDI-C ₈ Multilayer Film on SiO ₂	119
C.2 Fit Parameters of the H ₁₆ CuPc Multilayer Film on SiO ₂ at Different T_{sub} .	120
D Atomic Form Factors	121
List of Publications	123
List of Symbols	125
References	129

1 Deutsche Zusammenfassung

1.1 Motivation

Als am 29. Dezember 1959 RICHARD P. FEYNMAN seine berühmte Rede vor der amerikanischen physikalischen Gesellschaft hielt und aussagte, dass viel Spielraum nach unten existiere, wusste noch niemand, was für ein Ausmaß an Veränderungen in Wissenschaft und Technik diese Vorhersage ein halbes Jahrhundert später mit sich bringen würde [1]. Mit der Erfindung des Rastertunnelmikroskops, für die BINNIG und ROHRER 1986 den Nobelpreis erhielten [2–4], erfuhr die Welt der Nanotechnologie schließlich einen rasante Entwicklung und spaltete sich rasch, aufgrund der vielseitigen Forschungsmöglichkeiten, in verschiedene Zweigbereiche auf. Einer dieser Zweigbereiche beschäftigt sich mit der Untersuchung organischer Halbleiter auf molekularer Längenskala.

Die halbleitenden Eigenschaften π -konjugierter organischer Moleküle wurden schon Mitte des letzten Jahrhunderts erforscht, ziehen aber erst in jüngerer Zeit ein großes Augenmerk auf sich. Dies ist auf ihre elektrischen und optischen Eigenschaften zurückzuführen, die zum ersten Mal erfolgreich Mitte der achtziger Jahre in organischen Solarzellen, organischen Feldeffekttransistoren und organischen Leuchtdioden angewendet wurden [5–7]. Die geringen Produktionskosten bei der Herstellung solcher Bauelemente (verglichen mit der Verwendung anorganischer Materialien) und ihre vielseitigen Einsatzmöglichkeiten auf unterschiedlichsten Oberflächen, wie zum Beispiel flexible Kunststoffe, tragen auch zu einem wachsenden Interesse in der Industrie bei.

Die wesentlichen Kernpunkte, die für eine Verbesserung der Leistung der oben erwähnten Bauelemente verantwortlich sind, beinhalten Wachstum, Struktur und Morphologie der verwendeten organischen Materialien. Sie bestimmen entscheidend die optischen und elektrischen Eigenschaften in den jeweiligen Bauteilen. Eine genaue Kontrolle des Wachs-

tumsverhaltens wie auch eine detaillierte Untersuchung der Strukturmerkmale organischer Halbleiter in verschiedenen Geometrien ist daher unerlässlich, um ein tieferes Verständnis der Zusammenhänge zwischen elektrooptischen und strukturellen Eigenschaften zu erlangen.

In dieser Arbeit wurde das Wachstum organischer Halbleiter, die unter Ultrahochvakuumbedingungen sublimiert wurden, analysiert. Ziel war es, ihre strukturellen Eigenschaften zu charakterisieren und die Wachstumsbedingungen zu optimieren, um hochgeordnete Nanostrukturen in drei, zwei und einer Dimension zu bilden, welche eine verbesserte Leistung in organischen Feldeffekttransistoren und organischen Solarzellen ermöglichen soll. Alle untersuchten Moleküle gehören zur Klasse der Aromaten und zeichnen sich durch π - π Wechselwirkungen aus, die für die Selbstaggregation in kristallinen Strukturen verantwortlich sind. Die Kontrolle der kinetischen Parameter, wie auch die Verwendung modifizierter Substrate wurde neben der eben erwähnten Fähigkeit der Selbstaggregation in dieser Arbeit ausgenutzt. Unter Einsatz komplementärer experimenteller Techniken wie Röntgenreflektivität, Röntgenbeugung unter streifendem Einfall, Rasterkraft- und Rastertunnelmikroskopie sowie Raster- und Transmissionselektronenmikroskopie wurden die strukturellen Eigenschaften der untersuchten Systeme aufgedeckt.

1.2 Experimentelle Ergebnisse

Die experimentellen Ergebnisse lassen sich gemäß ihrer Dimensionalität in drei Kategorien einteilen:

- Die Untersuchung der dreidimensionalen (3D) Selbstaggregation von PTCDI-C₈-Mehrfachschichten auf schwach wechselwirkenden Oberflächen.
- Die Untersuchung der zweidimensionalen (2D) Selbstaggregation von Pentacen, F₁₆CuPc und deren gemischten Einzelschichten auf einer (100) orientierten Kupferoberfläche.
- Die Untersuchung eindimensionaler (1D) Selbstaggregation von Phthalocyanin-Derivaten.

1.2.1 3D Selbstaggregation von PTCDI-C₈-Mehrfachschichten auf schwach wechselwirkenden Oberflächen

Da die meisten aromatischen Moleküle p-Halbleitereigenschaften besitzen, das heißt, dass die Mehrheit der Ladungsträger durch Löcher bereit gestellt wird, ist es notwendig, organische n-Halbleiter zu untersuchen, um die Herstellung organischer ambipolarer Transistoren, organischer Leuchtdioden oder organischer Solarzellen zu ermöglichen [6, 8, 9]. PTCDI-C₈ ist einer der wenigen n-Halbleiter, der außerdem noch eine sehr hohe Ladungsträgerbeweglichkeit vorweisen kann [10, 11]. Um die Ursache einer solch hohen Ladungsträgerbeweglichkeit zu ermitteln, bedarf es einer umfassenden Analyse der Morphologie und der 3D Struktur in Dünnschichten auf technologisch relevanten Substraten wie zum Beispiel Siliziumdioxid oder Aluminiumoxid [12, 13], was bisher nicht geschehen war.

Die detaillierte Strukturanalyse von PTCDI-C₈ Dünnschichten auf Siliziumdioxid zeigt eine schiefwinklige Einheitszelle parallel zur Oberflächenebene auf. Ein Modell für die Molekülorientierung entlang der Oberflächennormalen wird vorgeschlagen, welches eine geneigte Konfiguration des PTCDI-C₈ Moleküls bezüglich der Oberflächenebene beinhaltet. Das Modell schließt auch mit ein, dass Alkylketten benachbarter PTCDI-C₈ Moleküle nicht ineinander greifen, im Gegensatz zu PTCDI-C₁₈, wo solch eine Verzahnung berichtet wurde [14]. Zudem wurde herausgefunden, dass die oberste Lage der Filmstruktur eine kleinere Dicke besitzt als die Lagen darunter, was auf eine größere Neigung der Alkylketten weg von der Oberflächennormalen zurückzuführen ist, um den Verlust an Kohäsionsenergie an der Grenzschicht organischer Halbleiter/Luft auszugleichen. Die Erhöhung der Substrattemperatur resultiert in einer weniger rauen Filmoberfläche mit einer Vergrößerung der nadelförmigen Terrassen. Die Domänengröße, die für den PTCDI-C₈ Film bei Raumtemperatur bestimmt wurde, ist erheblich kleiner als die Insel- und Korngröße, die mittels Rasterkraftmikroskopie beobachtet wurde. Darüber hinaus deuten die ähnlichen Breiten der (100) und (010) Bragg-Peaks auf ein eher isotropes Wachstumsverhalten entlang der unterschiedlichen kristallographischen Richtungen hin, was sich von der Erwartung eines schnelleren Wachstums entlang der π - π -Stapelrichtung, das heißt entlang der [010] Richtung, deutlich unterscheidet. Zusätzlich lässt sich feststellen, dass sich mit zunehmender Substrattemperatur die Inselgröße ausdehnt, jedoch die kristallinen Domänen in lateraler Richtung keine maßgeblichen Veränderungen vorweisen. Schließlich zeigt sich noch, dass ein Erhöhen der Substrattemperatur nach dem Wachstumsvorgang

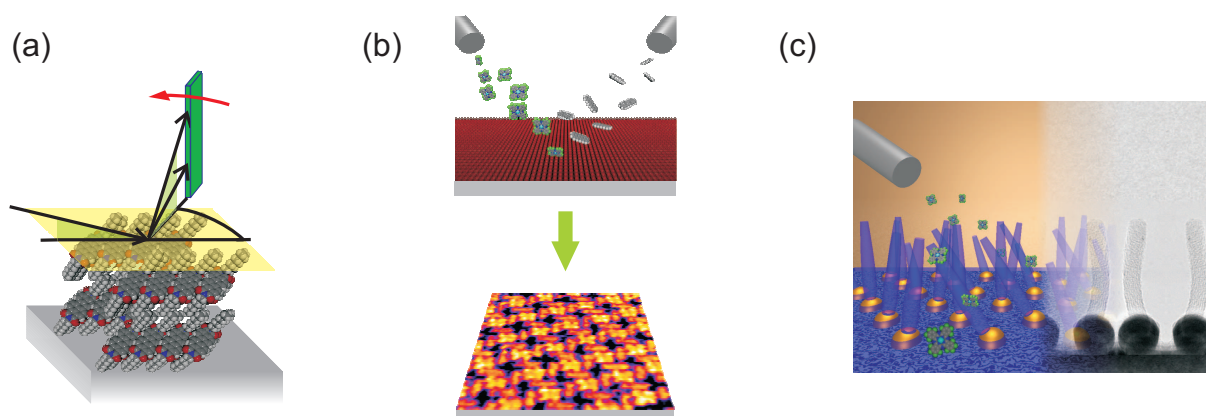


Abbildung 1.1: (a) Schema der Geometrie, die angewandt wurde, um die vollständige Strukturanalyse von PTCDI- C_8 Filmen auf Aluminiumoxid durchzuführen. (b) Schema des Koevaporationsprozesses für die gemischte Einzelschicht bestehend aus Pentacen und $F_{16}CuPc$ Molekülen. Darunter sieht man die hochgeordnete Monolage, die sich bei einem Molekülverhältnis von 2:1 (Pentacen: $F_{16}CuPc$) ausbildet. (c) Schema der Deposition von Phthalocyanin-Molekülen auf einem mit Goldnanopartikel bedeckten Substrat zusammen mit einer Transmissionselektronenmikroskopie-Aufnahme, die das Wachstum von 1D $H_{16}CoPc$ -Strukturen auf den Goldnanopartikeln anschaulich darlegt.

zu einem höheren Ordnungsgrad in der Filmstruktur führt.

Die komplette Bestimmung der Struktur und des molekularen Arrangements innerhalb von Dünnschichten stellt sich als nicht so einfache Aufgabenstellung dar, wie zum Beispiel die Durchführung und Analyse von Pulveraufnahmen, welche heutzutage schon eine etablierte Technik ist. Die Schwierigkeit liegt darin, dass organische Filme meist in der Oberflächenebene ein polykristallines Pulver ausbilden, aber senkrecht zur Oberfläche strukturiert sind. Daher wird hier, anhand von PTCDI- C_8 Filmen auf Aluminiumoxid, ein Weg aufgezeigt, wie man eine vollständige Strukturanalyse in Dünnschichten realisieren kann. Die trikline Einheitszelle, welche ein Molekül enthält, wurde mit Hilfe der Röntgenbeugung unter streifendem Einfall in Kombination mit einem Lineardetektor ermittelt, was in Abbildung 1.1 (a) schematisch veranschaulicht ist. Das Betragsquadrat des Strukturfaktors wurde als Funktion der möglichen Rotationen des PTCDI- C_8 Moleküls innerhalb der Einheitszelle simuliert und mit den experimentell gemessenen Daten verglichen. Aus der besten Übereinstimmung zwischen Modell und Experiment ergab sich, dass die Ebene, in die der aromatische Kern des Moleküls liegt, bezüglich der Oberflächenebene geneigt ist und dass die PTCDI- C_8 Moleküle sich entlang des b -Basisvektors stapeln. Ferner wurde eine vertikale Kohärenzlänge der Multilagen ermittelt, die mit der

Filmdicke übereinstimmt. Dies lässt darauf schließen, dass die 3D Kristallite sich über die ganze Dicke der Dünnschichtstruktur erstrecken.

1.2.2 2D Selbstaggregation von Pentacen, $F_{16}CuPc$ und deren gemischten Einzelschichten auf Kupfer (100)

Die fortschreitende Miniaturisierung in der Mikroelektronik und der Datenspeicherung erfordert neue Strategien, um diesen Trend aufrecht zu erhalten. Eine Möglichkeit bietet die Nanotechnik, in der sogenannte bottom-up (von unten nach oben) Nanostrukturen mit Hilfe der molekularen Selbstaggregation erzeugt werden [15,16]. Organische Moleküle repräsentieren hier wieder eine vielversprechende Klasse als Bausteine für Nanomaterialien mit neuartigen Funktionsweisen basierend auf dem Prinzip der Selbstaggregation. Im Rahmen dieser Arbeit wurde die Selbstaggregation von Pentacen, $F_{16}CuPc$ und deren gemischten Einzelschichten auf einer (100) orientierten Kupferoberfläche mit Hilfe der Rastertunnelmikroskopie untersucht [17]. Aufgrund seiner hohen Ladungsträgerbeweglichkeit ist Pentacen bisher der wichtigste p-Halbleiter. $F_{16}CuPc$ ist eines der wenigen Moleküle, die stabile n-Halbleitereigenschaften in organischen Transistoren unter Luft vorweisen können. Kupfer (100) wurde gewählt, da es häufig als Kontaktmaterial in organischen Bauelementen eingesetzt wird. Es konnte gezeigt werden, dass gemischte Monolagen von Pentacen und $F_{16}CuPc$ hochgeordnete 2D supramolekulare Strukturen bilden (wie schematisch in Abbildung 1.1 (b) dargestellt), begünstigt durch zwischenmolekulare Wechselwirkungen. Ein kristallines, nanoporöses Netzwerk wurde bei einem Mischverhältnis von 2:1 zwischen Pentacen und $F_{16}CuPc$ beobachtet. Die gemischte wie auch die reine $F_{16}CuPc$ -Monolage zeigten beide zwei enantiomorphe, chirale Domänen mit hohem Ordnungsgrad, im Gegensatz zu Pentacen-Einzelschichten, bei denen kein langreichweitiges Ordnungsverhalten vorgefunden wurde. Ein Modell wurde entwickelt, um die epitaktische Relation der gemischten wie auch der reinen $F_{16}CuPc$ -Einzelschichten mit dem Substrat zu bestimmen. C-F...H Bindungen werden als plausible Antriebskraft für die bimolekulare Selbstaggregation vorgeschlagen.

1.2.3 1D Selbstaggregation von Phthalocyanin-Derivaten

Die wiederholte Reduzierung der Dimensionalität von 2D zu 1D führt schließlich zum letzten Teil dieser Arbeit. Es wurden abermals die Eigenschaften der aromatischen Mo-

leküle zur Selbstaggregation ausgenutzt, jedoch nun in Verbindung mit dem Einsatz von mit Nanopartikeln bedeckten Substraten, um 1D vertikale Strukturen hervorzurufen [18]. Dieses höchst selektive 1D Wachstumsphänomen konnte für verschiedene Phthalocyanin-Derivate ($H_{16}CuPc$, $H_{16}CoPc$, $F_{16}CoPc$ and $F_{16}CuPc$) nachgewiesen werden, wie auch in Abbildung 1.1 (c) ersichtlich [19]. Neben flachen Nanobandstrukturen wurden Nanodräh- te auf mit Goldnanopartikeln modifizierten Siliziumdioxid- und Siliziumnitrid-Substraten beobachtet, deren monokristalline Nanostrukturen mittels Transmissionselektronenmikro- skopie aufgelöst werden konnten. Eine statistische Auswertung der Goldnanopartikel lie- ferte die Erkenntnis, dass ein minimaler Durchmesser nötig ist, um einen 1D Wachstums- modus auszulösen. Darüber hinaus konnte gezeigt werden, dass anstelle von Goldnano- partikeln, auch polykristalline Goldfilme ein 1D Wachstumsverhalten bewirken können, sofern ausreichend kleine Körner vorhanden sind. Somit bietet die Strukturierung von Siliziumsubstraten mit polykristallinen Goldinseln eine alternative Methode, um die Bil- dung eindimensionaler Strukturen herbeizuführen. Der Einfluss der Substrattemperatur auf das Wachstum wurde mit Hilfe der Raster- und Transmissionselektronenmikroskopie in Kombination mit Röntgenreflektivität ermittelt. Es wurde beobachtet, dass die Dicke der organischen Benetzungsschicht (die bei beliebiger Substrattemperatur vorhanden ist) mit wachsender Substrattemperatur abnimmt, wohingegen die Länge der 1D Strukturen zu- nimmt. Wiederum wurde ein Modell entworfen, um diesen komplexen Wachstumsprozess zu beschreiben, das auch die organische Benetzungsschicht um die Goldnanopartikel mit berücksichtigt, deren Dicke ebenso von der Substrattemperatur abhängt. Schließlich wur- de noch getestet, wie allgemein dieses Wachstumsverhalten ist, indem Indiumzinnoxid- anstelle von Siliziumdioxid-Substrate eingesetzt wurden, die entscheidend für die Her- stellung organischer Solarzellen sind. Auch hier konnten die 1D Strukturen erfolgreich reproduziert werden.

1.3 Schlussfolgerungen

Es wurde eine umfangreiche Strukturanalyse von PTCDI- C_8 Dünnschichten auf Silizi- umdioxid durchgeführt. Bei allen gemessenen Substrattemperaturen konnte beobachtet werden, dass PTCDI- C_8 Dünnschichten geringer Rauigkeit bildet, in denen die Moleküle sich in einer schiefwinkligen Einheitszelle anordnen und sich entlang des b -Basisvektors stapeln. Die Einheitszelle in der Ebene und der errechnete Neigungswinkel legen eine

Filmstruktur offen, die derer auf Aluminiumoxid sehr ähnlich ist. Zusätzlich wurde gezeigt, dass eine geeignete Substrattemperatur während des Wachstumsvorgangs gefolgt von einem nachträglichen Erhitzen des Substrats zu der am höchst geordneten Multilage führt. Dies lässt darauf schließen, dass die Ladungsträgerbeweglichkeit und somit auch die Leistung organischer Feldeffekttransistoren unter solchen Bedingungen verbessert werden. Schlussendlich deuten die ermittelten Resultate darauf hin, dass eine weitere Steigerung der Funktionsfähigkeit organischer Feldeffekttransistoren nicht allein von der Ausdehnung der lateralen Kristallitgröße abhängt, sondern auch von der drastischen Verringerung der Anzahl an Korngrenzen.

Auf Aluminiumoxid wurde eine Methode aufgezeigt, wie man die Informationen der vollständigen 3D Struktur inklusive der Molekülpackung allgemein in Dünnschichten und speziell von PTCDI-C₈ Multilagen gewinnen kann. Die trikline Einheitszelle, die ein PTCDI-C₈ Molekül beinhaltet, unterscheidet sich merklich von der Festkörperstruktur nadelförmiger PTCDI-C₈ Kristalle [20]. Der Moleküllern ist gegenüber der Oberflächennormalen geneigt und weist einen zwischenmolekularen Abstand benachbarter PTCDI-C₈ Moleküle von 3.58 Å entlang der π - π Stapelrichtung auf, die in Richtung des b -Basisvektors verläuft. Dies führt zu der Erkenntnis, dass man eine größere Überlappung der molekularen π - π Orbitale, die für den Ladungstransport ausschlaggebend sind, entlang der kristallographischen [010] Richtung erwarten kann. Die Bestimmung der Molekülpackung wie auch die vollständige 3D Struktur sind Schlüsselparameter, um die damit verbundene elektronische Bandstruktur zu berechnen, die dann wiederum eine Simulation des Ladungstransportes in organischen Feldeffekttransistoren erlaubt. Dies ist einer der wesentlichen Schritte, um letztendlich eine Kontrolle der elektrischen Eigenschaften polykristalliner organischer Dünnschichten zu erhalten.

Die Adsorption von Pentacen und F₁₆CuPc auf Kupfer (100) führt zu einem 2D kristallinen, nanoporösen Netzwerk mit Lücken von ungefähr 8 Å im Durchmesser. Die hier vorgestellte supramolekulare Selbstaggregation bietet nicht nur die Gelegenheit, regelmäßige 2D Nanostrukturierungen bestehend aus mehreren Komponenten herzustellen, sondern ermöglicht auch, die nanoporöse Matrix als Komplexbildung mit weiteren Verbindungen auszunutzen und geordnete 3D Architekturen zu kreieren. Es wurde offengelegt, dass intermolekulare C-F...H Wechselwirkungen zwischen beiden Molekülen die gemischten Monolagen begünstigen, wohingegen die Molekül-Substrat Wechselwirkungen die Orientierung der einzelnen Moleküle diktiert. Die langreichweitige Ordnung der

F₁₆CuPc-Pentacen Struktur gegenüber der kurzreichweitigen Ordnung der reinen Pentacenschichten zeigt eindrucksvoll, wie das Zusammenspiel zwischen intermolekularen und Molekül-Substrat Wechselwirkungen die Selbstaggregationseigenschaften supramolekularer Strukturen beeinflussen und bestimmen kann.

Das Wachstum von 1D Strukturen auf mit Goldnanopartikeln bedeckten Substraten ist ein allgemeiner Prozess für Phthalocyanin-Derivate. Solch ein selektives 1D Wachstum findet jedoch nicht für andere Moleküle mit anisotropem Wachstumsverhalten, wie zum Beispiel PTCDI-C₈ oder para-Sexiphenyl statt, was darauf schließen lässt, dass diese Erscheinungsform der Selbstaggregation speziell Phthalocyanin-Verbindungen zuzuschreiben ist. Die Möglichkeit, 1D organische monokristalline Strukturen mit präziser Ortsbestimmung und einstellbaren Ausdehnungen von sowohl n- als auch p-Halbleitern herzustellen, ermöglicht die bottom-up Fabrikation neuartiger Nanobauteile. Insbesondere besteht jetzt die Chance, durch das sequenzielle Aufdampfen von p- und n-Halbleitern, eine Art Kammstruktur zu bilden, die Ladungsträger höchst effizient einsammelt und eine hohe Ausbeute an gebildeten Exzitonen garantiert, was schließlich zu einer verbesserten Leistungsfähigkeit in nanostrukturierten Solarzellen führt.

2 Motivation

On December the 29th 1959, RICHARD P. FEYNMAN gave his famous talk in the annual meeting of the American Physical Society stating that there is plenty of room at the bottom [1]. The prediction he made should not only change science and technology but even our everyday lives in a tremendous way on condition that we would gain insight in how to control matter down to the atomic level. In 1989 finally, it was demonstratively shown how to manipulate surfaces with atomic precision by positioning individual xenon atoms on a single-crystal nickel substrate with the help of a scanning tunneling microscope tip [21]. Since then, the field of nanotechnology has undergone rapid progress and split into many different branches including the investigation of organic semiconductors on a molecular length scale.

Organic semiconductors have been studied since the late 1940s but the starting point of organic electronics can be set at the mid 1980s where organic materials were for the first time implemented into organic photovoltaic cells (OPVs), organic light emitting diodes (OLEDs) and organic field effect transistors (OFETs) [5–7]. The most appealing advantages, when compared to their inorganic counterparts, are that organic materials offer an inherent compatibility with plastic substrates, flexibility since the bonding between adjacent atoms in organic molecules is governed by van-der Waals forces, and amenability to low-cost and low-temperature processing methods such as melt processing, printing, and solution deposition [22–24]. The high demand for lightweight and inexpensive electronic components has therefore triggered an extensive research activity in the field of organic semiconductors.

Key aspects in manufacturing OPVs, OLEDs and OFETs with a high device performance are the growth, structure and morphology of the organic semiconducting material since they determine the optical and electrical characteristics of the respective applica-

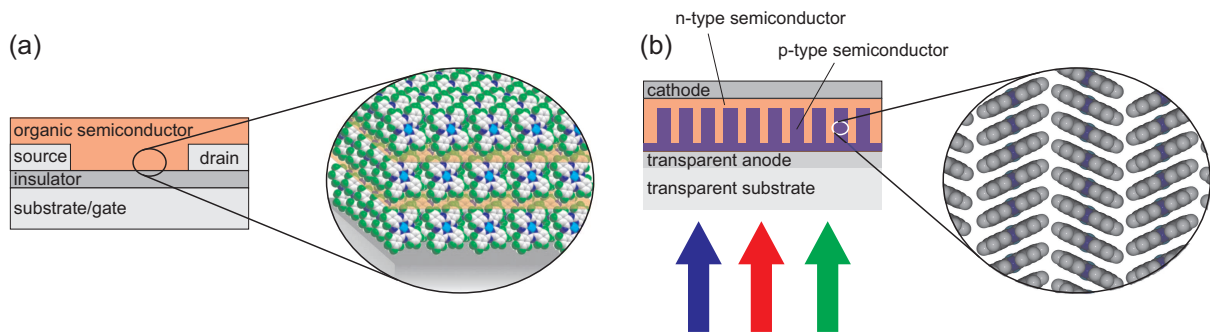


Figure 2.1: (a) Scheme of a typical bottom contact OFET geometry with a zoom into the active layer. A single crystalline organic film represents the ideal case for an optimum charge transfer. (b) Simplest layout of an organic photovoltaic cell consisting of a comb-shaped active layer with a zoom into one of the wire-like 1D structures. The architecture of such an active layer guarantees a large interfacial area to create and harvest as many excitons as possible. Furthermore, the 1D structures are supposed to form highly crystalline structures.

tion. The importance of this three properties shall be elucidated shortly with two simple examples. OFETs require high charge carrier mobility which turned out to be one of the major problems of organic semiconductors. In a thin film geometry, the charge carrier mobility of an OFET depends crucially on the structural order of the active (organic semiconducting) film and on the morphology and structure of the first organic layers at the organic/inorganic interface. Here, single crystalline films where the intermolecular overlap of electronic π -orbitals of adjacent molecules is maximized, as can be seen schematically in Figure 2.1 (a), represents the ideal case for an optimum charge carrier transport [23,25,26]. However, in applications such as OPVs where organic n- and p-type materials are mixed, the architecture and structure at the organic/organic interface plays a pivotal role in the device efficiency in addition to the forecited issues. From theoretical simulations as well as from experimental measurements it seems that a comb-shaped architecture of the active layer, as depicted in Figure 2.1 (b), is a promising avenue to improve the efficiency in OPVs [8,27]. A large interfacial area between p- and n-type material is provided to create and harvest as many excitons (electron-hole pairs) as possible. In addition, if the one dimensional (1D) structures are crystalline, this architecture guarantees a good charge carrier transport to the electrode.

To summarize, it can be seen that different devices face different needs for an optimum performance which can only be fulfilled by a precise control of the growth mode and a detailed characterization of the structural properties. Hence, it is crucial to gain profound

understanding in the growth and self-assembly mechanism of organic semiconductors on surfaces presenting one of the open issues of great technological interest.

In this experimental work, the growth of organic semiconductors by sublimation in ultra high vacuum was studied. The aim was to characterize structural properties and optimize growth conditions in order to attain highly ordered architectures in three, two and one dimension for an improved and suitable implementation into devices. The molecules studied in this thesis exhibit π - π interactions which are a driving force for the self-assembly in crystalline structures. This ability was exploited together with the control of kinetic parameters and the templating role of substrates. Precise information of the structural properties for each system has been achieved by the combination of various complementary techniques including x-ray reflectivity, grazing incidence x-ray diffraction, atomic force and scanning tunneling microscopy and scanning and transmission electron microscopy.

PTCDI-C₈ was investigated in chapter 6 not only because of its increased attention as one of the few n-type semiconductors but also due to the high charge carrier mobility reported recently [10,11]. To understand the origin of such a high charge carrier mobility makes it essential to unravel its morphology, three dimensional (3D) structure and molecular packing in thin films on technologically relevant substrates such as silicon dioxide or aluminum oxide, which was up to now still unknown [12,13]. However, the analysis of the structure and molecular arrangement within organic films is not as straightforward as for example in powder diffraction which is a well established technique nowadays. Organic films order in a powder fashion in plane but are textured perpendicular to the surface. Thus, a possible route is pointed out which can be applied to tackle the general problem of a full structure analysis in thin films [13].

In chapter 7, the self-assembly of pentacene, F₁₆CuPc and mixed supramolecular structures of these compounds were investigated by scanning tunneling microscopy in a two dimensional (2D) system to disclose the driving force in the growth process [17]. Pentacene still represents one of the most important p-type semiconductors whereas F₁₆CuPc is one of the few air stable n-type semiconductors. It is demonstrated how the interplay between intermolecular and molecule-substrate interactions can tune and dictate the self-assembly properties of supramolecular structures. Furthermore, it is shown that the supramolecular self-assembly of the 2D binary structures opens the avenue to nanoporous templates with potential for the complexation of other molecular species.

Reducing the dimensionality once more from 2D to 1D leads finally to chapter 8. Here, self-assembly properties of aromatic molecules were exploited in combination with templates of nanoparticles to induce vertical 1D structures. This highly selective 1D growth phenomenon could be proven for different derivatives of the phthalocyanine family [19]. Monocrystalline, upright standing nanowires were observed on gold nanoparticles which might be promising candidates for an implementation into organic solar cells as described before. The role of the gold nanoparticles in this growth mode was studied more thoroughly and extended to an analysis of phthalocyanines on patterned surfaces of gold islands and polycrystalline gold films. In addition, light was shed on the diffusion process and the kinetics as a function of the substrate temperature during growth.

This thesis shows bottom-up approaches by directing the self-assembly process of conjugated molecules in different dimensions through kinetic control and by the use of nanostructured surfaces. In doing so, various morphologies of organic semiconductors are tailored with the objective of improving and optimizing specific organic devices.

3 Organic Semiconductors

Organic semiconductors are materials based on molecules containing carbon compounds. They only become conductors of electric current when excess charge carriers are either produced by the internal photo effect or are injected by applied voltages. Their semiconducting properties are attributed to the conjugated π -electron systems in their skeletal structures which is a consequence of sp^2 hybridization of the carbon atoms: the p_x and p_y orbitals are forming together with the s orbital the σ bonds and are localized between the carbon bonding atoms. The p_z orbitals of adjacent atoms, however, overlap perpendicular to the plane of the sp^2 orbitals and form an additional bond, the π bond as illustrated in Figure 3.1.

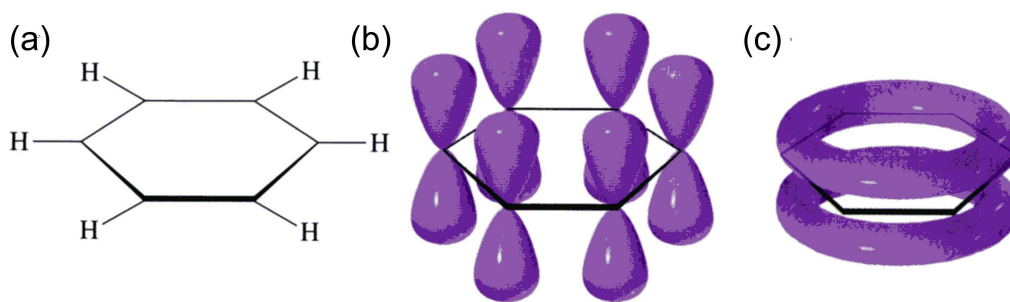


Figure 3.1: (a) The σ bonds of benzene. (b) p_z orbitals on each carbon atom of benzene which can overlap with two adjacent p_z orbitals. (c) The resulting electron cloud of π electrons above and below the plane of the benzene ring (from Ref. [28])

Due to the weak contribution of the π electrons to bonding of the molecule, the conjugated π -electron system exhibits electronic excitation energies in the range of only a few eV and is therefore responsible for the optoelectronic properties of organic semiconductors. In contrast to inorganic semiconductors, where the band gap extends between valence and conduction band, is the gap in organic semiconductors determined by the difference between the highest occupied molecular orbital (HOMO) and the lowest unoccupied molecular orbital (LUMO). This band gap can be varied to a certain extent by synthesizing diverse molecules which differ in size, atomic arrangement and functional groups in order to tune their electronic properties.

Basically, organic semiconducting molecules can be classified into two main groups: polymers and oligomers. Polymers are long flexible molecules which are characterized by the formation of unbounded repetitive molecular units. Oligomers or small weight organic molecules consist of a finite number of monomer units thus leading to a well defined mass (in contrast to polymers). Both, polymers and oligomers show similar electronic and optical properties with typical energy band gaps between 1.5 eV to 2.6 eV. The major difference is found in the thin film deposition techniques and in the resulting structural properties. Polymers can be easily processed from solution which decreases the production costs dramatically. Oligomers, however, are very often insoluble and techniques using ultra high vacuum (UHV) are required which are associated with higher costs. Nevertheless, oligomers have the crucial advantage over polymers that they allow the preparation of very well ordered films of high purity and crystalline order, two fundamental prerequisites to enhance charge carrier mobility.

3.1 Fundamentals of Thin Film Growth

3.1.1 Inorganic Thin Film Growth

For an implementation into devices, semiconductors (inorganic as well as organic) require a substrate and are therefore deposited in thin films on a surface. This process can be generally classified as heteroepitaxial growth since the substrate material is in this case not equal to the film material, in contrast to homoepitaxial growth where the substrate and the film are composed of the same material. Not only the choice of substrate and the deposition technique are key aspects which influence the film characteristics but also

experimental parameters as for instance substrate temperature and deposition rate. Extensive experimental and theoretical research has solidified a well-established theory of inorganic growth. In the literature, two theoretical approaches can be found which try to describe thin film growth. One uses a thermodynamic ansatz assuming that film growth takes place close to thermodynamic equilibrium whereas the second is based on kinetic considerations. In what follows is a short introduction in both formalisms [29–31].

BAUER tried to explain and predict the growth modes in terms of surface energies and distinguishes between three scenarios [32]. The first one is the so called Frank-van der Merwe or layer-by-layer growth. Here, one monolayer has to be completely covered upon adsorption of the next layer as demonstrated in Figure 3.2 (a). The second scenario is shown in Figure 3.2 (b) corresponding to island or Vollmer-Weber growth where new atomic or molecular layers are formed before completion of the underlying layers. Finally, Figure 3.2 (c) illustrates a combination of layer- and island growth which is defined as Stranski Krastanov growth. Here, after a critical thickness, islands start to grow on complete layers which is a result of induced strain due to a lattice mismatch between

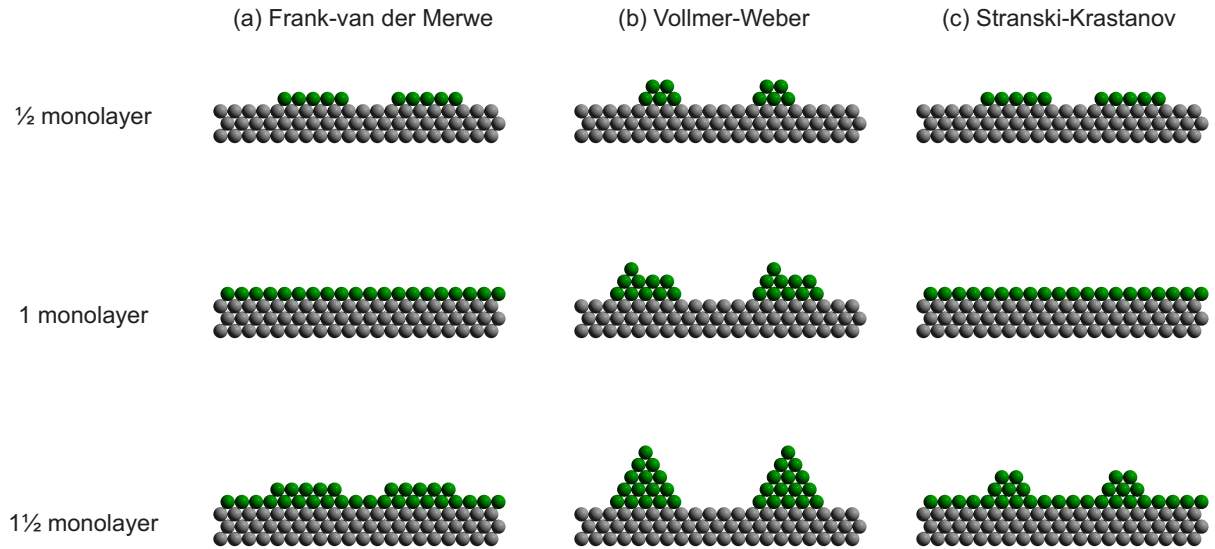


Figure 3.2: Schematic illustration of the three different growth modes: (a) layer-by-layer or Frank-van der Merwe growth, (b) island or Vollmer-Weber growth, (c) layer-plus-island or Stranski-Krastanov growth.

substrate and film. These various growth modes can be understood by taking a look at the involved surface energies. The substrate-vacuum (γ_{sv}), the film-substrate (γ_{fs}) and the film-vacuum (γ_{fv}) surface energies are related in thermodynamic equilibrium via

$$\gamma_{sv} \geq \gamma_{fv} + \gamma_{fs} \quad (3.1)$$

for Frank-van der Merwe growth. For Vollmer Weber growth is the formation of atomic or molecular islands energetically more favorable, thus resulting in the condition

$$\gamma_{sv} < \gamma_{fv} + \gamma_{fs}. \quad (3.2)$$

In the Stranski-Krastanov growth mode, the strain generated in the wetting layers of the thin film contributes to the film-substrate interface energy γ_{fs} . Therefore, there is a steady increase of energy for increasing film thickness until the aforementioned critical thickness where $\gamma_{sv} < \gamma_{fv} + \gamma_{fs}$. Here, the growth undergoes now a transition from layer-by-layer to island growth. A precise control of Stranski Krastanov growth in heteroepitaxial systems of semiconductors has also led to the fabrication of nanostructures with novel functional properties as for instance quantum dots.

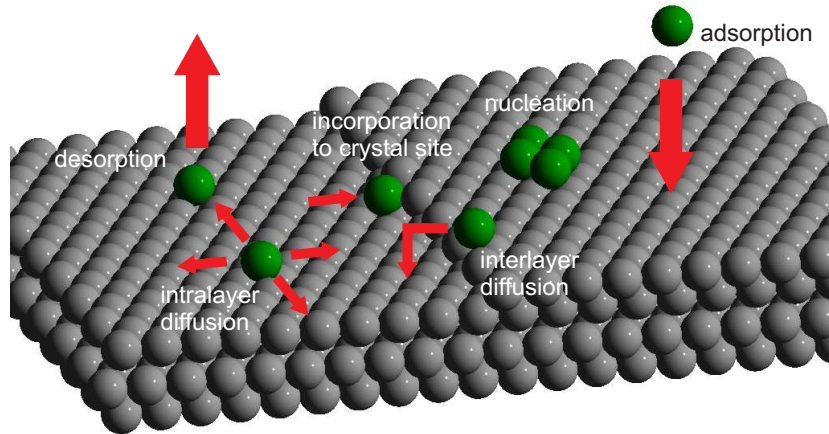


Figure 3.3: Elementary growth processes including adsorption of atoms on the surface, inter- and intralayer diffusion, island nucleation, incorporation to crystal sites and desorption.

All considerations made above are only applicable to systems in thermodynamic equilibrium. However, strictly speaking growth is always a non-equilibrium phenomenon. Here, a kinetic ansatz has to be done which takes several atomic processes into account occurring during film growth (see Figure 3.3): adsorption of an atom onto the surface, lateral diffusion of an adatom on the surface including a possible step crossing, incorporation of an adatom to a crystal site, nucleation with further adatoms or re-evaporation. Each of these processes are ascribed to a characteristic energetic barrier which is a material specific property. These energetic barriers along with the kinetic parameters of flux and temperature finally determine the growth mode and film morphology.

3.1.2 Organic Thin Film Growth

The introduction made in the previous section applies to inorganic thin film systems. However, there are intrinsic properties of organic materials which make these growth scenarios more complex [35, 36].

First, organic molecules are extended and anisotropic objects giving rise to internal degrees of freedom. The orientational degrees of freedom which are not included in conventional growth models can trigger new growth scenarios such as a change of molecular orientation within adjacent molecular layers (see Figure 3.4). This was shown in a recent work by HLAWACEK and co-workers and illustrates demonstratively that growth theories that are well known and verified in inorganic growth have to be reconsidered and modified for organic growth [37]. Beside the orientational degrees of freedom, organic molecules possess also vibrational degrees of freedom which can influence the substrate-film interaction and their diffusion behavior.

Second, the interaction potential between molecules and molecule and substrate is anisotropic. The interaction between organic molecules is dictated by van-der Waals interactions with contributions of other non-covalent interactions (H-bonding, π - π and dipolar interactions) in presence of certain functional groups. As direct consequence of this, their growth mode in thin films results often in polymorphic structures, frequently differing from these of the bulk phase.

Third, there are also important differences in the interaction of substrate and molecule: the large size of organic molecules and their associated unit cell make commensurate struc-

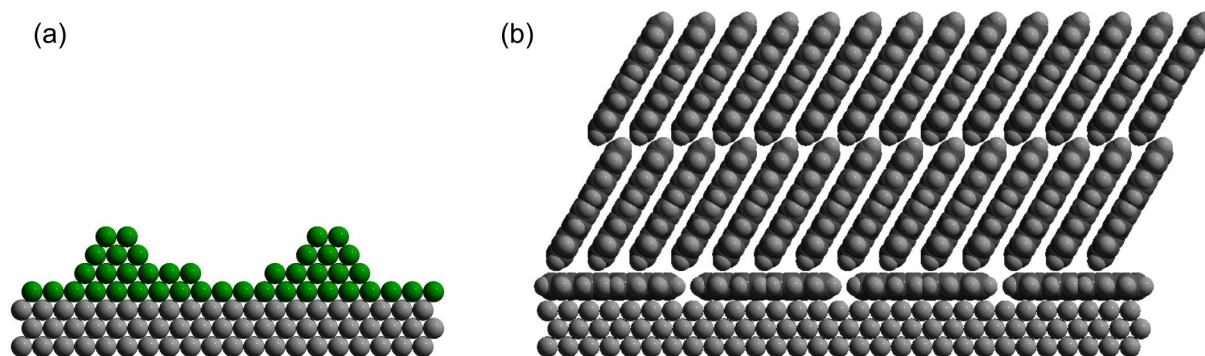


Figure 3.4: In contrast to atomic systems (a) which show spherical symmetry organic molecules (b) are extended and anisotropic objects giving rise to orientational degrees of freedom. Thus, new growth scenarios are possible such as a change of molecular orientation within adjacent molecular layers.

tures not always the favored one as it is usually observed for inorganic materials. This is a result of the effective lateral variation of the potential which is smeared out, i.e. averaged over the size of the molecule, implying an effective corrugation of the substrate which is experienced by the molecule in a weaker fashion. In addition, more translational domains can be found due to the size difference of the unit cells of adsorbate and substrate. Since organics show the tendency to crystallize in low-symmetry structures multiple domains are frequently observed.

All these considerations make organic growth a subject richer in phenomenology and therefore difficult to generalize in growth paradigms described by theoretical models. Nevertheless, some common guidelines can be given by looking at the corresponding adhesion energy in the interface between organic compound and substrate. Therefore, some general aspects of two relevant substrate classes will be discussed briefly: metals and metal oxides. Metal surfaces typically lead to an adhesion energy which is significantly stronger than the cohesion energy within the molecular bulk. In general, the organic molecules lie flat at the interface as also shown later in chapter 7 of this thesis. For thicker films, a molecular re-orientation toward a standing configuration commonly occurs to minimize the surface energy of the organic film. This results in a structure close or identical to the one found in the bulk phase. On metal oxides and passivated semiconductor surfaces, molecule-molecule interactions dictate the structure in the thin film and substrate-molecule interactions play a less important role. Hence, the weak molecule-substrate interactions favor

multilayer growth of more or less upright standing molecules where the long axis of the molecule is often found to be oriented almost normal to the substrate [38]. Silicon wafers are among one of the most important substrates due to their technological relevance and extreme flatness. However, several recent studies evidence that the growth mode is not so simple and that significant differences in the molecular tilt angle and lateral spacing may exist in the first layers on SiO₂, in spite of being amorphous on a chemically inert substrate [39,40].

3.2 Organic Semiconducting Molecules

In the following section, n- and p-type semiconducting molecules investigated in this thesis are presented. They belong to the group of aromatic molecules, a subclass of oligomers, which are characterized by a relatively simple shape consisting of several carbon rings to ensure the planarity of the molecular core. They can be modified by functional end-groups. Their simple shape allows a dense packing and facilitates crystallization of these molecules (see Figure 3.5). In addition, aromatic molecules have a high thermal stability making it possible to evaporate them in UHV what, in turn, guarantees a good control over their chemical and physical properties.

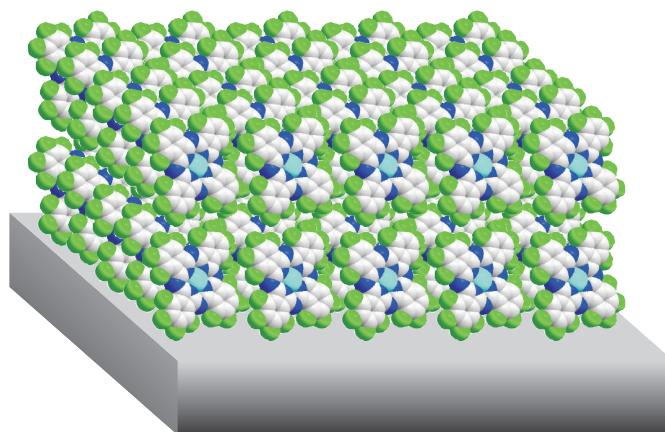


Figure 3.5: Schematic example of an aromatic molecule (F₁₆CuPc) forming a dense packing on a substrate.

3.2.1 PTCDI-C₈

N,N'-dioctyl-3,4:9,10-perylene tetracarboxylic diimide (in short PTCDI-C₈) belongs to the family of perylene bisimide which were initially applied for industrial purposes as red vat dyes. Later on, several perylene bisimide compounds were used in industrial applications as pigments due to weather and light-fastness, high thermal stability and insolubility. Nowadays, the major focus is in the field of electronic implementations since perylene bisimides are one of the best n-type semiconductors available [14, 41–45]. Recently, perylene bisimides derivatives were successfully synthesized showing reasonable charge carrier mobilities in ambient conditions [46–48].

Among the different perylene bisimide compounds we have chosen PTCDI-C₈ as an n-type semiconductor. Electron mobilities up to 1.7 cm²/Vs were measured for organic thin film transistors composed of PTCDI-C₈ molecules under UHV conditions [11]. The molecule (C₄₀H₄₂O₄N₂) consists of a planar core with two alkyl chains on opposite sides as shown in Figure 3.6 (a). As already mentioned in the motivation, there is a particular demand in n-type materials (the majority of them is p-type) in order to enable the fabrication of organic solar cells, ambipolar transistors and OLEDs in which both p- and n-type semiconductors are needed. Up to now, there are only few studies about structural properties of PTCDI-C₈ films. By employing x-ray diffraction in reflection mode

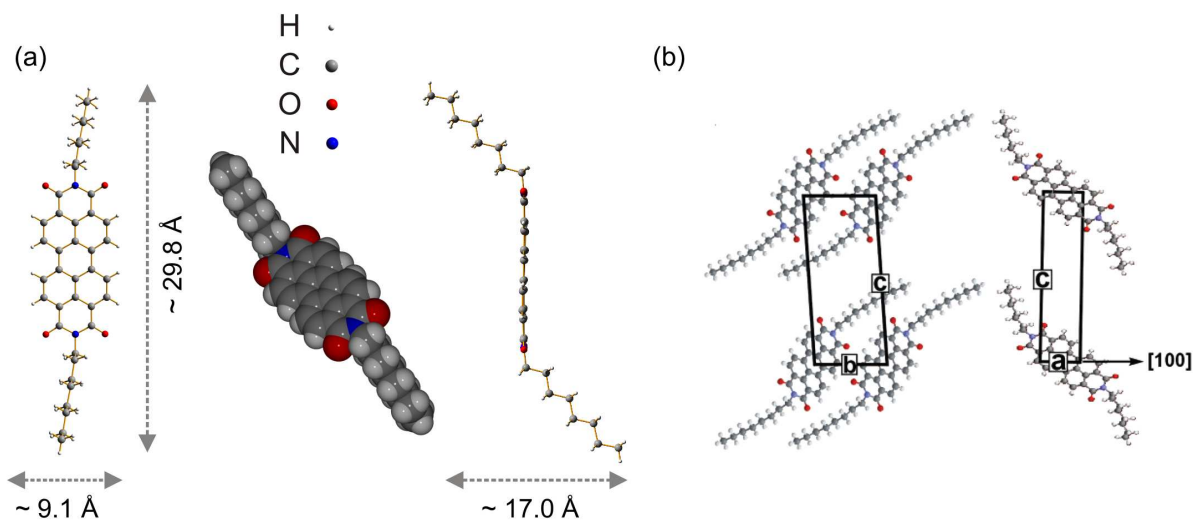


Figure 3.6: (a) Molecular structure and dimensions of PTCDI-C₈. (b) Molecular arrangement within the unit cell determined for the bulk structure of several millimeter long PTCDI-C₈ needles [20].

	a [Å]	b [Å]	c [Å]	α	β	γ	Z
PTCDI-C ₈	4.68	8.50	19.72	85.99°	91.57°	82.79°	1

Table 3.1: Cell parameters reported for the bulk structure of several millimeter long PTCDI-C₈ needles [20].

an out-of plane lattice constant of ~ 20 Å was reported for highly ordered PTCDI-C₈ films on SiO₂ [10]. Lately, the cell parameters for the bulk structure of several millimeter long PTCDI-C₈ needles were determined by x-ray crystallography summarized in Table 3.1 [20]. The corresponding molecular arrangement proposed within this unit cell is shown in Figure 3.6 (b).

3.2.2 Phthalocyanines

Phthalocyanines are porphyrin derivatives which, down to the present day, have attracted enormous interest due to their intense coloring properties associated with their use as blue and green pigments. Since the discovery of their semiconducting properties they are also employed as building blocks for the construction of new molecular materials for electronics and optoelectronics.

Phthalocyanines are planar molecules consisting of four isoindole subunits linked together through nitrogen atoms. In the following subsections, we focus on four representatives of the group of metal-phthalocyanines which are characterized by the presence of a metal atom in the molecular center.

Copper Phthalocyanine (CuPc)

Numerous applications of copper phthalocyanine (C₃₂H₁₆N₈Cu) as paint, dye for textiles and plastics and even for food coloring has been described in several hundred literature references and shows the significance of this compound illustrated in Figure 3.7 (a). The molecule is thermally stable and can therefore be sublimated. Semiconducting behavior was reported in bulk phthalocyanines in 1948 for the first time [49]. But only recently, these molecules have been considered as potential candidates for plastic electronics acting preferentially as p-type semiconductors [50–54].

Several studies have been performed trying to elucidate the bulk structure of copper phthalocyanine [55,56]. For the thin-film structure of CuPc, it turns out that two major

polymorphs exist where the stable modification is generally called the β -form and the metastable form of the crystal structure the α -form (see Figure 3.7 (b) and (c) and Table 3.2) [57–60]. However, the β -phase is only achieved at high temperatures ($\sim 240\text{ }^\circ\text{C}$) and beyond a critical thickness of about 800 nm [59]. Beside these two main modifications, there were lately γ - and ϵ -CuPc synthesized [61].

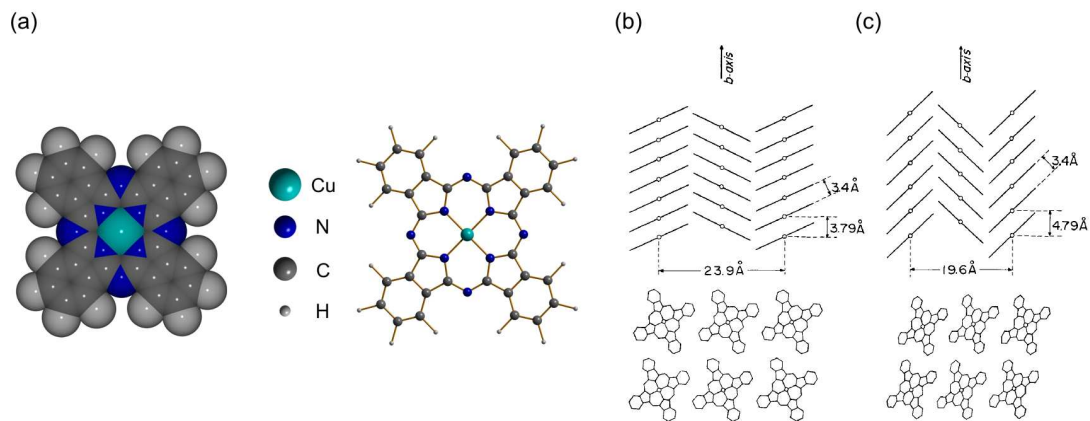


Figure 3.7: (a) Molecular structure of CuPc. Molecular arrangements in CuPc crystals of the (b) α -form and (c) β -form [57].

	α -CuPc	β -CuPc
a [Å]	25.92	19.407
b [Å]	3.79	4.79
c [Å]	23.92	14.628
α	90°	90°
β	90.4°	120.56°
γ	90°	90°
Z	4	2

Table 3.2: Cell parameters reported for the structure of α -CuPc [56] and β -CuPc [57].

Copper Hexadecafluorophthalocyanine ($F_{16}CuPc$)

Copper hexadecafluorophthalocyanine ($C_{32}F_{16}N_8Cu$) differs from $CuPc$ in the 16 hydrogen atoms surrounding the molecule which are replaced for this compound by fluorine atoms as can be seen in Figure 3.8 (a).

This substitution implies an increase in electron affinity which allows a more efficient electron injection into the empty LUMO states resulting in a change to primarily n-type behavior when combined with high work function metals such as gold. $F_{16}CuPc$ is one of the few air stable n-type semiconductors making this molecule an interesting candidate for applications in OTFTs, ambipolar transistors and organic photovoltaic cells [62–69].

The parameters of the $F_{16}CuPc$ bulk structure are given in Table 3.3 together with the unit cell parameters for the in-plane thin film structure on SiO_2 which undergoes

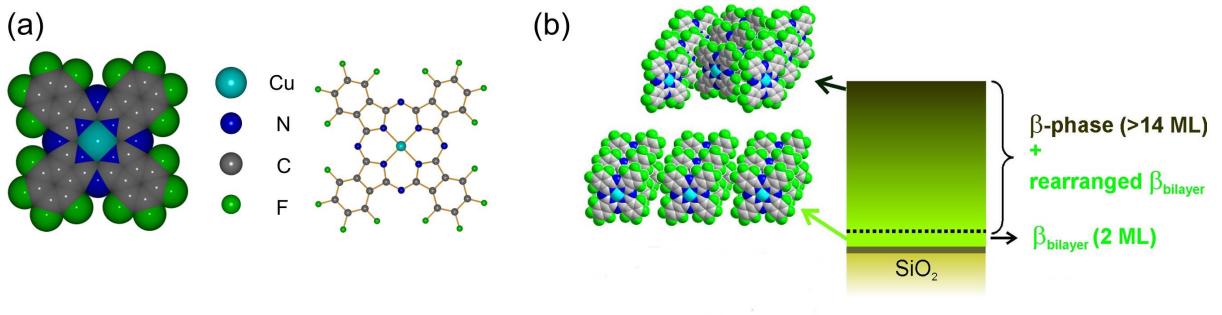


Figure 3.8: (a) Molecular structure of $F_{16}CuPc$. (b) Thin film structure on SiO_2 where a structural transition of the molecular arrangement takes place from $bilayer-F_{16}CuPc$ to $\beta-F_{16}CuPc$ [72].

	$bulk-F_{16}CuPc$	$bilayer-F_{16}CuPc$	$\beta-F_{16}CuPc$
a [\AA]	14.61	29.52	20.26
b [\AA]	3.31	3.79	4.87
c [\AA]	23.92	-	-
α	90°	-	-
β	90.4°	-	-
γ	90°	$\sim 90^\circ$	84.1°
Z	2	2	2

Table 3.3: Cell parameters reported for the bulk [71] and thin film structure on SiO_2 [72] of $F_{16}CuPc$.

a thickness-dependent structural transition between a coverage of two monolayers to 14 monolayers from *bilayer*-F₁₆CuPc to β -F₁₆CuPc as shown in Figure 3.8 (b) [71, 72].

Cobalt Phthalocyanine (CoPc)

Cobalt phthalocyanine (C₃₂H₁₆N₈Co) only differs from CuPc in the center atom which is replaced in this case by a cobalt atom (see Figure 3.9). An important aspect of this molecule is that, beside its semiconducting behavior as a p-type material [73], it also shows magnetic properties [74–76].

Unlike copper based phthalocyanine compounds there are no structural reports so far about thin films of CoPc. However, for the bulk structure it is known that several polymorphs exist among the α - and the β -configuration are best-known [70, 77–79]. Their structural properties are summarized in Table 3.4 [79]. α -CoPc is triclinic having one molecule within the unit cell whereas β -CoPc exhibits a monoclinic structure with $Z = 2$.

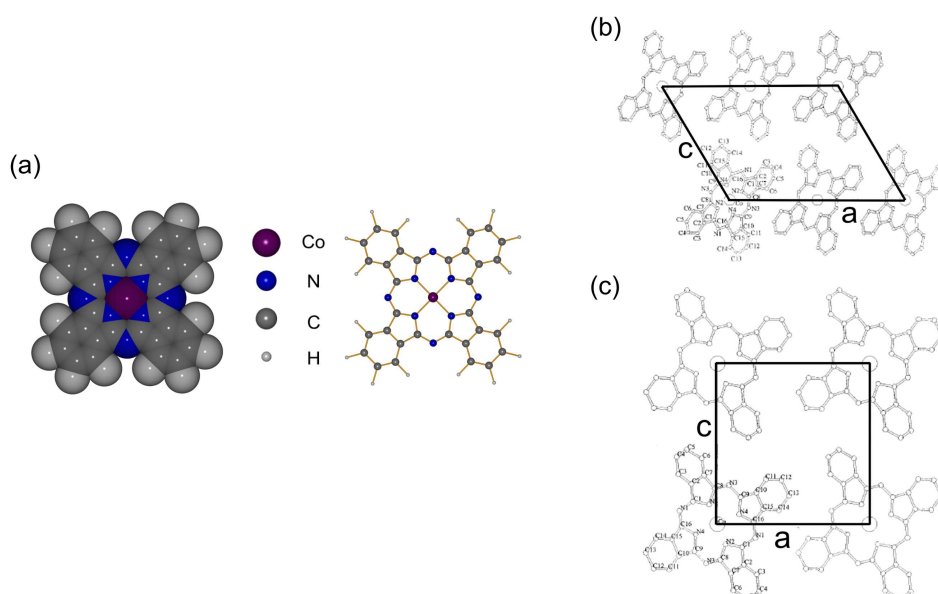


Figure 3.9: (a) Molecular structure of CoPc. Molecular arrangement of (b) α -CoPc and (c) β -CoPc as seen along the [010] direction [79].

	α -CoPc	β -CoPc
a [Å]	12.090	14.5982
b [Å]	3.754	4.7937
c [Å]	12.800	19.4348
α	88.96°	90°
β	90.97°	120.782°
γ	95.09°	90°
Z	1	2

Table 3.4: Cell parameters reported for the structure of α -CoPc and β -CoPc [79].

Cobalt Hexadecafluorophthalocyanine ($F_{16}CoPc$)

Cobalt hexadecafluorophthalocyanine is a rather poorly investigated semiconducting molecule. Its chemical formula is $C_{32}F_{16}N_8Co$ and its molecular structure can be seen in Figure 3.10. Up to now, the thin film structure on SiO_2 has been reported proposing a rectangular unit cell with the parameters denoted in Table 3.5 [80].

Similarly to $F_{16}CuPc$, $F_{16}CoPc$ starts to order during the first two layers in the bilayer configuration before, upon subsequent growth, polymorphism sets in and both structures grow simultaneously. The β structure is favored as the the coverage is increased.

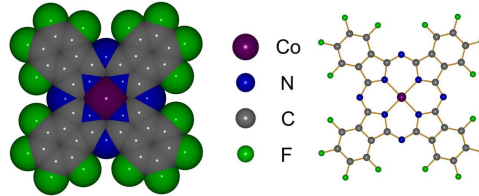


Figure 3.10: Molecular structure of $F_{16}CoPc$.

	<i>bilayer</i> - $F_{16}CoPc$	β - $F_{16}CoPc$
a [Å]	14.61	20.43
b [Å]	3.19	4.84
γ	$\sim 90^\circ$	83.4°
Z	1	2

Table 3.5: Cell parameters reported for the thin film structure of $F_{16}CoPc$ on SiO_2 [80].

3.2.3 Pentacene

Among organic semiconducting materials pentacene has been found to have one of the highest mobilities for hole transport [81,82]. Therefore, it is one of the most characterized materials and a large number of growth studies have been performed on SiO₂ due to its application as gate dielectric in thin film transistors [83–90].

Pentacene (C₂₂H₁₄) is a planar molecule composed of five benzene rings. It crystallizes in a layered structure with a herringbone arrangement within the layers as demonstrated in Figure 3.11 (a) - (c). Two polymorphs are reported for bulk-phase pentacene both showing a triclinic structure (see Table 3.6). Evaporated thin films, however, undergo a phase transition from the so called thin-film structure to the bulk structure beyond a critical thickness. Just recently, the complete crystal structure of thin films of pentacene has been determined by surface x-ray diffraction [40,90].

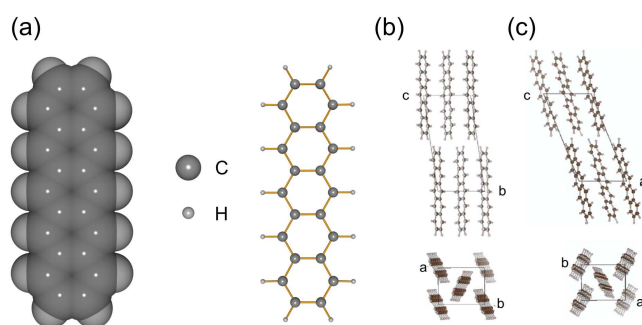


Figure 3.11: (a) Molecular structure of pentacene. Structure and molecular packing of the pentacene (b) thin film phase and (c) bulk phase [40].

	bulk-phase	bulk-phase	thin-film
a [Å]	6.485	7.90	5.958
b [Å]	7.407	6.06	7.596
c [Å]	14.745	16.01	15.61
α	77.25°	101.9°	81.25°
β	85.72°	112.6°	86.56°
γ	80.92°	85.08°	89.80°
Z	2	2	2

Table 3.6: Cell parameters reported for the bulk-phase [85,91] and thin-film [90] structure of pentacene on SiO₂.

4 Experimental Techniques

In surface science, it is crucial to attain a precise characterization of structural and morphological properties which in general is only made possible by employing complementary techniques. This chapter shall give the reader an overview of the different experimental techniques used in this thesis. X-ray scattering experiments were chosen to gain accurate information of the overall organic thin film structure. In addition to x-ray scattering experiments which spatially average over a larger sample area, atomic force microscopy and scanning tunneling microscopy were used to obtain locally resolved structural information at the surface of the respective organic materials. Electron microscopy investigations were applied where the other two techniques did not allow a detailed study of the surface. Here, scanning electron microscopy gave a more general idea of the growth mode and morphology whereas transmission electron microscopy provided information about specific structural properties of the organic architectures down to a few Ångströms.

4.1 X-ray Scattering

After the discovery of x-rays by WILHELM CONRAD RÖNTGEN in 1895 it still took some years before the true potential of this discovery was fully appreciated [92]. It was in 1912 when FRIEDRICH and KNIPPING demonstrated with the first x-ray diffraction experiment the electromagnetic nature of x-rays [93]. With this new technique they revealed at the same time the atomic structure of crystals by observing a pattern of regularly placed well defined spots as already proposed by MAX VON LAUE. The use of x-rays nowadays stretches across medicine, chemistry, physics and even art, just to list a few. Generally, it can be distinguished between the following techniques: imaging, spectroscopy and scattering, each giving a particular kind of information about the structural properties

and composition of the respective material under investigation. In this thesis, x-ray scattering has been employed to investigate the structure of thin films. The next section is therefore providing a short overview in theoretical and technical aspects of this method. A more profound description can be found in references [94–97].

4.1.1 X-ray Diffraction

X-rays are scattered by electrons with a scattering length which can be expressed, in the case of elastic scattering, by the so called Thomson scattering length or classical electron radius r_e . All scattering processes can be depicted by an incoming wave with momentum $k_i = 2\pi/\lambda$ and an outgoing wave with momentum $k_f = 2\pi/\lambda$ involving a momentum transfer $\mathbf{q} = \mathbf{k}_f - \mathbf{k}_i$ with λ being the wavelength. Assuming kinematic approximation (i.e. absorption is neglected as well as multiple scattering effects), the scattering length of an atom can be expressed by

$$r_e \cdot f_0(\mathbf{q}) = r_e \cdot \int \rho(\mathbf{r}) e^{i\mathbf{q}\cdot\mathbf{r}} d^3r \quad (4.1)$$

where $f_0(\mathbf{q})$ is the Fourier transform of the electron distribution described by a continuous electron density $\rho(\mathbf{r})$. $f_0(\mathbf{q})$ is also called the atomic form factor. $\mathbf{q} \cdot \mathbf{r} = (\mathbf{k}_f - \mathbf{k}_i) \cdot \mathbf{r}$ is the resulting phase shift taking place between waves scattered from different volume elements. In the case of atoms with bonded electrons (equation 4.1 is only valid for free electrons), two additional energy dependent terms called dispersion and absorption correction factors have to be included, resulting in

$$f(\mathbf{q}, E) = f_0(\mathbf{q}) + f'(E) + if''(E). \quad (4.2)$$

If the atom is isolated, that is in absence of chemical bonds, the atomic form factor can be approximated by the following analytical expression:

$$f_0(q) = \sum_{i=1}^4 a_i \cdot e^{b_i(\frac{q}{4\pi})^2} + c_0. \quad (4.3)$$

a_i , b_i and c_0 are fitted parameters for each type of atom and can be found in the International Tables of X-ray crystallography together with the dispersion and absorption correction factors [100]. In order to get the structure factor of a single molecule, the

atomic form factors have simply to be summed up leading to

$$F_{mol}(\mathbf{q}) = \sum_j f_j(\mathbf{q}) e^{i\mathbf{q}\cdot\mathbf{r}_j} d^3r \quad (4.4)$$

with f_j being the atomic form factors for each atom and \mathbf{r}_j being the respective atomic position. Now, the next step is to add all molecules k within the unit cell to obtain the structure factor

$$F_{unit\ cell}(\mathbf{q}) = \sum_k F_{k,mol}(\mathbf{q}) e^{i\mathbf{q}\cdot\mathbf{r}_k} d^3r . \quad (4.5)$$

Finally, it is possible to determine the structure factor of a crystal lattice by summing up over all n unit cells resulting in

$$F_{crystal}(\mathbf{q}) = \sum_n F_{n,unit\ cell}(\mathbf{q}) e^{i\mathbf{q}\cdot\mathbf{r}_n} d^3r . \quad (4.6)$$

Due to the fact that the crystal is extended over n unit cells and not the whole space, the sum in equation 4.6 can be transformed by using the form of a geometric series. Thus, the scattered intensity which is proportional to the modulus square of the structure factor of the crystal can be written as

$$I(\mathbf{q})_{crystal} \propto |F(\mathbf{q})_{crystal}|^2 \cdot \frac{\sin^2(N_x \mathbf{q} \cdot \mathbf{a}_x / 2)}{\sin^2(\mathbf{q} \cdot \mathbf{a}_x / 2)} \frac{\sin^2(N_y \mathbf{q} \cdot \mathbf{a}_y / 2)}{\sin^2(\mathbf{q} \cdot \mathbf{a}_y / 2)} \frac{\sin^2(N_z \mathbf{q} \cdot \mathbf{a}_z / 2)}{\sin^2(\mathbf{q} \cdot \mathbf{a}_z / 2)} \quad (4.7)$$

where N_x , N_y and N_z are the the number of unit cells and \mathbf{a}_x , \mathbf{a}_y , \mathbf{a}_z the lattice vectors in the three crystallographic directions. From this relationship it can be seen that the intensity pattern is sharply peaked exactly at the time when all the denominators of the interference functions equal zero also referred to as the Laue condition being fulfilled. Furthermore, the intensity is proportional to the square modulus of the structure factor which is able to strongly modulate the intensity pattern. This, in turn, will depend on the molecular arrangement within the unit cell and its associated electron density.

For simplicity, a one-dimensional crystal is now being considered which in fact can be used to describe the scattered intensity from a layered film when measured in specular geometry, i.e. two components of the momentum transfer \mathbf{q} are zero. From equation 4.6

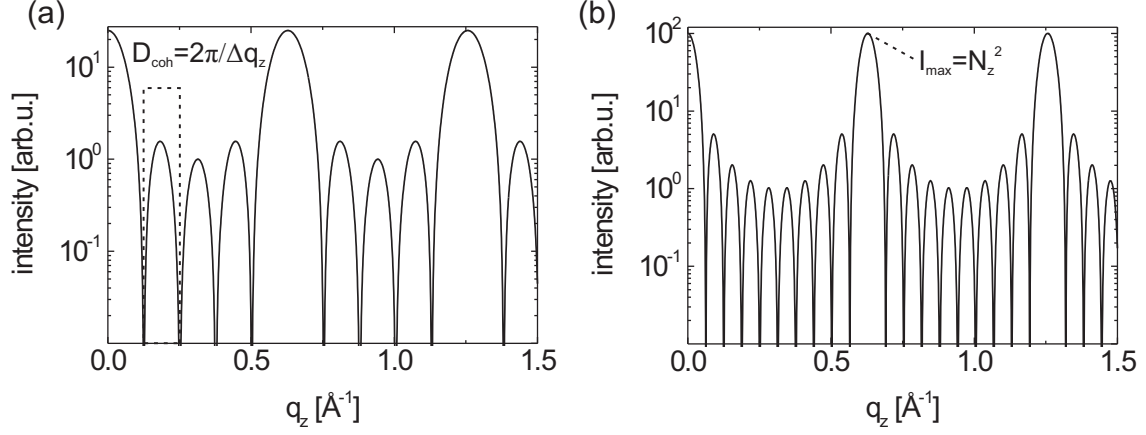


Figure 4.1: Scattered intensity for a one dimensional crystal or ordered film for (a) $N_z = 5$ and (b) $N_z = 10$ with $|F(\mathbf{q})_{\text{crystal}}|^2 = 1$.

it follows now that

$$I(q_z)_{\text{crystal}} \propto |F(q_z)_{\text{crystal}}|^2 \cdot \frac{\sin^2(N_z q_z a_z / 2)}{\sin^2(q_z a_z / 2)} \quad (4.8)$$

if, for instance, q_x and q_y are set to zero. The corresponding graph can be seen in Figure 4.1 for $|F(\mathbf{q})_{\text{crystal}}|^2 = 1$ and $N_z = 5$ and $N_z = 10$, respectively. The periodicity a_z is related to the position of the principal maxima where the momentum transfer coincides with the reciprocal lattice vector $a_z^* = 2\pi/a_z$. The peak intensity of these maxima are proportional to $N_x^2 N_y^2 N_z^2$. The distance between minima of adjacent side-peaks Δq_z determines the crystal size or in the case of a film its coherent thickness $D_{\text{coh}} = 2\pi/\Delta q_z$. All these considerations made for one dimension can be applied to three dimensions.

4.1.2 X-ray Reflectivity

The interaction of electromagnetic waves with matter can be characterized by means of the index of refraction. For x-rays

$$n = 1 - \delta_d + i\beta_a \quad (4.9)$$

with $\delta_d = \lambda^2 r_e \rho / 2\pi$ being the dispersion and $\beta_a = \lambda \mu_a / 4\pi$ being the absorption. r_e is the aforementioned Thomson scattering length, ρ the electron density and μ_a the absorption coefficient of the respective material. Note that equation 4.9 is only valid for x-ray energies far from absorption edges as being the case in this thesis.

X-rays exhibit total external reflection for incidence angles θ_i below the critical angle $\theta_{crit} = \sqrt{2\delta_d}$ as a consequence of $n < 1$. Almost all incoming radiation is reflected (there are small losses due to absorption) since the x-rays do not penetrate far into the medium. With increasing incident angle, however, the reflectivity R and therefore also the intensity drops rapidly according to

$$R \approx \left(\frac{\theta_{crit}}{2\theta_i} \right)^4 \quad \text{for } \theta_i > 3\theta_{crit} \quad (4.10)$$

deduced from the Fresnel equations. This simple case for a perfectly smooth vacuum/medium interface is illustrated in Figure 4.2 (a). Notice the logarithmic scale which is usually used in order to take the drastic decrease in intensity into account.

Considering a system of two perfect layers with two interfaces leads to the intensity pattern shown in Figure 4.2 (b). Here, one layer represents the substrate whereas the second layer correspond to the case of a homogeneous film. It can be seen that a periodic oscillation appears (the so called Kiessig fringes) due to the interference of x-rays scattered at the vacuum/film and film/substrate interface. The width Δq_z of each oscillation is related to the film thickness D via $D = 2\pi/\Delta q_z$ with $q_z = 4\pi \sin \theta / \lambda$ being the momentum transfer perpendicular to the surface for equal incident and exit angles θ_i and θ_f . If the film has an internal periodic modulation of the electron density, for example a layered film, additional peaks are visible in the intensity pattern as demonstrated in Figure 4.2 (c). These so called Bragg peaks arise if the Bragg condition $2d \sin \theta = N\lambda$ is fulfilled (N is an integer) where d is the film periodicity along the surface normal corresponding to the periodicity a_z introduced in the previous section. Figure 4.2 (d) shows the damping of the reflected intensity pattern when interfacial and surface roughness is taken into account.

It can be seen that the reflected intensity contains information about the projection of the electron density along the surface normal which is directly related to the projected crystalline structure in this direction. Furthermore, the roughness between layers and at the surface can be extracted from x-ray reflectivity.

Structural information of complex layered systems as shown in Figure 4.2 (c) and (d)

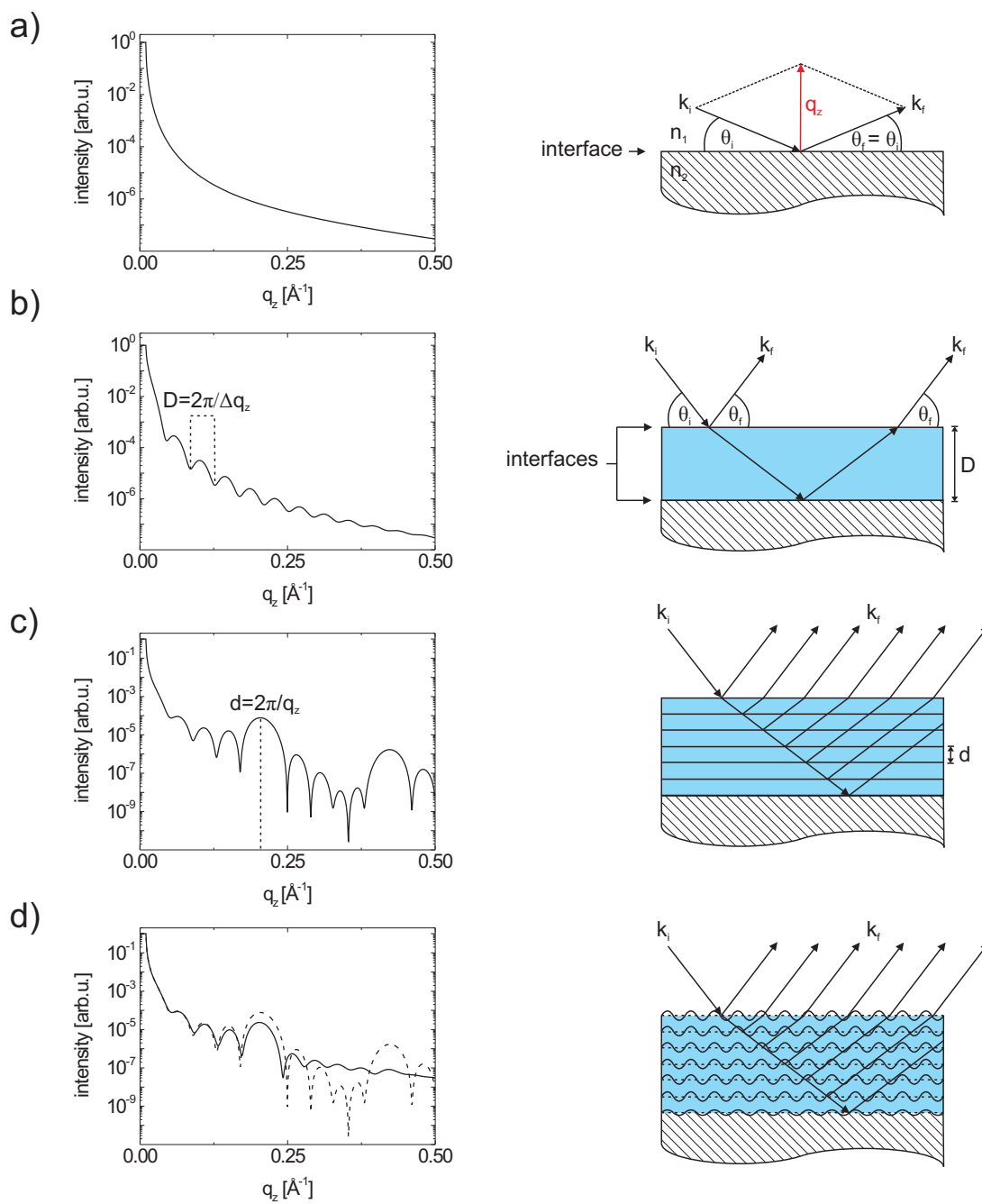


Figure 4.2: Computed reflectivity curves (left side) as a function of momentum transfer q_z (a) from a perfectly smooth vacuum/medium interface, (b) from a single homogeneous layer or film with two interfaces, (c) if the film has an internal periodic modulation of the electron density and (d) if roughness is taken into account (the dashed curve is taken from (c) for a better comparison).

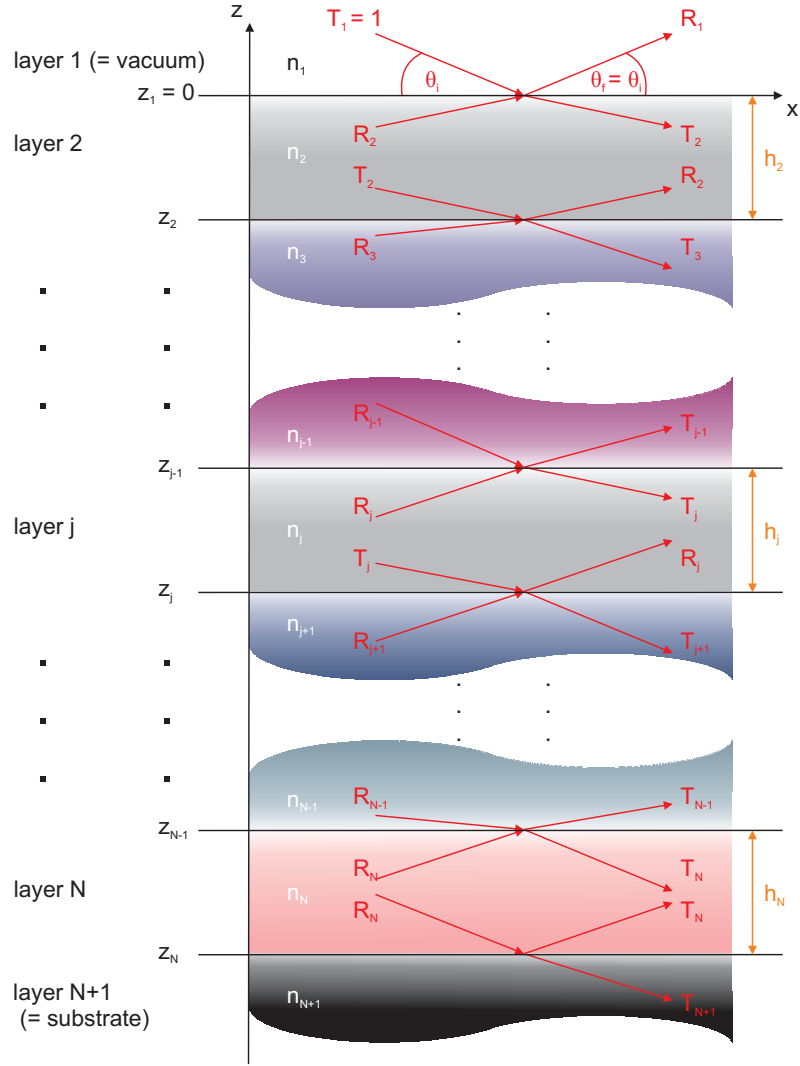


Figure 4.3: Schematic illustration of the reflection and refraction of plane waves at $N + 1$ slabs separated by N interfaces. Each layer is characterized by a refractive index n_j and a thickness h_j .

can be obtained from a fit of the reflected x-ray intensity. For this analysis, an adequate structure model of the electron density has to be proposed for which the x-ray intensity has to be calculated and compared to the experimental one. One of the methods employed in this thesis is called the Parratt formalism where such a complex layered structure is divided into a series of slabs with well defined interfaces [95, 101]. Figure 4.3 shows N interfaces with $N + 1$ slabs including the top layer (normally vacuum, $j = 1$) and substrate ($j = N + 1$) each characterized by a refractive index n_j and a thickness h_j . The

reflectivity R^2 is calculated via a recursive algorithm from the squared modulus of the ratio between the reflected wave-amplitude R_j and the transmitted wave-amplitude T_j in the j -th slab. In order to take roughness into account an exponential damping term is introduced which smears out the calculated electron density profile between adjacent slabs. Altogether, each slab exhibits four fitting parameters: the electron density, the absorption coefficient, the thickness and the roughness. X-ray reflectivity is a powerful tool to investigate the internal structure of thin films and buried interfaces in a precise way.

4.1.3 Grazing Incidence X-ray Diffraction

At incident angles θ_i below the critical angle θ_{crit} the totally reflected wave is accompanied by an evanescent wave field which travels parallel to the surface. The amplitude of the evanescent wave is exponentially damped according to

$$A_{eva} \propto e^{i\mathbf{k}_{\parallel} \cdot \mathbf{r}_{\parallel}} \cdot e^{-z/\Lambda} \quad (4.11)$$

and propagates perpendicularly in the range of a few nanometers. \mathbf{k}_{\parallel} denotes the wave vector parallel to the surface and \mathbf{r}_{\parallel} the plane parallel to the surface. z is the direction normal to the surface and Λ the penetration depth into the medium at which the amplitude of the wave has decreased to $1/e$ [96,99]. The high surface sensitivity of evanescent waves makes it possible to reveal lateral structural properties since the momentum transfer is mainly determined by the component q_{\parallel} in the plane as can be seen from the scattering

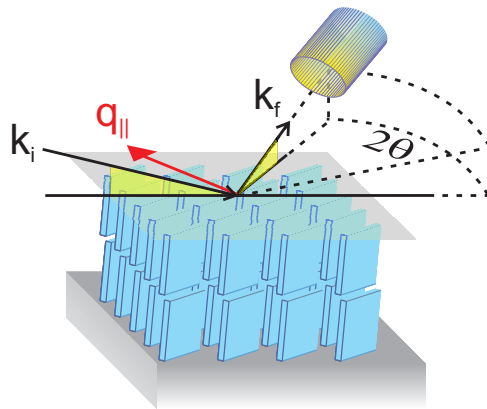


Figure 4.4: Schematic representation of the scattering geometry in GIXD.

geometry in Figure 4.4. By varying the incidence and scattering angles θ_i and θ_f depth-dependent structural studies are possible by employing grazing incidence x-ray diffraction (GIXD) [96]. Note, that the organic films examined in this thesis exhibit randomly oriented crystalline domains which implies that the in-plane structure is a 2D powder. Therefore, all GIXD scans were performed by rotating the detector around the fixed sample as shown in Figure 4.4.

4.1.4 Synchrotron Radiation

The history of synchrotron radiation is rather young beginning in the 1960s and 1970s. At that time, the first generation of synchrotron-radiation facilities were also called parasitic facilities because the accelerators were built primarily for high-energy and nuclear physics. Nowadays, third-generation synchrotron radiation sources are operating producing bright x-rays. Plans for the fourth-generation sources including ultrabright, coherent, pulsed time-structured x-rays are already in preparation.

When charged particles, especially electrons, are forced to move in a circular orbit, they emit photons. At relativistic velocities these photons are emitted in a narrow cone in the forward direction with energies ranging from the infrared to the x-ray spectrum. This radiation is called synchrotron radiation.

In order to produce synchrotron radiation artificially ultrahigh vacuum rings are used, the so called storage rings. They are either equipped with bending magnets where the electron is forced to change direction and, as a result, will be accelerated thereby emitting magnetic bremsstrahlung or synchrotron radiation. Or they have insertion devices (wigglers or undulators) sitting in the straight sections of the storage ring. Wigglers and undulators both consist of successive dipole magnets forcing the electron to follow an oscillating trajectory. The difference can be found in the kind of synchrotron radiation they emit. In a wiggler, electrons experience a higher deflection leading to a higher photon energy but also to a broadband synchrotron radiation. In undulators, however, the photon energy is in general smaller but showing a sharper spectrum and a higher brilliance.

The major advantage of synchrotron radiation over conventional x-ray tubes is the high brightness and intensity which is several orders of magnitude more. Furthermore, it exhibits a high collimation (meaning that the angular divergence of the beam is small) and

it can be tuned in energy and wavelength. Especially for experiments in grazing incidence condition, this highly brilliant radiation is crucial in order to detect a scattered signal from the respective sample. For organic thin films, synchrotron radiation is essential for surface studies due to their lower electron density when compared to inorganic materials. In the experiments presented in this thesis, radiation damage of the organic compounds was avoided by performing all synchrotron experiments under UHV conditions.

4.2 Scanning Probe Microscopy

Scanning probe microscopy (SPM) is based on the simple principle that a sharp tip is brought in direct contact with a surface causing interactions between tip and surface. A certain physical variable such as tunnel current or force is probed while the tip is scanning a defined area on the sample. In general, a constant interaction between tip and sample surface is set thereby recording the reaction of the tip due to topographic changes. The most common scanning probe microscopes are the scanning tunneling microscope (STM) and the atomic force microscope (AFM) whose general work principles will be explained in the following sections. In the case of the STM, the interaction relies on quantum tunneling effect whereas for AFM, the interaction is based on intermolecular forces as, for instance, van-der Waals, electrostatic, friction or capillary forces.

4.2.1 Scanning Tunneling Microscopy

Scanning tunneling microscopy (STM) had and still has a major impact in the scientific world due to the ability to image materials down to the atomic level. BINNIG and ROHRER who built the first instrument capable to resolve atoms got rewarded in 1986 by the Nobel Prize in physics [2–4,102,103]. The setup, as shown in Figure 4.5, and principle of STM is conceptually simple and is related to the quantum tunneling effect which allows an electron to cross an energy barrier. In general, the tunneling current I_T through a potential barrier V_b is according to

$$I_T \propto e^{-2\kappa d_b} \quad (4.12)$$

dependent on the decay constant $\kappa = \frac{2m}{\hbar} \sqrt{V_b - E}$ of the wave function and the barrier width d_b . E is the energy and m the mass of the electron and the difference $V_b - E$

is the average local work function of the tip and surface. In the case of the STM, d_B is the distance between the tip (normally a sharpened metallic wire) and the conducting surface of the sample. Since the tunneling current depends exponentially on the tip-sample distance, it mainly flows through the few atoms at the STM tip apex. Thus, the tunneling current is highly localized leading to a lateral resolution in the atomic range. Moreover, for typical work functions in the range of 4 to 5 eV, the exponential dependence of the tunnel current implies a change of one order of magnitude when the tip-sample distance is increased or reduced by 1 Å. The lateral tip position as well as the tip-sample distance are controlled by means of voltage signals applied to piezo-electric materials. Figure 4.6 (a) shows schematically the case of the isolated tip and sample surface with corresponding Fermi energies $E_{F,tip}$ and $E_{F,sam}$. When they are brought in electrical contact the Fermi levels adjust and it can be seen from Figure 4.6 (b) that the same amount of electrons escape from the tip to the sample as from the sample to the tip, i.e. the net current is zero. In order to provide a measurable current a voltage has to be applied. In the case of a positively biased sample as shown in Figure 4.6 (c) the net current originates from

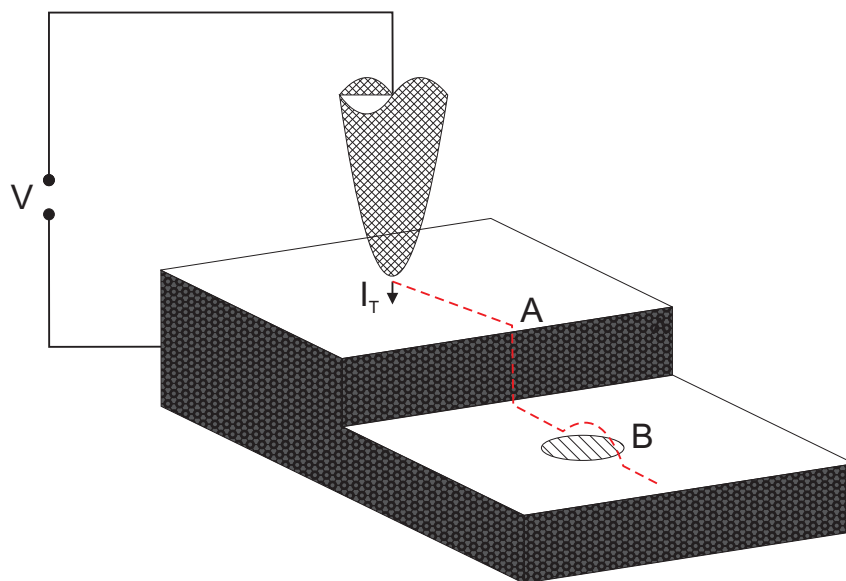


Figure 4.5: Schematic illustration of the STM. A sharpened metallic wire, the tip, is brought in close contact with the sample surface and a voltage V is applied between tip and sample. The tunneling current I_T and the height displacement of the tip is recorded while scanning across the sample surface. Point A represents a step which increases the distance between tip and sample. Point B depicts a chemical inhomogeneity changing the electrical properties of the surface. The tip is reacting at both points, A and B, as denoted by the dashed line.

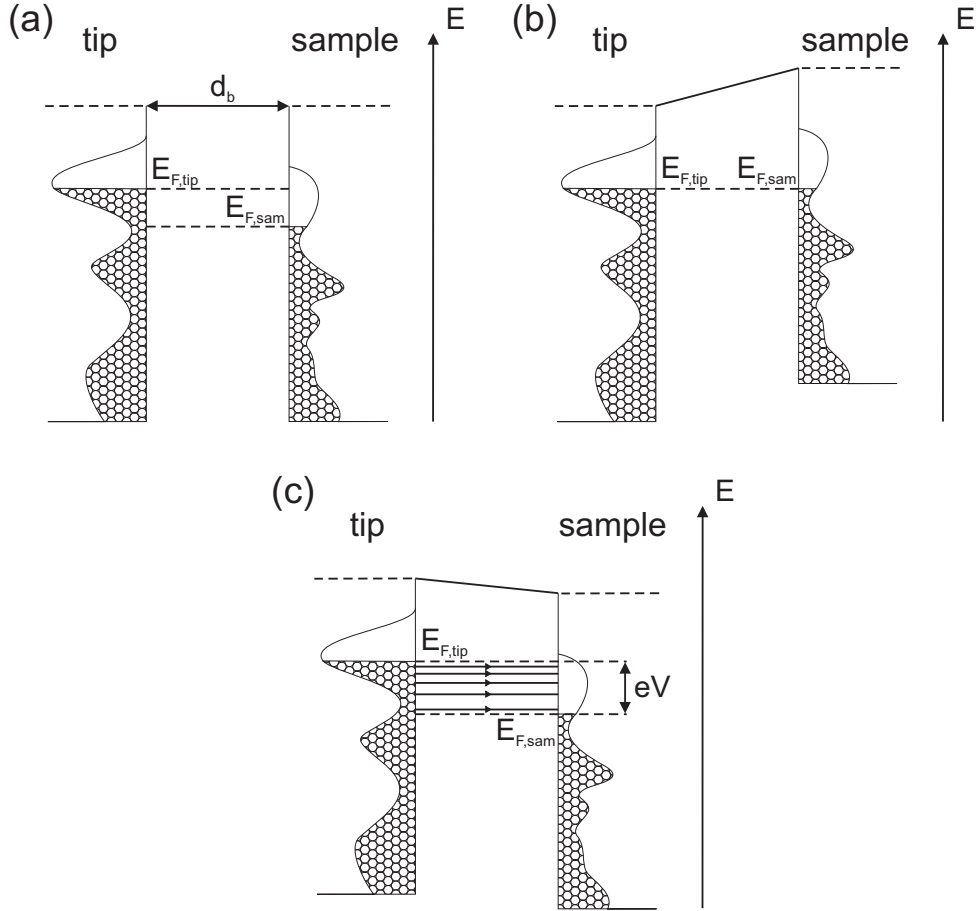


Figure 4.6: Schematic illustration of the Fermi energies $E_{F,tip}$ and $E_{F,sam}$ of tip and sample for (a) the isolated case, (b) when they are brought in contact and (c) when a positive bias is applied to the tip.

electrons tunneling from occupied states in the tip to unoccupied states of the sample. The current per energy unit is depicted by the density of horizontal arrows indicating a decrease with decreasing energy since the energetically lower states decay faster in the vacuum barrier region.

Although it is intuitively clear from Figure 4.6 (c) that the tunneling current will depend on the density of occupied and unoccupied states of tip and sample, the exact calculation of the tunneling current, taking into account the electronic structures of tip and sample, is not straightforward and a rather difficult task. One approach was suggested by TERSOFF and HAMANN who developed a theory allowing to compare quantitatively between the tunneling currents and the real measurements [104,105]. It is based on the widely used

transfer Hamiltonian approximation introduced by BARDEEN [106] where the tunneling current is given by

$$I_T = \frac{2\pi e}{\hbar} \sum_{\mu,\nu} f_F(E_\mu)[1 - f_F(E_\nu + eV)]|M_{\mu\nu}|^2\delta(E_\mu - E_\nu) \quad (4.13)$$

with $f_F(E)$ being the Fermi function, V the applied voltage and $M_{\mu\nu}$ the transfer matrix between states φ_μ of the probe and φ_ν of the surface. E_μ and E_ν are the respective energies of the states φ_μ and φ_ν in the absence of tunneling. $M_{\mu\nu}$ is expressed by

$$M_{\mu\nu} = -\frac{\hbar^2}{2m} \int_{\Sigma} d\mathbf{S} (\psi_\nu^* \nabla \psi_\mu - \psi_\mu \nabla \psi_\nu^*) \quad (4.14)$$

which must be evaluated over a surface Σ within the gap region and with the wave functions ψ_μ and ψ_ν of the unperturbed sample and tip, respectively. For measurements performed in the limit of low temperatures and low bias voltages equation 4.13 can be expressed by

$$I_T = \frac{2\pi e^2}{\hbar} V \sum_{\mu,\nu} |M_{\mu\nu}|^2 \delta(E_\nu - E_F) \delta(E_\mu - E_F). \quad (4.15)$$

It can be seen that I_T is related to the values of the tunneling matrix elements and the convolution of the electronic structure of tip and sample. The important aspect of this result is that recorded STM images are given by the convolution of the density of states belonging to both, tip and specimen. Thus, chemical changes on the sample surface can cause contrast differences in the image although there exists no height difference as can be schematically seen in Figure 4.5 at point B.

In STM, it can be distinguished between two main modes: constant-height or constant-current mode [107]. In constant-height imaging, the tip scans across the surface at a fixed height and bias V and the tunneling current I_T varies depending on topography and the local electronic properties of the specimen. The change in tunneling current measured at each location on the sample surface constitute the data set, the topographic image. In constant-current mode however, I_T is fixed while scanning the surface. A feedback guarantees the regulation of the distance tip-sample d_b in order to maintain the tunneling current constant. As mentioned above, it is crucial to bear in mind the interplay between topography and electronic structure for a correct interpretation of the STM data.

Each mode has advantages and disadvantages. Constant-height mode can be performed much faster since there is no need of any feedback regulation which is important for real time measurements. However, it only provides useful information for relatively smooth surfaces. Constant-current mode is still able to scan rougher surfaces with a high precision but imaging takes more time.

4.2.2 Atomic Force Microscopy

The crucial handicap of STM is the limit of measuring only electrically conductive samples. Therefore, in 1986 atomic force microscopy (AFM) was implemented allowing to image any arbitrary surface [108]. Its setup is also rather simple consisting of a pyramidal shaped tip attached to a probe called cantilever with elastic constant K (see Figure 4.7) which scans the substrate surface at small distances [109]. A piezoelectric scanner is either moving the tip across the sample or the sample across a fixed tip. Deflections of the cantilever, arising from interaction forces between sample and tip, are usually measured by focusing a laser beam on the cantilever. The reflected beam from the top side of the cantilever is collected by a position-sensitive photodiode. In absence of interaction forces the reflection is centered in the photodiode. However, as soon as the tip “feels” a force there will be a deflection of the cantilever. As a result, the reflected laser beam is changing its position on the photodiode generating now a different photo current. If the photodiode contains four independent segments it is possible to distinguish between deflection and torsion of the cantilever. In response to the normal force F_z the cantilever is bending down in z direction according to Hook’s law $F_z = K\Delta z$ inducing a vertical

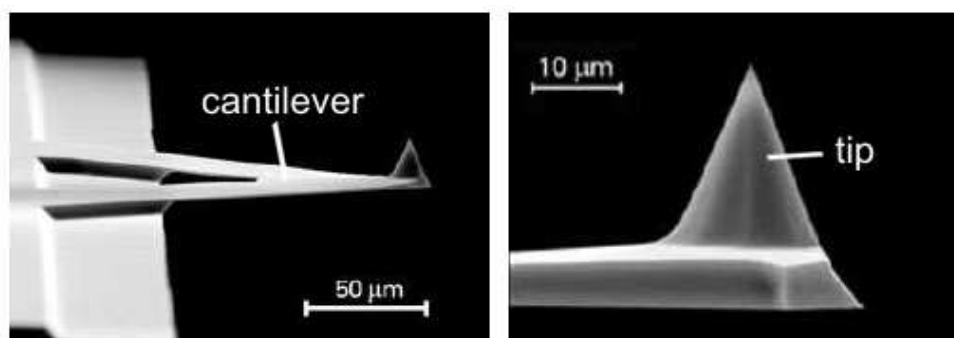


Figure 4.7: Scanning electron microscope image of a triangular cantilever with its attached tip.

displacement Δz . Torsions, however, lead to a lateral movement of the reflected laser beam on the photodiode.

The tip-sample force as a function of distance does not follow a monotonic behavior which makes it difficult to operate the AFM with a stable feedback loop. Thus, different modes are present to overcome this difficulty which basically can be divided into the contact mode and dynamic modes.

Contact Mode

In the contact mode, the tip is brought in direct contact with the sample's surface. While the tip is scanning across the surface, it is deflected as the tip is moving over the surface corrugation. There is a whole zoo of forces contributing to the deflection: short-range repulsive forces arising from the overlap of the tip and sample orbitals, long range van-der Waals forces as a result of dipole-dipole interactions, electrostatic forces, friction forces and adhesion forces. The measurement of the topography can be either carried out in constant height mode or constant force mode, both illustrated in Figure 4.8. The advantage of constant height mode is its simplicity since there is no demand on a feedback circuit. However, this mode is only applicable to very flat and smooth surface due to the tip's geometry. The constant force mode is more common. Here, the tip is kept at a constant cantilever deflection at each point by using a feedback circuit. If the cantilever deflection is changing, the feedback circuit immediately makes sure to get back to the initial cantilever position by moving the sample with the help of the piezoelectric scanner. Therefore, the topography of the sample corresponds to the recorded changes in the

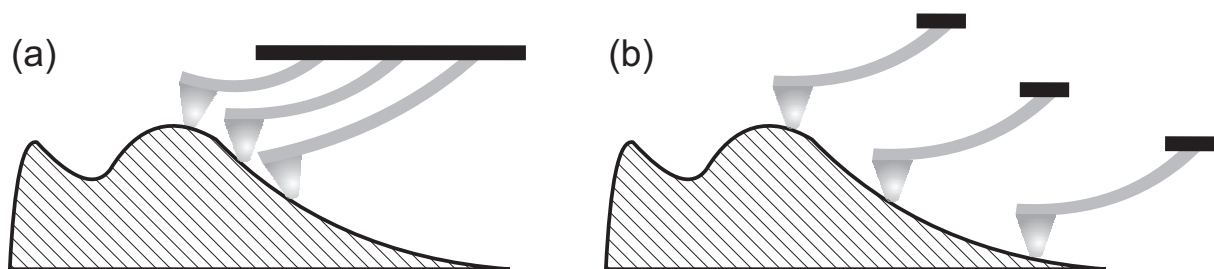


Figure 4.8: (a) Illustration of the constant height mode where the tip scans the surface at a constant height. (b) Constant force mode where the cantilever is kept at a constant cantilever deflection.

cantilever-surface displacements.

To display the force as a function of cantilever-surface distance is a general procedure to calibrate the cantilever sensitivity and to investigate the tip-sample interaction. Here, the cantilever deflection is measured while approaching and withdrawing the tip from the sample.

A special technique of contact mode is the jumping mode which is suitable to image softer samples and samples in liquids [110]. The working principle can be described as a cycle repeated at each image point with the following steps: first, the tip approaches into contact using a feedback which is in general performed on the cantilever deflection. Afterwards, it retracts out of contact and moves laterally one step. The relevant feature of jumping mode is that the lateral motion occurs when the tip is not in contact with the sample in order to avoid shear forces. However, the displacements in ambient conditions can be larger than 200 nm due to high adhesion forces. Therefore, the tip-sample separation and the approach step take a relatively long time which makes jumping mode a rather slow scanning mode.

It should be kept in mind that images measured with an AFM are always a convolution of the probe geometry and the shape of the features being imaged. Deconvolution of the tip should be taken into account for the analysis of samples with topographical characteristics in the nanometer scale.

Dynamic Mode

The idea of developing an AFM working in the so called dynamic mode was to minimize the sample damage which is inherent in contact mode since it is operating in the repulsive regime. The dynamic mode, in contrast, is taking place in the attractive regime. Here, the cantilever is mounted on an actuator to allow a deliberate oscillation by an external excitation amplitude A and excitation frequency ω . It can be distinguished between two basic methods of dynamic operation: amplitude-modulation and frequency-modulation [111,112]. Both modes have in common that the actuator is driven by a fixed amplitude at a fixed frequency being close to the resonance frequency $\omega_0 = \sqrt{k/m}$ of the free cantilever. This can be simply described by a driven harmonic oscillator with damping

via the differential equation

$$m\ddot{z} + \frac{m\omega_0}{Q}\dot{z} + m\omega_0^2 z = m\omega_0^2 A \cos(\omega t) \quad (4.16)$$

where Q is the quality factor related to the damping of the cantilever. The solution of this second order differential equation consists of the superposition of a transient term describing the adaption of the cantilever movement to the excitation frequency and a steady-state term with constant amplitude A_0 , frequency ω and phase ϕ :

$$z(t) = A_t e^{-\omega_0 t/2Q} \cdot \sin(\omega_0 t + \phi_t) + A_0 \cos(\omega t + \phi). \quad (4.17)$$

ϕ_t is the phase and A_t represents the amplitude of the transient term. The exponent $\omega_0 t/2Q$ determines the time τ after which the steady term dominates the motion. When the tip approaches the sample, interaction forces change both the amplitude and the phase relative to the driving signal of the cantilever. The important difference between amplitude-modulation and frequency-modulation is the feedback signal. In amplitude-modulation the change in amplitude is used as feedback. This change, however, does not happen instantaneously with a change in the tip-sample interaction but on a time scale of $\tau_{AM} \approx 2Q/\omega_0$ which makes this mode very slow (Q values are typically in the range of 10000 to 100000 in ultra high vacuum). The problem was solved by introducing the frequency-modulation where the change in the resonance frequency occurs within a single oscillation on a time scale of $\tau_{FM} \approx 1/\omega_0$.

Initially, both modes were meant to be non-contact modes implying that the cantilever is far away from the surface and clearly in the attractive regime. But the amplitude-modulation mode was also later used at an intermediate regime involving repulsive tip-sample interactions which is nowadays usually called tapping mode [113–115].

4.3 Electron Microscopy

The aim of any microscopy is to resolve structures which are not able to be seen by the naked eye. In the previous section, it was shown that this is manageable by the manufacture of sharp tips brought in close contact to the sample surface thereby exploiting the presence of different interactions between the tip and the sample. Another approach

was accomplished by the introduction of electron microscopy which uses the wave nature of electrons discovered by LOUIS DE BROGLIE in 1924 [116]. The term of an electron microscope was first used by KNOLL and RUSKA in 1932 and they succeeded in recording electron images [117, 118]. For this achievement, RUSKA received the Nobel prize (somewhat late) in 1986.

It is known that the limit of the resolution is given by the wavelength of the light. Therefore, electron microscopes (whose electron beams possess a wavelength of about 10^5 times smaller than that of light waves) exhibit the essential advantage over light microscopes that they can resolve structures in the atomic regime down to one to two Ångströms. In the next section, two representatives of electron microscopes will be shortly introduced, namely the transmission electron microscope (TEM) and the scanning electron microscope (SEM) which both work under vacuum. References [119–122] are suggested for a more profound understanding of both techniques.

4.3.1 Transmission Electron Microscopy

Transmission electron microscopy (TEM) can be divided into imaging and analytical TEM. Conventional TEM and high resolution TEM (HRTEM) allow an investigation of the micro- and nanostructure of the respective sample with a high spatial resolution down to the atomic level. Analytical TEM, in addition, gives an insight into the chemical composition as well as the electronic structure of the illuminated specimen. One prerequisite for TEM-studies is the thickness of the sample which should not exceed 200 nm in order to assure that the high energy electrons pass through. Rotationally symmetric, inhomogeneous magnet fields guarantee a collimating and focusing of the electron beam.

Figure 4.9 shows schematically the optical path in a conventional TEM. The beam is generated in the electron source (usually a heated tungsten filament, lanthanum hexaboride (LaB_6) cathode or a field emission cathode) and accelerated by an electric potential in the range of typically several 100 kV. A Wehnelt-cylinder and a condenser lens system focus the electron beam on the specimen where the interaction processes take place. The scattered electrons emerging from the thin sample are taken by the objective lens recombining them again to form an image in the image plane. In addition, a diffraction pattern is created in the back focal plane where an objective aperture can be inserted. Depending on the adjustment of the intermediate lens the viewing screen is showing ei-

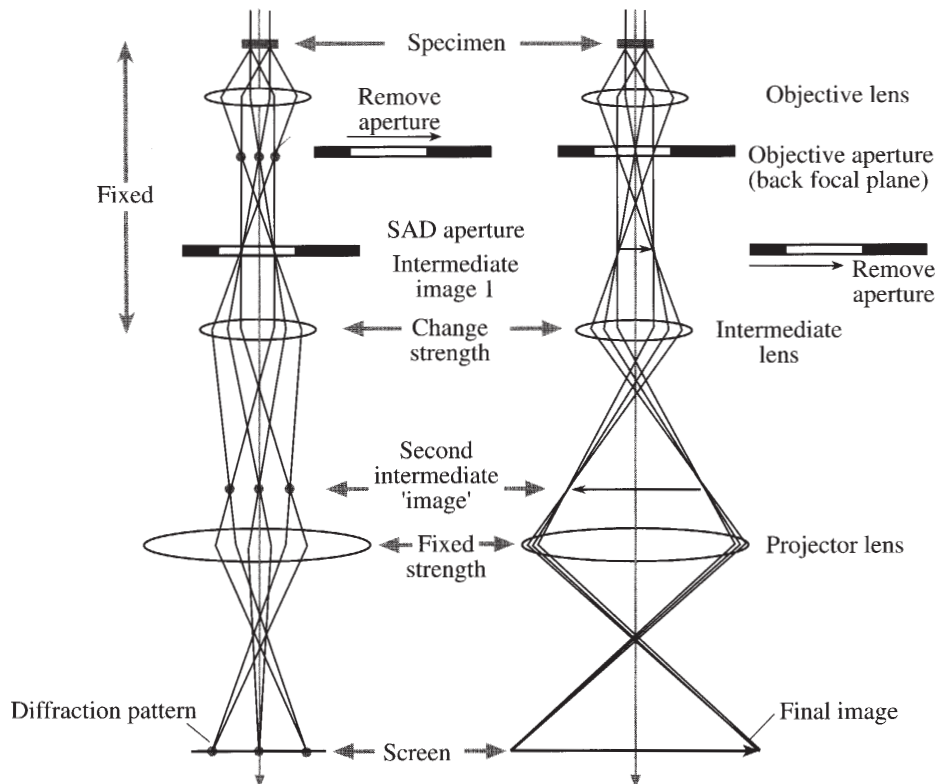


Figure 4.9: Schematic illustration of the optical path in the two basic operation modes of TEM. (a) Projection of the diffraction pattern on the viewing screen. (b) Projection of the image onto the screen (from Reference [120]).

ther the diffraction pattern or the image. If the back focal plane of the objective lens acts as the object plane for the intermediate lens, the diffraction pattern can be observed on the screen as illustrated in Figure 4.9 (a). If, however, the image plane of the objective lens acts as the object plane, then the image is projected onto the viewing screen as can be seen in Figure 4.9 (b). The contrast differences in conventional TEMs is related to the specimen structure and occurs in amorphous samples via scattering and in crystalline samples by diffraction.

One problem, which still has to be solved, is that the obtained diffraction pattern from the specimen contains electrons from its whole area. In this case, the viewing screen can be damaged due to the intense direct beam. Besides, the pattern is not very useful because the sample is very often buckled. The standard way to overcome this issue is to use a selecting aperture called selected-area diffraction (SAD) mode [123]. It is inserted

as shown in Figure 4.9 into the image plane of the objective lens and centered on the optic axis.

When using the diffraction pattern mode together with the SAD aperture two imaging operations can be performed by inserting the objective aperture: the bright-field (BF) image or the dark-field (DF) image. The BF image is characterized by selecting the direct beam with the objective aperture. In the DF image mode, the scattered electrons are chosen by adjusting the objective aperture.

4.3.2 Scanning Electron Microscopy

Scanning electron microscopy (SEM) has a lower resolution than TEM but allows to scan larger areas on the sample surface providing a representative overview of the respective specimen. In contrast to TEM where the electrons pass through the specimen and create “direct” images, is the image in SEM generated by backscattered electrons providing “indirect” images.

A bundled electron beam (the so called primary beam), which contains electrons accelerated by an electric potential in the range of only 1-40 keV, is scanning the sample surface. The electron beam impinges on the specimen surface and interaction processes take place. These processes can be classified into elastic and inelastic scattering. Elastic scattering involves electrons which get deflected by the positively charged atomic nuclei thereby changing their trajectory without any loss in energy. The electrons which leave the sample again due to single or multiple scattering effects are called backscattered electrons. They possess energies in the same order of magnitude as the primary beam. Inelastic scattering occurs when primary electrons lose a part of their energy because of the interaction with the atomic shell or the atomic nuclei. They transfer a part of their energy to the electrons in the sample surface resulting in the emission of secondary electrons. These secondary electrons typically exhibit energies in the range of 10-50 eV and are rather “slow” with low kinetic energies. Therefore, the ones escaping from the specimen and collected by the detector are generated close to the surface (5 to 50 nm) thus leading to the possibility of probing the sample surface. The aforementioned backscattered electrons can also be used to image the sample surface providing a good material contrast. However, this mode is less surface sensitive since the penetration depth of the backscattered electrons is in the range of some 100 nm.

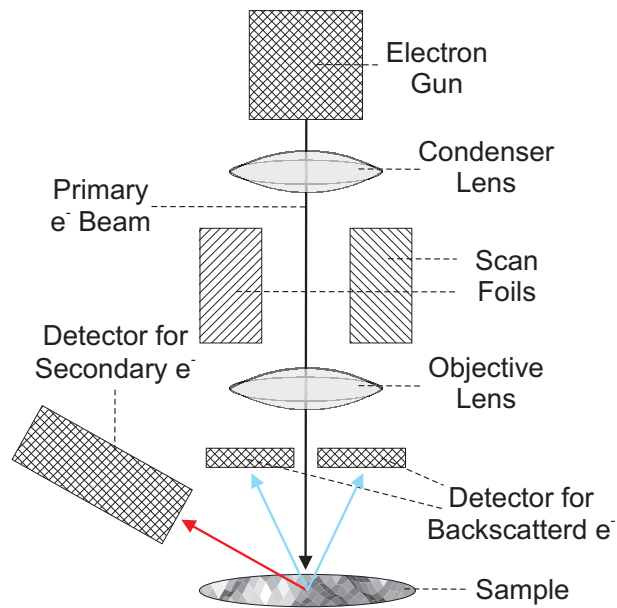


Figure 4.10: Schematic illustration of a typical SEM setup.

The setup of a typical SEM can be seen in Figure 4.10. It consists of an electron gun equipped with a filament cathode to create the electron beam. Similar to TEM, the electron source can either be a heated tungsten filament, a LaB_6 cathode or a field emission cathode. The beam is then focused by one or two condenser lenses. An objective lens projects the beam onto the sample surface and scan coils are used to deflect the beam making it possible to record the image of the specimen in a raster fashion.

5 Experimental Details

From previous sections it could already be seen that various molecules and experimental techniques are employed. Therefore, this chapter is devoted to give a detailed description of the respective substrate preparations together with the experimental setups used in the framework of this thesis.

5.1 Substrate Preparation

The successful growth of organic semiconducting films depends crucially on the substrate preparation. The substrate material itself already determines many structural features of the subsequent growth taking place. Moreover, the (nano)structuring of the surface has an impact on the growth mode. Beside all this aspects, it is essential to have a clean surface free of contaminants and water in order to draw the right conclusion about the film growth, morphology and structure of the respective molecule. The substrates used in this thesis are $\text{Al}_2\text{O}_3(11\bar{2}0)$ and $\text{Si}(100)$ wafers covered by a native oxide layer (SiO_2), modified by arrays of either gold (Au), platinum (Pt) or palladium (Pd) nanoparticles and a $\text{Cu}(100)$ single crystal surface. In addition, the same $\text{Si}(100)$ wafers were used for the deposition of nanopatterned gold films. All preparation procedures are described in detail in the following.

5.1.1 $\text{Al}_2\text{O}_3(11\bar{2}0)$ and $\text{Si}(100)/\text{SiO}_2$

$\text{Al}_2\text{O}_3(11\bar{2}0)$ substrates were cleaned by successive ultrasonic baths with acetone and ethanol for about ten minutes. After the last cycle the substrates were immediately dried in a nitrogen stream. Finally, they were transferred into the UHV system where they

were annealed overnight at about 500° C and subsequently cooled down to the growth temperature. The Si(100) wafers with native oxide were prepared in the same way.

5.1.2 Si(100)/SiO₂ modified by Au, Pt, and Pd nanoparticles

The Si(100) wafers with SiO₂ were coated by Au, Pt and Pd nanoparticles whose diameters and interparticle distances are adjustable. For this purpose, the method of block copolymer micellar nanolithography is used which exploits the self-assembly properties of polystyrene-*b*-poly(2)-vinylpyridine diblock copolymer micelles into uniform monomolecular films onto solid substrates [124–127]. The diblock copolymers are dissolved in toluene forming uniform spherical micelles. Depending on the desired material of the nanoparticle (Au, Pt or Pd), metal salts are added (HAuCl₄, H₂PtCl₆ or Pd(Ac)₂). After stirring for 24 hours, all of the respective metal salt is dissolved and the substrate can be immersed into this solution and retracted with a certain velocity. During retraction, a micellar monolayer self-assembles on the surface as shown in Figure 5.1 (a) and (b). Afterwards, the polymer shell is removed by hydrogen plasma treatment of the substrate resulting in an extended array of nanoparticles on top of the Si wafer as demonstrated in Figure 5.1 (c).

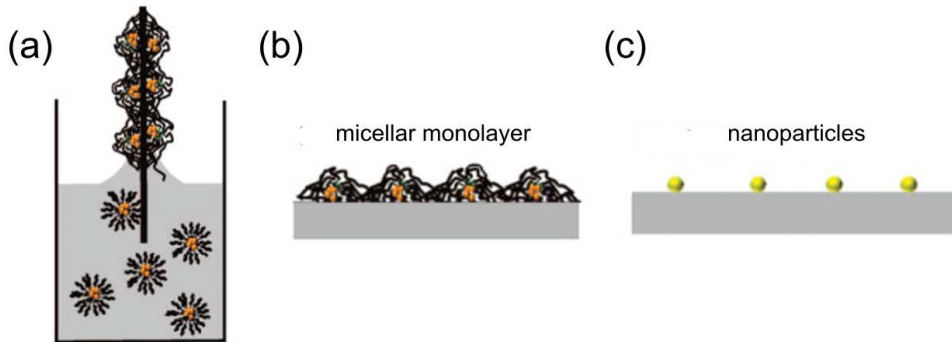


Figure 5.1: Illustration of the fabrication process. (a) The substrate is retracted from a toluene solution of metal salt loaded micelles. (b) Thereby, a micellar monolayer forms on the surface. (c) The polymer shell is removed by hydrogen plasma treatment resulting in an extended array of metal nanoparticles (from reference [126]).

5.1.3 Cu(100)

The Cu(100) crystal was prepared by polishing followed by subsequent sputtering and annealing cycles in the UHV chamber. The argon sputtering was carried out at a pressure of 1.5 to $2 \cdot 10^{-4}$ mbar with an emission current of 30 mA and an energy of 800 to 900 eV. The annealing temperature was between 500 to 670° C. As the surface conditions improved the sputtering and annealing cycles were reduced from about one hour to 30 minutes.

5.1.4 Nanopatterned Gold Films

The nanopatterned gold films or polycrystalline gold islands were created by electron beam lithography in a SEM. The patterns could be found within an 50 by 50 micrometer square among each was containing rings of gold islands with increasing diameters. The preparation included several steps as shown in Figure 5.2. (a) First, the sample was covered with polymethylmethacrylat (PMMA) which is a resist sensitive to exposure to high

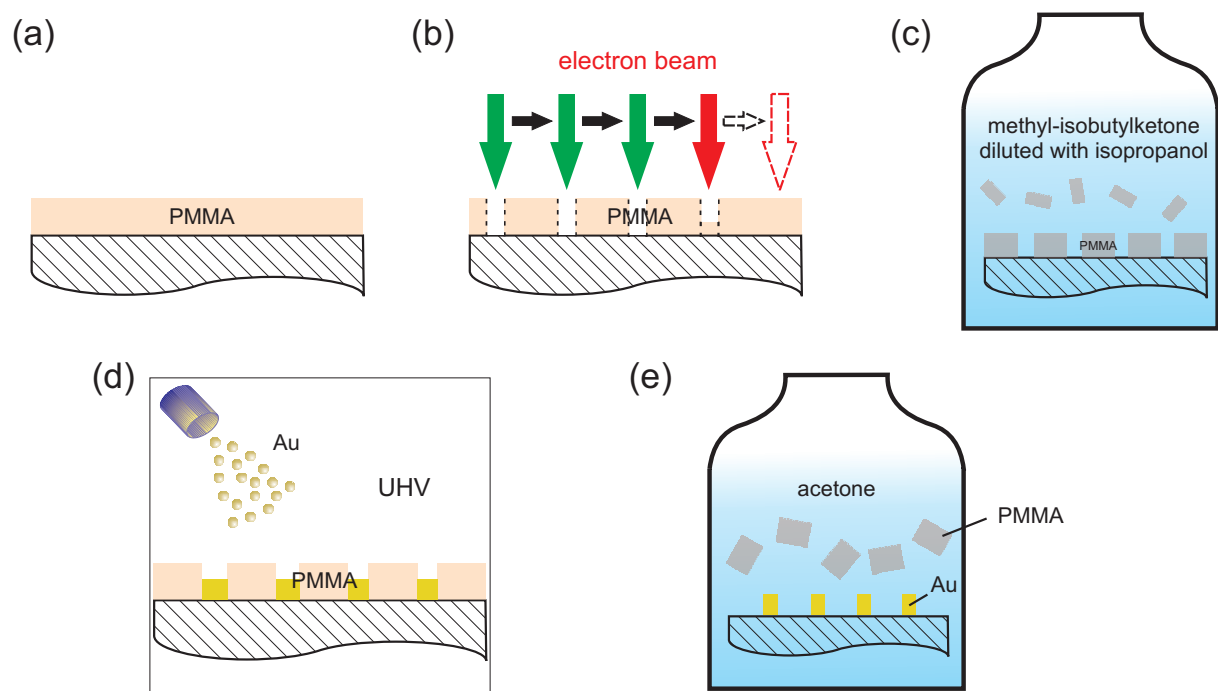


Figure 5.2: Illustration of the single steps during the formation of gold islands. The particular steps are described in the text.

energy particles [128]. PMMA is a polymer build up by monomers with chemical formula $(C_5H_8O_2)_x$. (b) As a result of the interaction between the high energetic electrons from the beam and the covalently binded electrons from the molecule, the chains of the polymer break in regions where they are exposed by the electron beam. The desired patterns could be read in by a computer connected to the SEM. (c) The next step consisted of the dissolution of the broken molecules in methyl-isobutylketone diluted with isopropanol to make sure that only the exposed areas are removed. (d) Afterwards, the substrate was transferred into an UHV system where the evaporation of the gold film took place. (e) In a last step, the residual polymers were dissolved in acetone (also called lift-off) being left over with the gold islands.

5.2 Organic Molecules

Pentacene and all phthalocyanines derivatives used in this thesis were purchased at Sigma Aldrich with purities ranging between 98 % to 99 %. PTCDI- C_8 was synthesized by the Institut für Organische Chemie at the Universität Würzburg. Prior to film growth all organic compounds were purified by gradient sublimation at the 3. Physikalisches Institut of the Universität Stuttgart.

5.3 Organic Molecular Beam Deposition

For all substrates presented in the previous section organic molecular beam deposition (OMBD) was applied in order to grow thin films of high purity. As already mentioned earlier, OMBD ensures a very good control over the structure, growth and morphology of organic semiconducting films since it allows a fine tuning of the substrate temperature, deposition rate and film thickness. The samples were prepared in three different systems consisting of a Omicron and JEOL system, both stationary and commercially available, and a portable home-built UHV chamber.

5.3.1 Omicron UHV chamber

The Omicron system, shown in Figure 5.3, can be basically divided into three chambers: the load lock system, the deposition chamber and the analysis chamber. All of them are

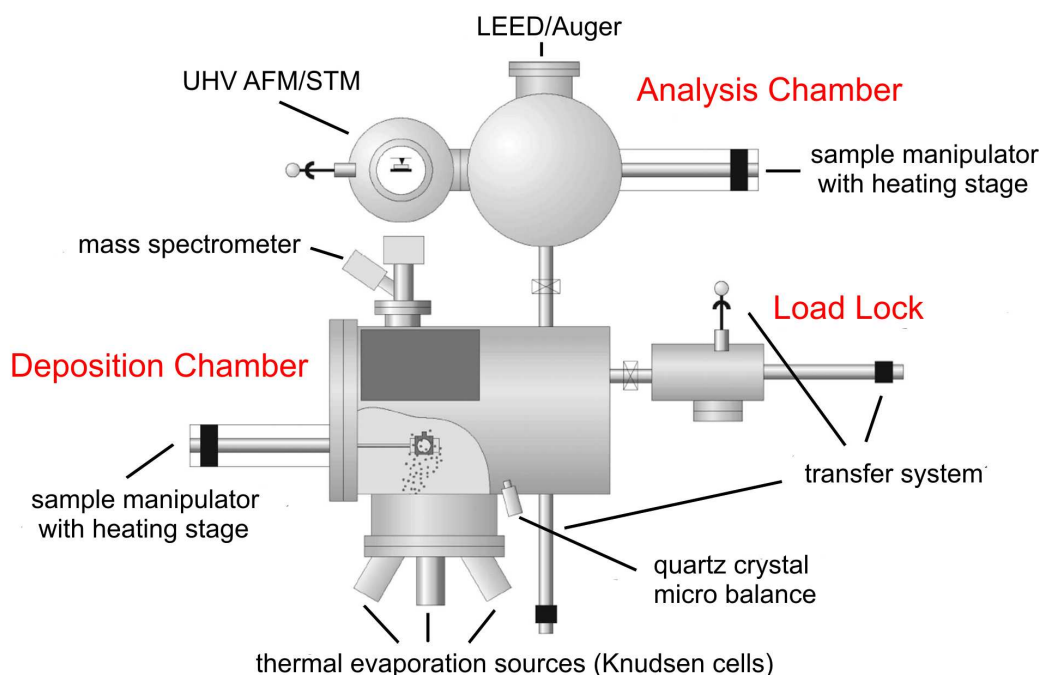


Figure 5.3: Schematic top view of the Omicron UHV system which consists of a load lock, a deposition chamber and an analysis chamber all connected with each other by transfer bars. In order to achieve UHV all three parts can be separated from each other by valves (from Ref. [129]).

connected via a transfer system which allows a substrate movement to all parts without breaking the vacuum. The load lock system guarantees a fast insertion of substrates and is, due to a rather small size, pumped down to a base pressure of 10^{-6} mbar within one hour.

The deposition chamber is equipped with four Knudsen cells to assure a controlled deposition of the respective molecule. The sample manipulator can be heated up to allow various substrate temperatures during growth. The thickness and deposition rate of the grown films are monitored by a quartz crystal micro balance. The evaporation temperature is measured by either C- or K-type thermocouples. In order to ensure stabilized temperature measurements Eurotherm controllers are used regulating the current which is responsible for heating up the filled crucibles in the Knudsen cells.

The analysis chamber contains a sputter gun and a sample manipulator with heating stage to make a preparation of single crystal surfaces possible. The characterization of the surface can be done by either a combined AFM/STM system or a combined low energy

electron diffraction/Auger electron spectroscopy setup.

The base pressure of the growth and analysis chamber are in the range of 10^{-10} to 10^{-11} mbar which is obtained by a combination of turbo-molecular pumps with additional ion-pumps and titanium sublimation pumps for each chamber. All three parts of the system can be separated from each other in order to keep this very low pressure.

5.3.2 JEOL UHV chamber

The JEOL system consists as well of three independent chambers as can be seen in Figure 5.4. The load lock allows again a fast sample insertion and is connected to the deposition chamber which is equipped with two Knudsen cells. A sputter gun and a sample manipulator with heating stage assures the preparation of single crystals. The analysis chamber exhibits a variable temperature STM. The whole system is pumped down to pressures of about 10^{-9} to 10^{-10} mbar and is bedded on an air-suspended table in order to reduce noise.

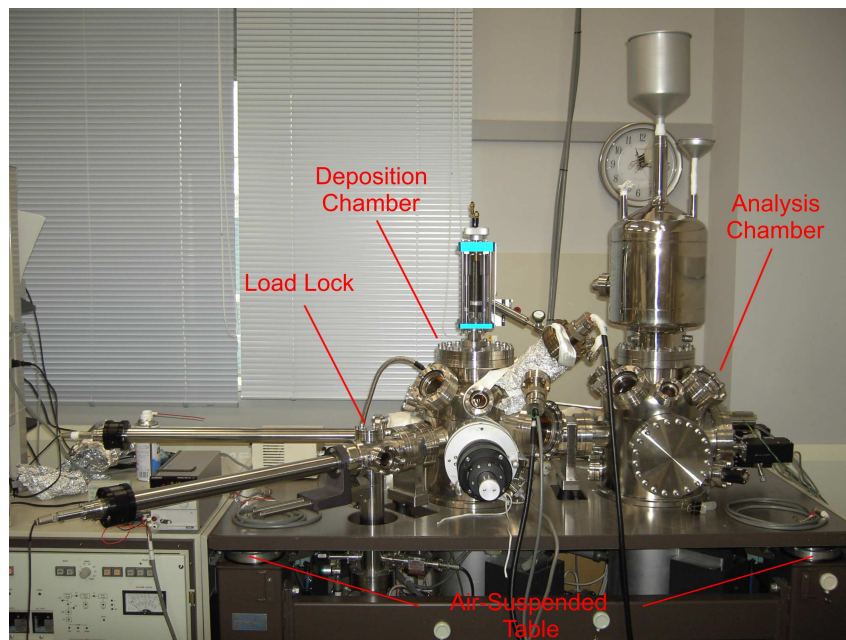


Figure 5.4: The JEOL UHV system which consists of a load lock, a deposition chamber and an analysis chamber all bedded on an air-suspended table in order to reduce noise.

5.3.3 Portable UHV chamber

The design of the portable UHV chamber allows in-situ characterizations by x-rays. For this purpose, the chamber is portable and can be mounted on standard diffractometer tables as shown in Figure 5.5. It is equipped with three Knudsen cells and a sample holder which is able to vary the substrate temperature. A beryllium window of 1 mm thickness guarantees a low x-ray absorption and a high transfer of x-ray intensity through the chamber to the detector. A system of membrane and turbo-molecular pump enables a base pressure of 10^{-8} mbar.

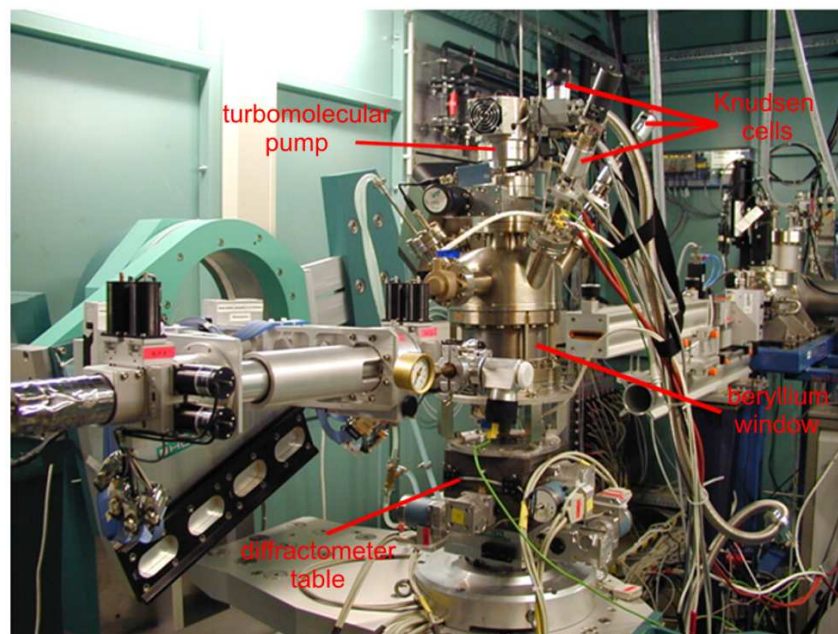


Figure 5.5: Portable UHV chamber mounted on the diffractometer table of the MPI-MF beamline at the Ångströmquelle Karlsruhe.

5.4 AFM in Air

All samples were measured by a commercial Nanotec AFM under ambient conditions which could be employed in contact mode, jumping mode and tapping mode. The AFM was equipped with two different piezoelectric tubes allowing scan areas from nanometer size up to several microns. Silicon nitride tips attached on cantilever with spring constants

of 0.01 N/m, 0.03 N/m, 0.1 N/m and 0.5 N/m were used. The image processing was performed by the help of the freeware WSxM [130].

5.5 Synchrotron Beamlines

Each synchrotron beamline is usually dedicated to carry out particular sample analysis techniques and therefore exhibits special characteristics in its setup. Thus, the next section is devoted to a more detailed description of the respective beamlines used for the experiments in this thesis which can be found either at the Ångströmquelle Karlsruhe (ANKA) or at the European Synchrotron Radiation Facility (ESRF).

5.5.1 MPI-MF Surface Diffraction Beamline at ANKA

This synchrotron consists of a storage ring operating at an electron energy of 2.5 GeV with a current of 200 mA. The beamline, as schematically shown in Figure 5.6, is a multi-purpose bending magnet beamline whose optics contain a rhodium coated silicon mirror for cutting the energy spectrum and for vertical beam focusing. A Si(111) double

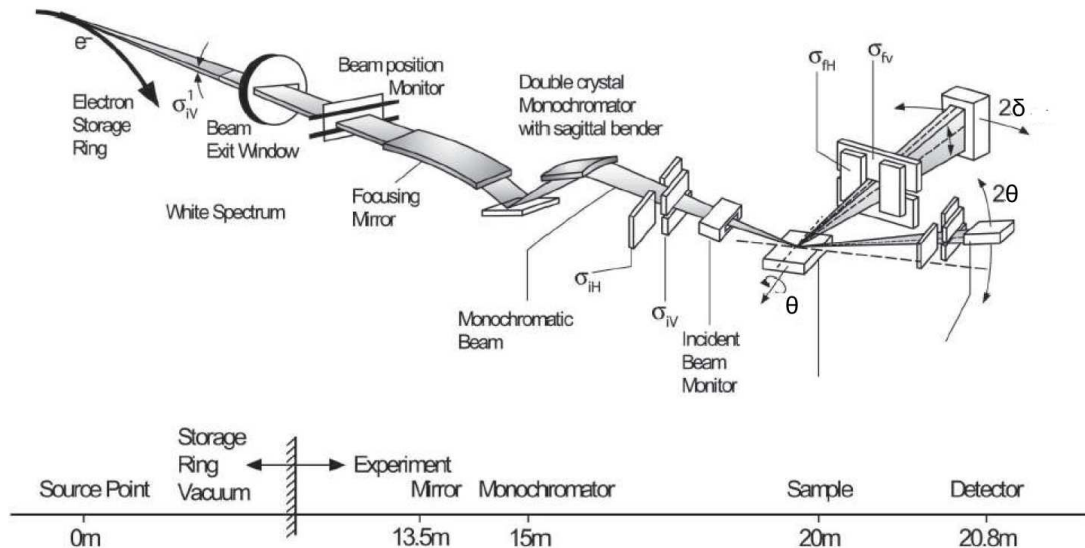


Figure 5.6: Schematic illustration of the MPI-MF surface diffraction beamline at ANKA with corresponding distances (from Ref. [131]).

crystal monochromator is able to adjust the energy within a range of 6-20 keV giving an energy resolution of 10^{-4} . The multi-circle (2+3) diffractometer can be employed with different ultra high vacuum (UHV) chambers and detectors allowing vertical and horizontal diffraction geometry for the experiments. The beam width and the resolution can be varied by horizontal (σ_{iH} , σ_{fH}) and vertical (σ_{iV} , σ_{fV}) slits situated in front of the sample and between the sample and the detector, respectively. For a specular scan the sample is tilted with respect to the incoming beam by the angle α_i and the detector by $2\alpha_i$ keeping θ_{HK0} at 0° [131]. For GIXD-scans the detector rotates along $2\theta_{HK0}$ thereby setting $2\alpha_i$ to the critical angle $2\alpha_{crit}$.¹

5.5.2 ID10B at the ESRF

The ESRF runs a storage ring at 6 GeV injecting a current of 200 mA. The ID10B beamline itself is a multi-purpose, high-brilliance undulator beamline and is dedicated for high resolution x-ray scattering and surface diffraction on solid and on liquid interfaces, combining GIXD and x-ray reflectivity. Its optics consist of a diamond (111) and (220) double crystal monochromator with an intrinsic energy resolution $\Delta E/E$ of $5.9 \cdot 10^{-5}$ and $2.3 \cdot 10^{-5}$, respectively. The energy can be tuned from 8-13 keV for the (111) and from 13-22 keV for the (220) diamond. In order to suppress higher harmonics a double-mirror setup is installed. The diffractometer is able to perform scattering experiments in both horizontal and in vertical scattering geometry.²

¹More detailed information can be found at:

http://www.mf.mpg.de/en/abteilungen/dosch/anka/anka_en.shtml

²More detailed information can be found at:

<http://www.esrf.eu/UsersAndScience/Experiments/SCMatter/ID10B/>

6 3D Self-Assembly of PTCDI-C₈ Multilayer Films on Weak Interacting Surfaces

This chapter is devoted to give an insight into structural and morphological properties of PTCDI-C₈ films on SiO₂ and Al₂O₃. Success in achieving OFETs with high charge carrier mobility hinges on the ability to grow organic films with high crystallinity and a reduced number of structural defects and grain boundaries. The molecular orientation and packing in the film are crucial issues concerning the relationship structure-properties since they determine the intrinsic charge transport properties of the organic film and its anisotropic properties. The morphology of the film is also a critical factor since crystalline defects and grain boundaries generally result in a reduction of the effective mobility. Thus, the importance of the investigation of growth and structural properties has been recognized beyond the academic interest, especially on dielectric surfaces of technological relevance for OFETs, like amorphous SiO₂ and Al₂O₃.

Nevertheless, whereas the evolution of the morphology has been well investigated, the determination of the complete crystalline structure of very thin molecular films, i.e. unit cell parameters *and* molecular packing, is still a challenging experimental task, remaining unknown for most of the molecular systems. Important progress has been made by synchrotron x-ray diffraction experiments which have unraveled by grazing incidence the in-plane structure of the first layers in close proximity to the substrate interface [39, 41, 72, 88, 132]. These GIXD studies have revealed that the structure of very thin molecular films is often different from that of the bulk due to molecule-substrate

interactions. However, the low signal of the Bragg diffractions along with the lack of high crystalline order hinder the measurement of enough number of reflections to solve the complete crystal structure of thin organic films.

Only recently, the 3D structure determination of organic thin films has been made possible by virtue of a controlled thin film growth and a powerful analysis by surface-sensitive x-ray diffraction methods. Until now, reports exist for the most important organic p-type semiconductor, pentacene on SiO₂ [40, 90, 133], and for two other p-type organic materials [134, 135]. Therefore, together with the investigation of growth and morphology, two possible routes are presented in this chapter tackling the problem of a complete structural characterization of organic thin films on the example of PTCDI-C₈ on SiO₂ and Al₂O₃.

6.1 PTCDI-C₈ on SiO₂

6.1.1 Morphology and Growth Mode

AFM in contact mode was used to collect information about the morphology and growth mode. It can be seen that PTCDI-C₈ forms smooth layered films. Figure 6.1 (a) displays a typical topographical AFM image of a 270 Å thick PTCDI-C₈ film grown on SiO₂ at a substrate temperature of ~ 150 °C. Elongated terraces of several microns are observed

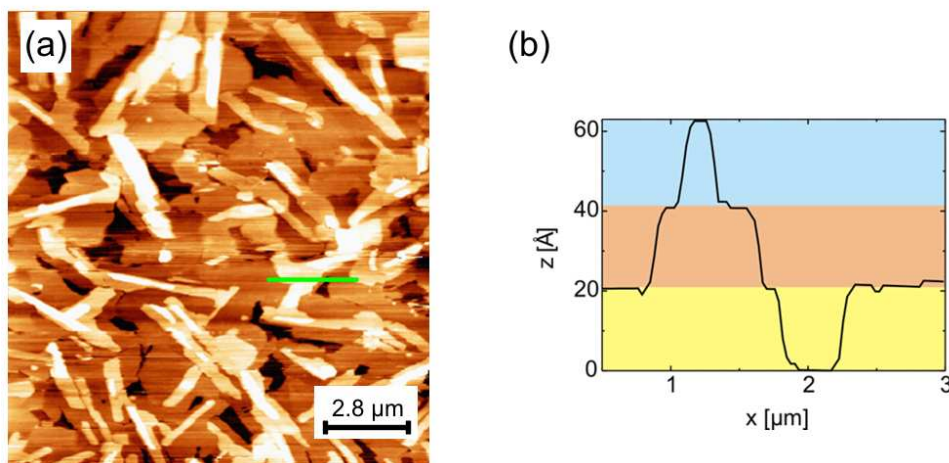


Figure 6.1: Contact AFM-image of the PTCDI-C₈ film grown at 150 °C. The film morphology reveals elongated islands with large planar terraces extended up to several microns.

separated by mono-molecular steps of $20.3 \pm 1.5 \text{ \AA}$, as shown in Figure 6.1 (b), which is in good accordance to previous studies [10]. Given the isotropy of the substrate surface, it is evident that the anisotropic shape of the islands obeys to the intrinsic anisotropy of the PTCDI-C₈ crystal. It is remarkable that the root mean square roughness of the film is of only 9.7 \AA , less than one molecular layer, which indicates that the growth takes place in a layer-by-layer fashion.

6.1.2 Structure and Molecular Packing

In what follows is a detailed structural analysis of PTCDI-C₈ films by the complementary use of x-ray reflectivity and GIXD. In addition, it will be shown how the combination of both techniques allow the disclosure of the molecular packing.

PTCDI-C₈ films exhibit an excellent degree of order perpendicular to the surface (out-of-plane) as observed by x-ray reflectivity measurements performed at ANKA with a wavelength of $\lambda = 1.3477 \text{ \AA}$. The data shown in Figure 6.2 correspond to a sample evap-

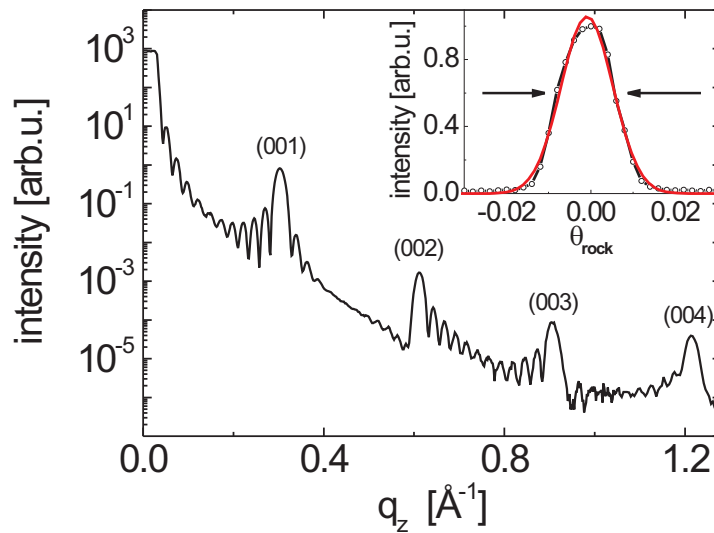


Figure 6.2: X-ray reflectivity curves after a post annealing of the substrate. The inset shows a rocking scan with its Gaussian fit (red curve) revealing the small mosaicity of the film.

orated with a deposition rate of 3-6 Å/min at a substrate temperature of 90 °C and post-annealed to 100 °C. These parameters turned out to be the optimal conditions for a highly ordered thin film structure which will be shown in the next section. Bragg reflections up to the fourth order as well as undamped Laue-oscillations around the first, second and third Bragg peak provide the indication of a highly ordered lamella structure with an out-of plane lattice of $d = 20.69$ Å. This is in very good agreement with MALENFANT et al. who proposed a spacing of ~ 20 Å and coincides with the height of the monomolecular terraces measured by AFM [10]. Further evidence of the excellent crystalline order is obtained from the analysis of the rocking curves measured at the Bragg reflections. The inset in Figure 6.2 shows a rocking scan of the third Bragg peak (red curve is the Gaussian fit). The small full width at half maximum ($\Delta\theta_{rock}$) of $0.0123 \pm 0.0002^\circ$ reveals a very good alignment of the (001) crystalline planes with respect to the surface, i.e. small mosaicity. The PTCDI-C₈ film is coherently ordered across its entire thickness due to the similar widths of the Kiessig fringes at low q_z -values, related to the total film thickness, and the Laue-oscillations, related to the coherently ordered film thickness.

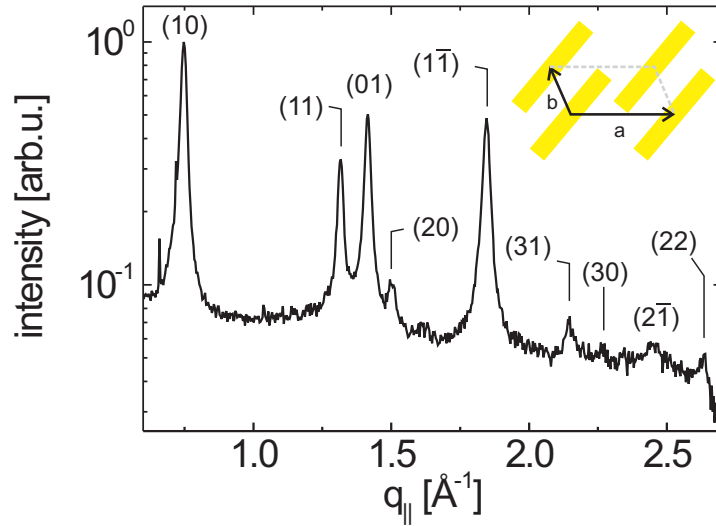


Figure 6.3: GIXD data of PTCDI-C₈ deposited on SiO₂ at room temperature (thickness of ~ 66 Å). From the in-plane Bragg reflections an oblique unit cell ($a = 9.14$ Å, $b = 4.83$ Å and $\gamma = 113.1^\circ$) can be deduced where the π - π stacking is directed along the b -axis.

Bragg reflection	1	2	3	4	5	6	7	8	9
$q_{ }$ [\AA^{-1}]	0.746	1.316	1.414	1.499	1.845	2.147	2.260	2.448	2.627
$d_{ }$ [\AA]	8.42	4.77	4.44	4.19	3.41	2.93	2.78	2.57	2.39
assignment	(10)	(11)	(01)	(20)	(1 $\bar{1}$)	(31)	(30)	(2 $\bar{1}$)	(22)

Table 6.1: Summary of the observed in-plane Bragg reflections and the proposed unit cell assignment.

GIXD, which allows to access the in-plane crystal structure of the films, has been carried out at the ESRF with a wavelength of $\lambda = 1.54613 \text{ \AA}$. The scan performed at room temperature under a critical angle of $\theta_{crit} = 0.20^\circ$ is shown in Figure 6.3 and discloses several Bragg reflections corresponding to lattice spacings summarized in Table 6.1. The GIXD data confirm that the films are crystalline and, by applying the relation

$$q_{||} = \sqrt{q_x^2 + q_y^2} = 2\pi \sqrt{(h/a)^2 + \left(-\frac{h}{a} \cdot \frac{\cos \gamma}{\sin \gamma} - \frac{k}{b} \cdot \frac{1}{\sin \gamma} \right)^2}, \quad (6.1)$$

the in-plane Bragg reflections can be assigned to an oblique cell with basis vectors $a = 9.14 \text{ \AA}$ and $b = 4.83 \text{ \AA}$ and an in-plane angle $\gamma = 113.1^\circ$. h and k are the corresponding Miller indices presented in Table 6.1 for the assignment. The structure contains one molecule per unit cell according to the dimensions of the in-plane lattice. The crystalline plane (001) is thus parallel to the substrate with PTCDI-C₈ molecules packed in a slipped cofacial alignment with the π - π stacking along the b -axis.

It could be seen that from a simple inspection of the specular x-ray data, many structural characteristics can be already determined as for instance the mean out-of plane lattice constant and the mosaicity. Note that the spacing between molecular layers ($d = 20.69 \text{ \AA}$) is considerably smaller than the length of the extended PTCDI-C₈ molecule ($\sim 29.8 \text{ \AA}$, see Figure 3.6). In principal, two configurations could be compatible with such reduced interlayer spacing in base of geometrical considerations: interdigitation between alkyl chains of adjacent molecular layers [14] or a certain tilt of the PTCDI core. Since the vertical structural features of the organic film are buried in the detailed x-ray intensity distribution along the specular rod, the reconstruction of the electron density profile

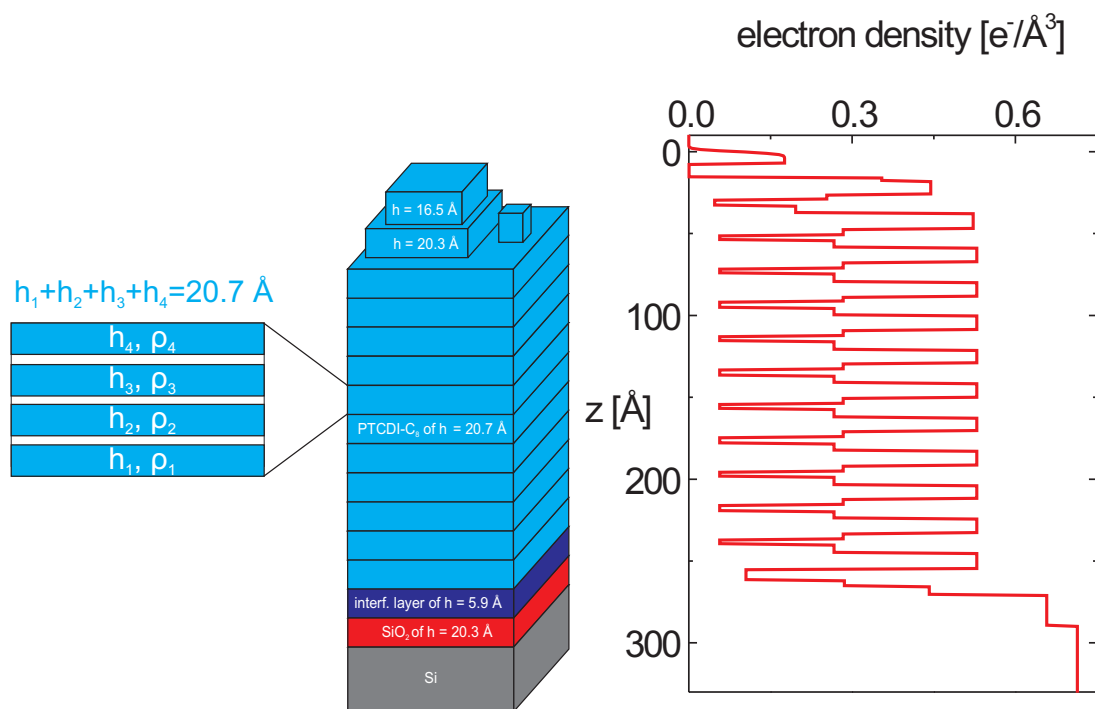


Figure 6.4: Scheme of the structural model described by the electron density profile.

$\rho(z)$ from the x-ray reflected data provides a way to deduce the molecular orientation. In other words, the shape of $\rho(z)$ is a fingerprint of the molecular orientation and packing and enables to discriminate between a tilted or an interdigitated configuration.

The electron density profile $\rho(z)$ has been obtained by a fit to the x-ray specular reflected intensity using the superfit program based on the Parratt formalism [101,136]. The structural model used to fit the x-ray specular data accounts for the substrate (silicon and SiO₂) and the PTCDI-C₈ multilayer (see Figure 6.4). An interfacial layer between SiO₂ and the organic multilayer was introduced to take into account possible structural differences at the silicon dioxide-organic interface (which are a consequence of the molecular interaction with the substrate). On top of this interfacial layer, n identical layers PTCDI-C₈ are considered. The internal electron profile of one molecular layer, which carries the aforementioned information about the molecular orientation, is described by four sub-boxes of different heights h_i and electron densities ρ_i . Notice that each PTCDI-C₈ box must consist of at least two sub-boxes since the molecule has two parts of well differentiated electron densities: the alkyl chain and the aromatic core. However, if a part of the alkyl chains of molecules in adjacent layers interdigitate as proposed for PTCDI-C₁₈ [14],

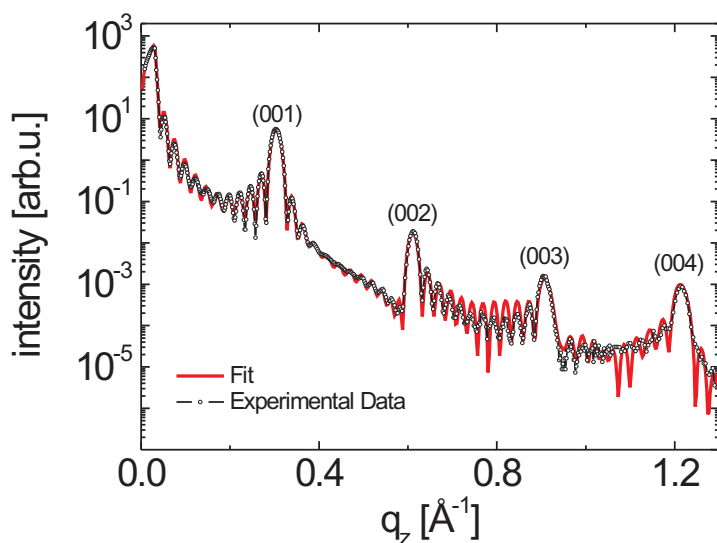


Figure 6.5: The red curve corresponds to the fitted intensity using a multilayer model for the electron density profile introduced in Figure 6.4.

a four sub-box model will be necessary to describe the electron density profile. It should be also mentioned that none of the boxes apart from the last one contains roughness to keep the number of fitting parameters as small as possible. In addition, m layers with varying electron density and interlayer distance account for the incomplete coverage of the terminating layers and for possible structural differences at the air-organic interface, respectively.

The best fit is shown in Figure 6.5 (red curve) belonging to the electron density profile depicted in Figure 6.4. A summary of the relevant parameters of the fitted model is provided in the appendix C.1. Note that the fit is able to reproduce the intensity of the four Bragg reflections as well as the asymmetry of the Laue-oscillations of the experimental data. The associated electron density profile discloses eleven full covered PTCDI-C₈ layers followed by two incomplete layers (observed as an electron density decrease). An interesting feature is that the height of the last layer exhibits a value of ~ 16.5 Å. This could be attributed to a more tilted configuration of the alkyl chains (away from the surface normal) to compensate the loss in cohesive energy at the organic-air interface due to their less dense packing or to a more tilted configuration of the overall molecule.

Now, one possible approach to determine the molecular tilt is to compare the electron density profile $\rho(z)$ obtained from the fit with a simple modeling of the electron density profile of a row of PTCDI-C₈ molecules stacked along the z -direction. Therefore, each z_i -position of every atom in the PTCDI-C₈ molecule is defined as the center of a Gaussian function

$$f(z) = \mu e^{(z-z_i)^2/\omega_r^2} \quad (6.2)$$

characterizing the positions of electrons. The area below each Gaussian curve, i.e. the integration of each Gaussian function, corresponds to the number of electrons of the respective atom and has to be normalized by the parameter μ . The parameter ω_r is given by the van-der Waals radius of the relevant atom and describes a spatial upper limit for the distance between electron and atomic nucleus. All parameters μ and ω_r for each atom in the PTCDI-C₈ molecule are summarized in Table 6.2. Summing up all the Gaussian curves for each atom results in the electron density profile in z -direction. In order to get the electron density, one has to divide the values of the electron density profile by the in-plane lattice area which is given by the in-plane unit cell $a \cdot b \cdot \sin \gamma = 40.61 \text{ \AA}^2$ determined above.

The best agreement between simulated and fitted electron density can be seen in Figure 6.6 (a). Here, the molecule was rotated around all three space axes and both alkyl chains were tilted around the axis lying in the plane of the molecular core and being perpendicular to the molecular core axis. It can be seen that the main features of the electron density profile are reproduced. In order to illustrate the sensitivity of this analysis the expected electron density profile for an interdigitated arrangement is also shown (gray curve) which is in clear discrepancy with our observations. The simulated x-ray intensity is in clear disagreement with the measured data and fails in reproducing the intensity of the Bragg reflections and the asymmetry of the Laue oscillations as shown in Figure 6.6

	H	C	O	N
$\mu [\text{\AA}^{-1}]$	$\frac{1}{1.2\sqrt{\pi}}$	$\frac{1}{1.7\sqrt{\pi}}$	$\frac{1}{1.52\sqrt{\pi}}$	$\frac{1}{1.55\sqrt{\pi}}$
$\omega_r [\text{\AA}]$	1.2	1.7	1.52	1.55

Table 6.2: Parameters for the Gaussian functions of each atom in the PTCDI-C₈ molecule for the simulated electron density profile.

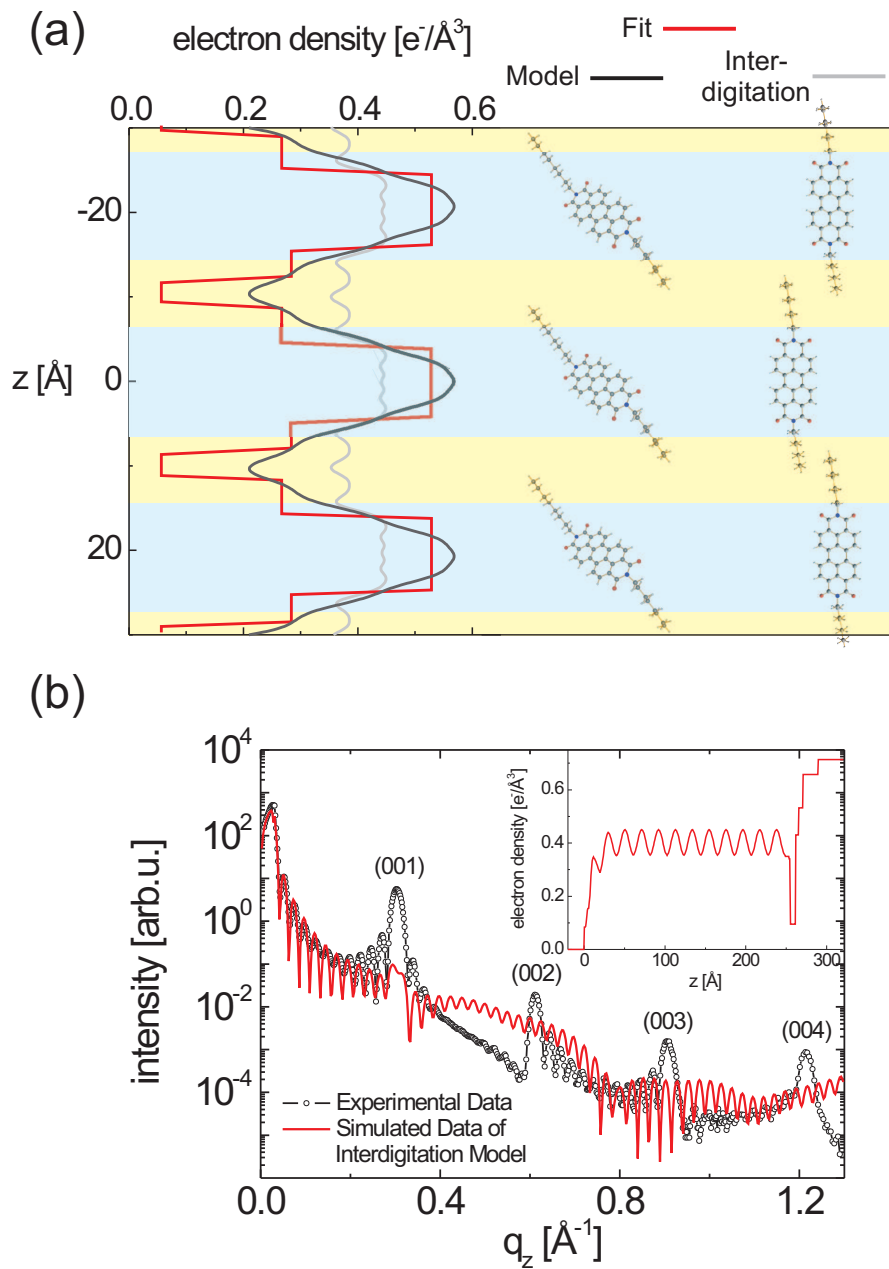


Figure 6.6: (a) Calculated electron density profile for a tilted configuration of PTCDI-C₈ molecules obtained after a rotation of the molecular core and a tilt of the alkyl chains (black curve). This electron density profile reproduces the main features of the electron density profile obtained from the fit of the x-ray specular data (red curve). The simulated electron density profile for an interdigitated configuration (gray curve) exhibits an obvious disagreement to the electron density profile obtained via the fit. (b) Simulated x-ray reflectivity and electron density profile (inset) if interdigitation of adjacent molecules is considered.

(b). The inset shows the corresponding electron density profile the interdigitated case. The parameters (ρ_i, h_i) for the substrate, the SiO₂ and the interfacial box are fixed for a reasonable comparison.

To conclude, this strong discrepancy rules out an interdigitated packing of the PTCDI-C₈ molecules. Instead, a tilted configuration with respect to the z -axis gives a better agreement and it can be determined that the perylene core of PTCDI-C₈ is tilted with respect to the surface plane by an angle of $\sim 65^\circ$ as depicted in Figure 6.6 (a).

6.1.3 Temperature Dependent Studies

As the improvement of the electrical performance is inevitably entangled to temperature-dependent molecular organization on the substrate, temperature-dependent structural

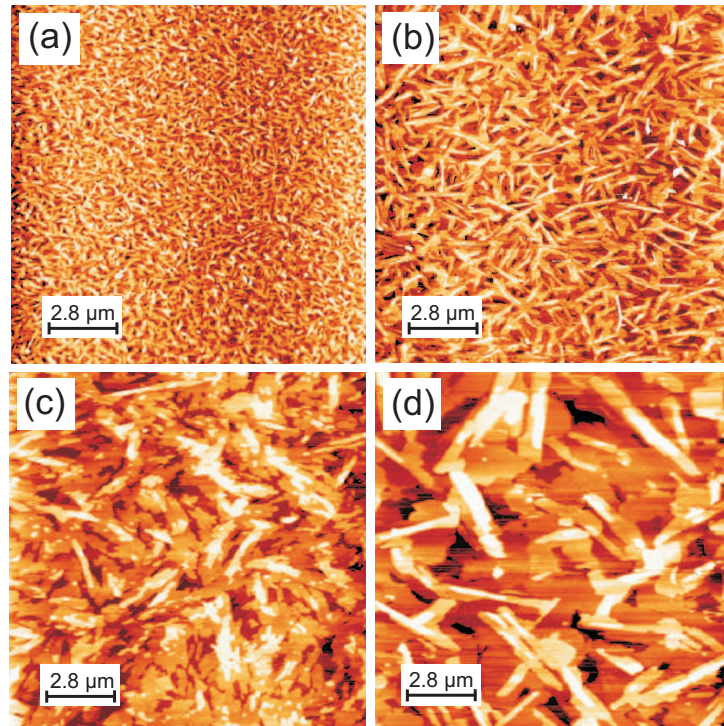


Figure 6.7: Contact AFM images of 270 Å thick PTCDI-C₈ films grown at (a) room temperature, (b) 70 °C, (c) 90 °C and (d) 150 °C (scan area: $14.0 \times 14.9 \mu\text{m}^2$). The film morphology undergoes an enlargement of the needle-like islands, from a typical length of ~ 500 nm at room temperature to elongated islands with large planar terraces extended up to several microns beyond $T_{sub} \sim 90$ °C.

data of thin films are a crucial input for a modeling of their properties and for further device optimization [26]. Therefore, a thorough characterization of the structural properties of PTCDI-C₈ films on SiO₂ as a function of both, growth and post-annealing temperatures have been performed.

The influence of the substrate temperature on the morphology is illustrated in Figure 6.7 (a) - (d) which shows typical topographical images of 270 Å thick PTCDI-C₈ films grown on SiO₂ at four different substrate temperatures (room temperature, 70 °C, 90 °C and 150 °C). The root mean square roughness drops from 17.5 Å at room temperature to 13.6 Å at $T_{sub} = 90$ °C and 9.7 Å at $T_{sub} = 150$ °C. With increasing substrate temperature, the length of the needle terraces (and grains) increases from ~ 500 nm to several microns (beyond 90 °C). Information about the degree of lateral crystalline order was collected by GIXD for different growth temperatures between room temperature and 150 °C. The mean size L of the crystalline domains along a certain crystallographic direction can be estimated from the inverse of the full width at half maximum of the corresponding in-plane Bragg reflection (see Figure 6.8) according to $L_{(hk0)} \approx 2\pi/\Delta q_{(hk0)}$. The domain size

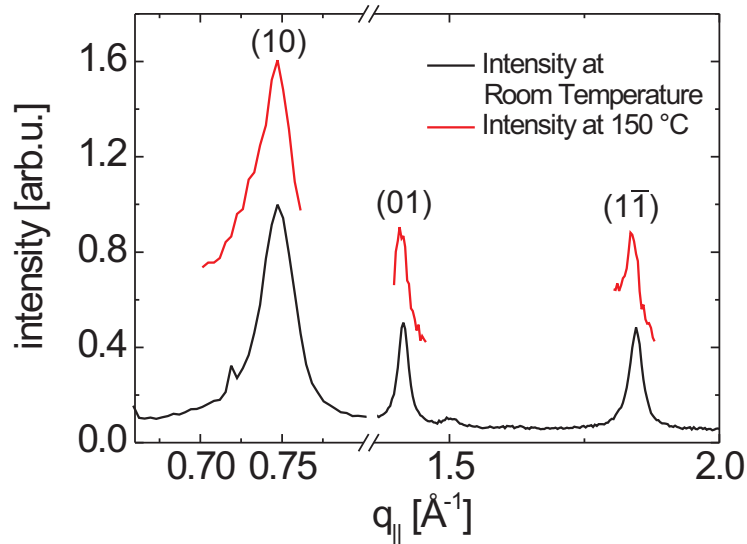


Figure 6.8: GIXD scan of the PTCDI-C₈-film at room temperature and $T_{sub} \sim 150$ °C.

estimated for the film grown at room temperature is $L_{(010)} \sim 280 \text{ \AA}$. This is considerably smaller than the characteristic island (and grain) length $L_I \sim 5000 \text{ \AA}$ observed by AFM. This evidences that molecular islands are polycrystalline. Moreover, unexpected similar widths of the (100) and (010) peaks ($\sim 270 \text{ \AA}$ and $\sim 280 \text{ \AA}$, respectively) indicate a rather isotropic growth along the different crystallographic directions, which differs from the expectation of a faster growth along the π - π stacking direction, i.e. along the [010] direction, as observed in the growth of PTCDI-C₈ single-crystals [20]. However, the elongated shape of monomolecular terraces suggest that, in spite of the small lateral crystalline coherence, orientational long-range order between crystallites exists with the mean direction of the b -axis pointing along the long axis of the terraces.

Surprisingly, similar domains sizes are found for the film grown at 150 °C in strong contrast to the micron-size length of monomolecular islands and terraces. Thus, with increasing growth temperature from room temperature to 150 °C, there is an enlargement of islands sizes (~ 10 times) but without significant growth of the lateral crystalline domains. The polycrystalline structure within organic islands has recently been observed for pentacene suggesting that polycrystallization evolved from a single nucleus is not a rare phenomenon in organic growth [137, 138]. For PTCDI-C₈, the two-dimensional (2D) domain boundaries are apparently no obstacle for an efficient charge transport accordingly to the high saturation electron mobility of $1.7 \text{ cm}^2/\text{Vs}$ [11]. Quantum mechanical calculations for PTCDI-C₅ have disclosed that substantial π - π orbital overlap and intermolecular charge delocalization exist not only along the [010] but also along the [110] direction [11]. Thus, it is plausible that the average orientational alignment of PTCDI-C₈ 2D crystalline domains guarantees sufficient π - π orbital overlap across domain boundaries within the islands (or needle grains). Thus, a major factor responsible for the improvement of effective field effect mobility with increasing growth temperature [11] is the reduction in the density of 3D grain boundaries (as observed in the topographic AFM images) due to a decrease of the overall film resistance.

It is reported that a post-thermal treatment successfully improves the electron mobility in OFETs [44]. Here, we have investigated the impact of post-annealing on the crystallinity of films grown at $T_{sub} \sim 90 \text{ °C}$ (thickness of 270 \AA) since this is an adequate growth temperature for good multilayer order. The film has been annealed stepwise from room temperature to 200 °C and characterized for each temperature by specular x-ray reflection

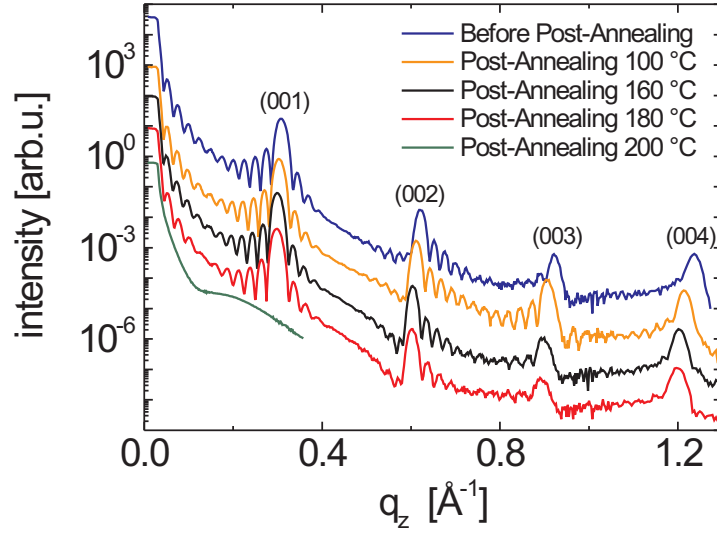


Figure 6.9: X-ray specular reflection curves of the PTCDI-C₈ film grown at 90 °C and post-annealed to different substrate temperatures.

It can be seen from Figure 6.9 that a significant improvement of the out-of plane structure is taking place by a mild annealing to 100 °C visibly manifested in the pronounced Laue-oscillations between the second and third Bragg reflection (less damped than at room temperature). Post-annealing to 180 °C causes the disappearance of two Laue-oscillations evidencing desorption of the last two molecular layers and therefore the onset of molecular desorption, which is indeed completed at 200 °C. The shift of the Bragg reflections towards smaller momentum transfer values q_z is due to thermal expansion perpendicular to the molecular layers.

6.2 PTCDI-C₈ on Al₂O₃

As already mentioned, the particular challenge in the design of functional organic thin films is related to the highly anisotropic properties of the organic molecules which, in turn, define the anisotropic properties of organic films on a macroscopic scale. Hence, the determination of molecular orientation and packing of organic semiconductors in the thin film geometry (which may be significantly different from its bulk structure) is a crucial

input for modeling the electronic band structure and the associated intrinsic charge transport properties [133, 139–141]. In the previous section, it was shown that the combination of GIXD and x-ray reflectivity enables the determination of the interlayer spacing, the in-plane unit cell and the tilt of the molecule. However, the lattice parameter c and the angles α and β of the unit cell remain still unknown as well as the azimuthal orientation. This section presents a possible route to elucidate the full molecular packing and structural characteristics on a Al₂O₃ (11 $\bar{2}$ 0) substrate.

6.2.1 Structure and 3D Molecular Packing

The molecules were evaporated by OMBD in UHV with a growth rate of 3–6 Å/min on an Al₂O₃ (11 $\bar{2}$ 0) substrate kept at 150 °C. PTCDI-C₈ shows a weak van der Waals interaction with the substrate giving rise to films with an outstanding degree of crystalline order. The crystalline domains in the organic film exhibit a random azimuthal orientation on the surface. As a direct monitor of the film quality the specular x-ray intensity was

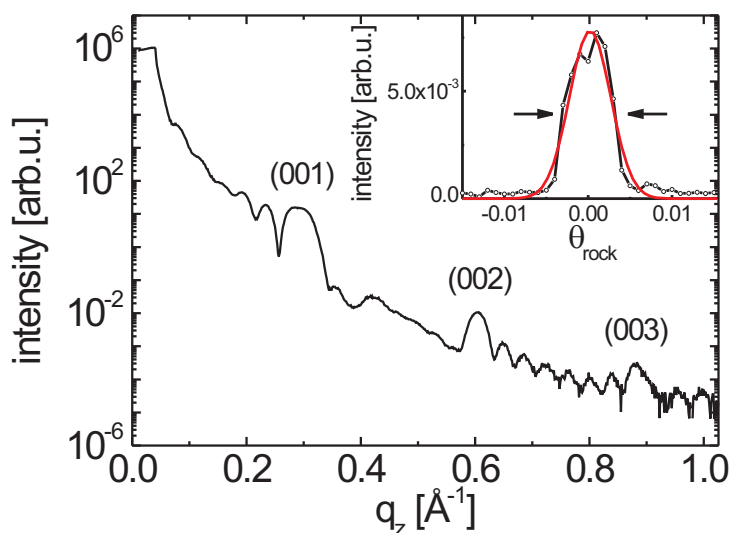


Figure 6.10: X-ray specular reflection curve of a PTCDI-C₈ film grown at 150 °C on Al₂O₃. The inset shows the rocking scan of the second Bragg peak revealing an excellent alignment of the (001) crystalline planes with respect to the growth direction.

recorded which is shown in Figure 6.10. The scattered intensity exhibits Bragg reflections with well defined Laue-oscillations which are characteristic for a highly ordered lamella structure. From the data, a distance between adjacent layers of $d \sim 20.8 \text{ \AA}$ can be extracted (as measured at $150 \text{ }^\circ\text{C}$) as well as a total film thickness of $D \sim 182 \text{ \AA}$ (about 8.7 layers). The width of the Bragg rocking scans reveal an excellent alignment (better than 0.005°) of the (001) crystalline planes with respect to the growth direction as shown in the inset of Figure 6.10. Note the similar interlayer spacing with films on SiO₂. Because a better structural order can be observed at $150 \text{ }^\circ\text{C}$, as disclosed by more pronounced Laue oscillations, a detailed analysis of the 3D molecular packing has been performed at this temperature.

The 3D x-ray crystallography was carried out at the beamline ID10B of the European Synchrotron Radiation Facility (ESRF) with a wavelength of $\lambda = 1.5461 \text{ \AA}$ and at an incident angle close to the critical angle of the substrate (0.20°). The scattered intensity was recorded by a 1-dimensional (1D) detector as schematically shown in Figure 6.11 and is plotted as a function of the momentum transfer q_{\parallel} , q_z , parallel and perpendicular to the surface respectively.

The 2D plot in reciprocal space of the PTCDI-C₈ film on Al₂O₃ is illustrated in Figure 6.12 (a) where the color code corresponds to the collected intensity recorded by the 1D detector. Figure 6.12 (b) shows the corresponding three dimensional view of Figure 6.12 (a). The pronounced intensity rods with Bragg diffraction peaks up to the fourth order, which can be observed at different q_{\parallel} positions, disclose again an extraordinary crystalline order of the organic film.

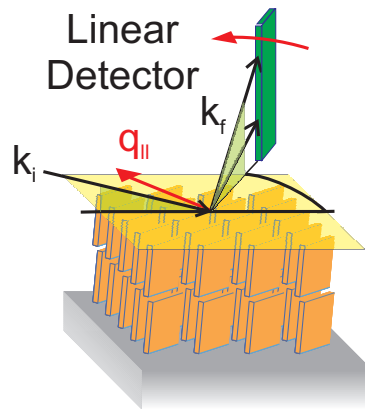


Figure 6.11: Schematic of the scattering geometry using a 1D detector.

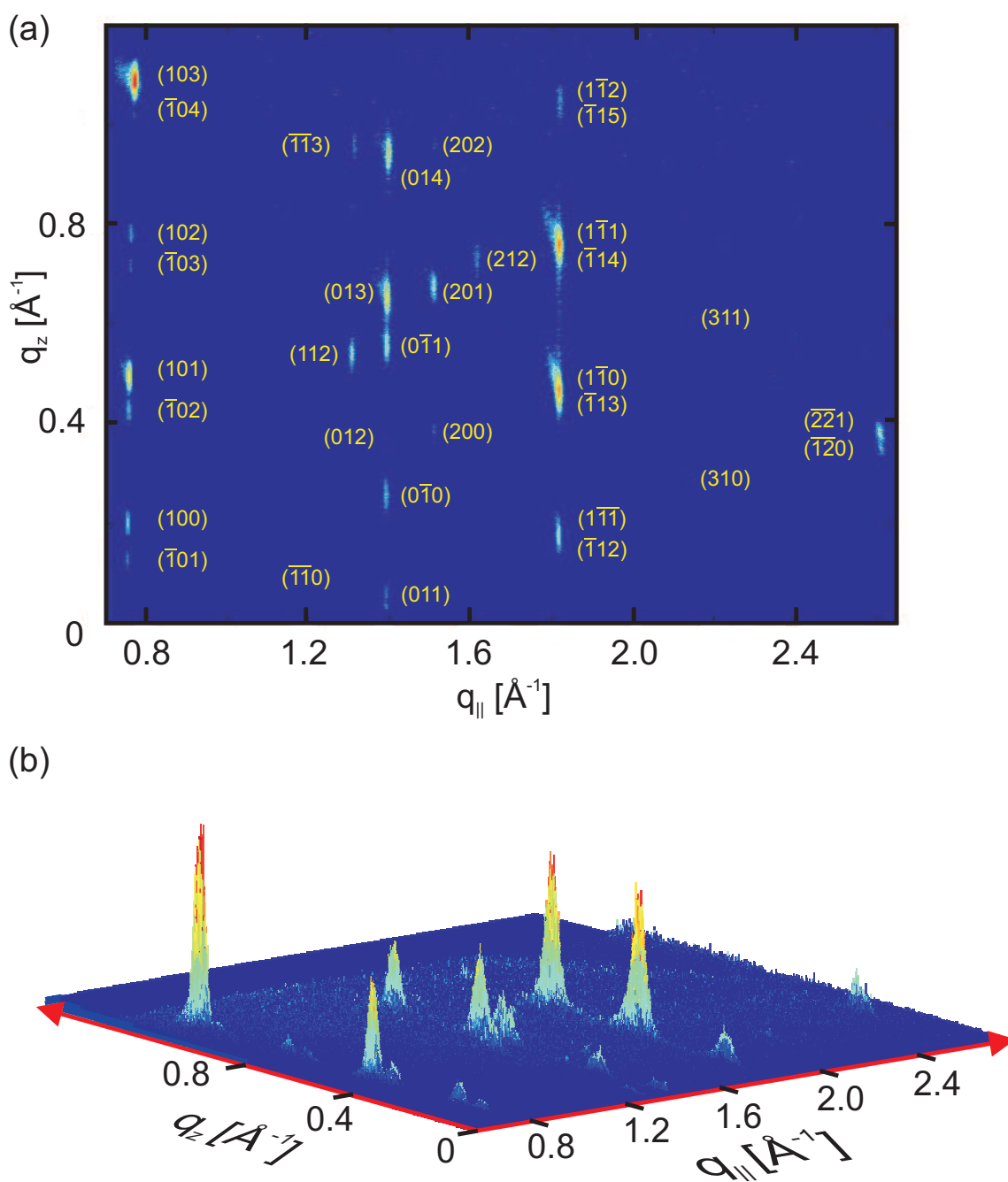


Figure 6.12: (a) Reciprocal map of the PTCDI-C₈ film on Al₂O₃ (11 $\bar{2}$ 0) measured by grazing incidence using a 1D-detector. The Bragg reflections are assigned to a triclinic lattice with one molecule per unit cell. (b) 3D representation of the collected intensity.

In a first step of the data analysis, the unit cell parameters have been deduced from the positions of the Bragg peaks. The associated transformation of the collected data from real space to reciprocal space is summarized in appendix A. Instead of determining immediately all three lattice vectors and angles, a cross sectional scan of the 2D plot was taken in order to determine the in-plane unit cell via equation 6.1. It turns out that the in-plane unit cell can be described by the lattice parameters $a = 9.00 \text{ \AA}$ and $b = 4.89 \text{ \AA}$ and by an angle of $\gamma = 112.8^\circ$ thereby containing one molecule. The in-plane unit cell deviates from the one derived for PTCDI-C₈ on SiO₂ by less than 1 %. Hence, the same thin film structure of PTCDI-C₈ on Al₂O₃ and on SiO₂ is expected considering the weak molecule-substrate interaction on both surfaces. The relationship

$$q_z = 2\pi \cdot \frac{\left[\frac{h}{a} \cdot \left(\cos \gamma \cdot \frac{\cos \alpha - \cos \beta \cdot \cos \gamma}{\sin \gamma} - \sin \gamma \cdot \cos \gamma \right) + \frac{k}{b} \cdot \frac{\cos \alpha - \cos \beta \cdot \cos \gamma}{\sin \gamma} + \frac{l}{c} \cdot \sin \gamma \right]}{\sqrt{1 - \cos^2 \beta - \cos^2 \gamma + 2 \cdot \cos \alpha \cdot \cos \beta \cdot \cos \gamma}} \quad (6.3)$$

has been employed for the determination of the remaining parameters c , α , β and the assignment of the Bragg reflections displayed in Figure 6.12. The structure of PTCDI-C₈ films consists of a primitive triclinic unit cell with $a = 9.00 \text{ \AA}$, $b = 4.89 \text{ \AA}$, $c = 21.65 \text{ \AA}$, $\alpha = 95.0^\circ$, $\beta = 100.7^\circ$ and $\gamma = 112.8^\circ$ where the a - b plane is parallel to the surface. The crystal structure for the PTCDI-C₈ thin film differs considerably from the bulk structure recently obtained from millimeter long needles of PTCDI-C₈ ($a = 8.50 \text{ \AA}$, $b = 4.68 \text{ \AA}$, $c = 19.72 \text{ \AA}$, $\alpha = 88.43^\circ$, $\beta = 94.01^\circ$ and $\gamma = 97.21^\circ$) [20]. The major differences are found in the larger values of the c lattice parameter and γ angle for the thin film structure.

In a second step, the orientation of the molecule within the unit cell was determined by a model fit to the Bragg intensities. As the PTCDI-C₈ molecule is large and strongly anisotropic, the intensity pattern is strongly modulated by the molecular structure factor. The intensity of each Bragg reflection was integrated and then, after standard corrections, [142, 143] compared to the calculated square modulus of the molecular structure factor associated with all possible rotations of PTCDI-C₈ within the unit cell. Six angles are used to define the orientation of the PTCDI-C₈ molecule: three rotation angles for the orientation of the aromatic core within the unit cell and three for the alkyl chains considered as rigid (see Figure 6.13). The assumption of rigid alkyl chains is physically reasonable since this conformation leads to the closest chain packing and keeps in addition the number of fit parameters low. However, a certain bending (as found in the

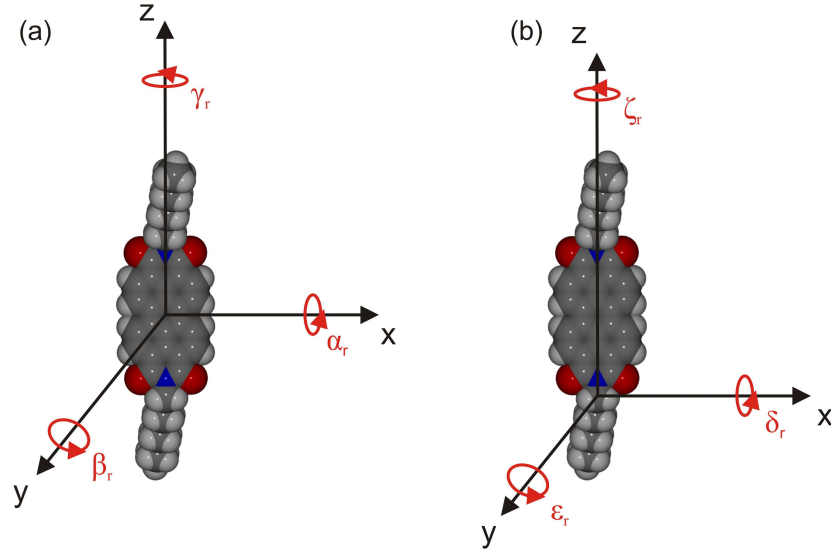


Figure 6.13: Illustration of the six rotation angles used for determining the structure factor. (a) Three angles are used to rotate the whole molecule and (b) three angles are applied to rotate both alkyl chains around the first carbon atom of each alkyl chain.

bulk structure of PTCDI-C₈) or gauche defects could exist which may become detectable by extending the crystallographic study to higher Fourier components. The theoretically calculated structure factor can be expressed by

$$F = \sum_{j=1}^{42} f_H \cdot e^{i\mathbf{q} \cdot \mathbf{r}_j^H} + \sum_{j=1}^{40} f_C \cdot e^{i\mathbf{q} \cdot \mathbf{r}_j^C} + \sum_{j=1}^4 f_O \cdot e^{i\mathbf{q} \cdot \mathbf{r}_j^O} + \sum_{j=1}^2 f_N \cdot e^{i\mathbf{q} \cdot \mathbf{r}_j^N} \quad (6.4)$$

with

$$\mathbf{q} = \begin{pmatrix} q_x \\ q_y \\ q_z \end{pmatrix} \quad (6.5)$$

being the momentum transfer components from equation 6.1 and 6.3 and \mathbf{r}_j^X representing the coordinates of each type of atom belonging to the PTCDI-C₈ molecule which can be arbitrarily rotated. The parameters used for the atomic form factor f_X can be found in the appendix D. The best fit is obtained for $\alpha_r = 35.89^\circ$, $\beta_r = 38.07^\circ$, $\gamma_r = 19.17^\circ$, $\delta_r = 0.022^\circ$, $\epsilon_r = 5.204^\circ$ and $\zeta_r = 0^\circ$. At these angles, the landscape of the corresponding

modulus square of the structure factor $|F|^2$ within certain (hkl) planes is depicted in Figure 6.14. The cross scan in Figure 6.14 (b) shows the intensity modulation along the (10l) direction. Note that the form factor results in a strong increase at the (103) Bragg reflection in accordance with the experimental data. The molecular arrangement that gives the best agreement with the experimental intensities is shown in Figure 6.15: The PTCDI- C_8 molecules stack in a cofacial packing along the b -axis with a distance between adjacent aromatic planes of 3.58 Å, a typical intermolecular distance of perylene molecules along the π - π stacking direction [144–146]. Consequently, the overlap of the molecular π orbitals, crucial for the charge transport, is expected to be larger along the

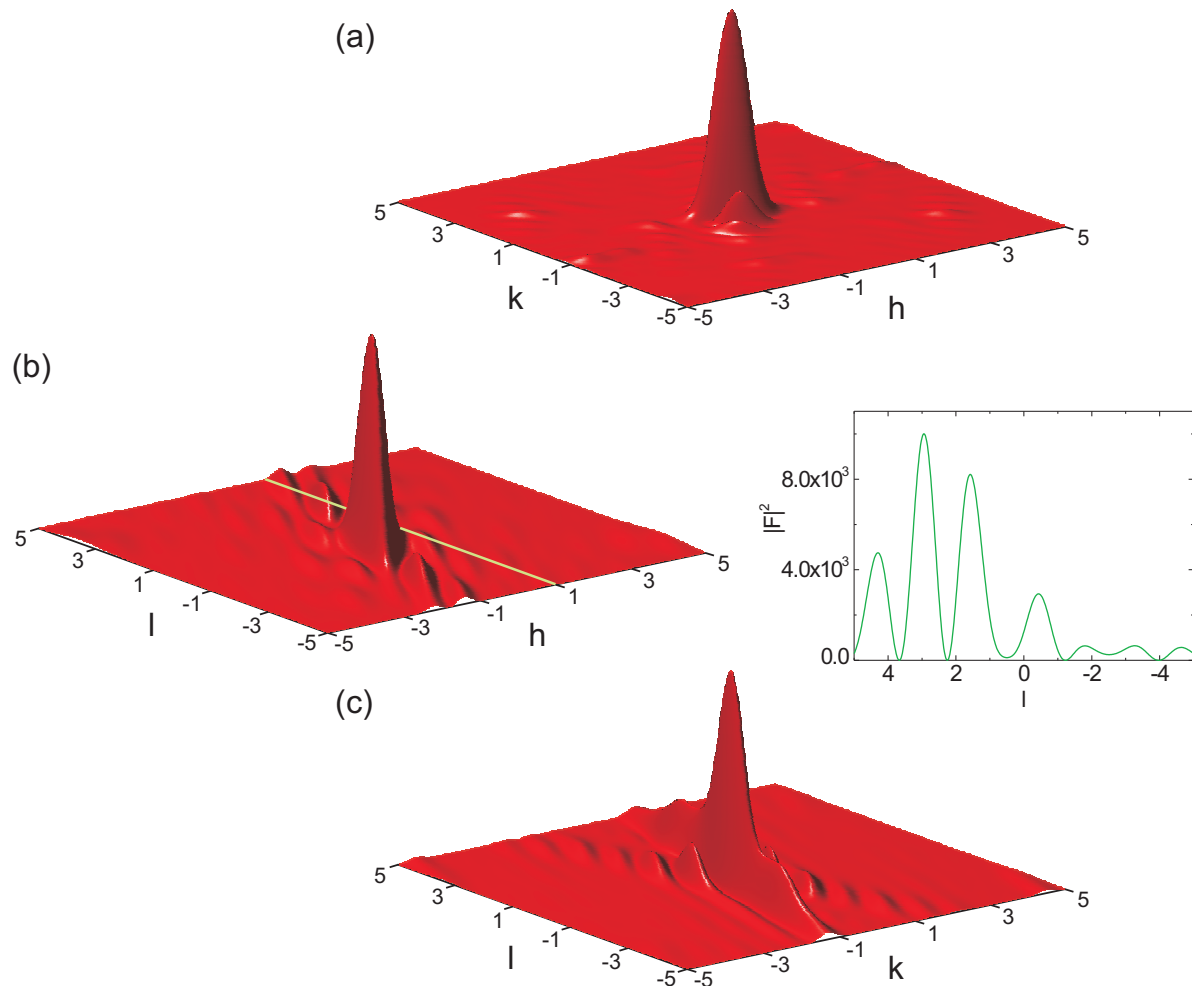


Figure 6.14: 2D representation of the square modulus of the structure factor F in the (a) (hk0) plane, (b) (h0l) plane with a cross scan along the (10l) direction and (c) (0kl) plane.

[010] crystal direction. Thus, the anisotropic growth of PTCDI-C₈ along this direction (assisted by external methods such as the use of templates or anisotropic substrates) could be exploited to induce one dimensional structures with enhanced effective charge carrier mobility. The molecular plane of the aromatic core is tilted by $67 \pm 2^\circ$ with respect to the surface plane. Note that this structure implies a tilt of each alkyl chain of $50 \pm 3^\circ$ with respect to the molecular plane. A similar value is found for the bulk phase. However, the tilt angle of the aromatic core relative to the *a-b* plane, which is more relevant for

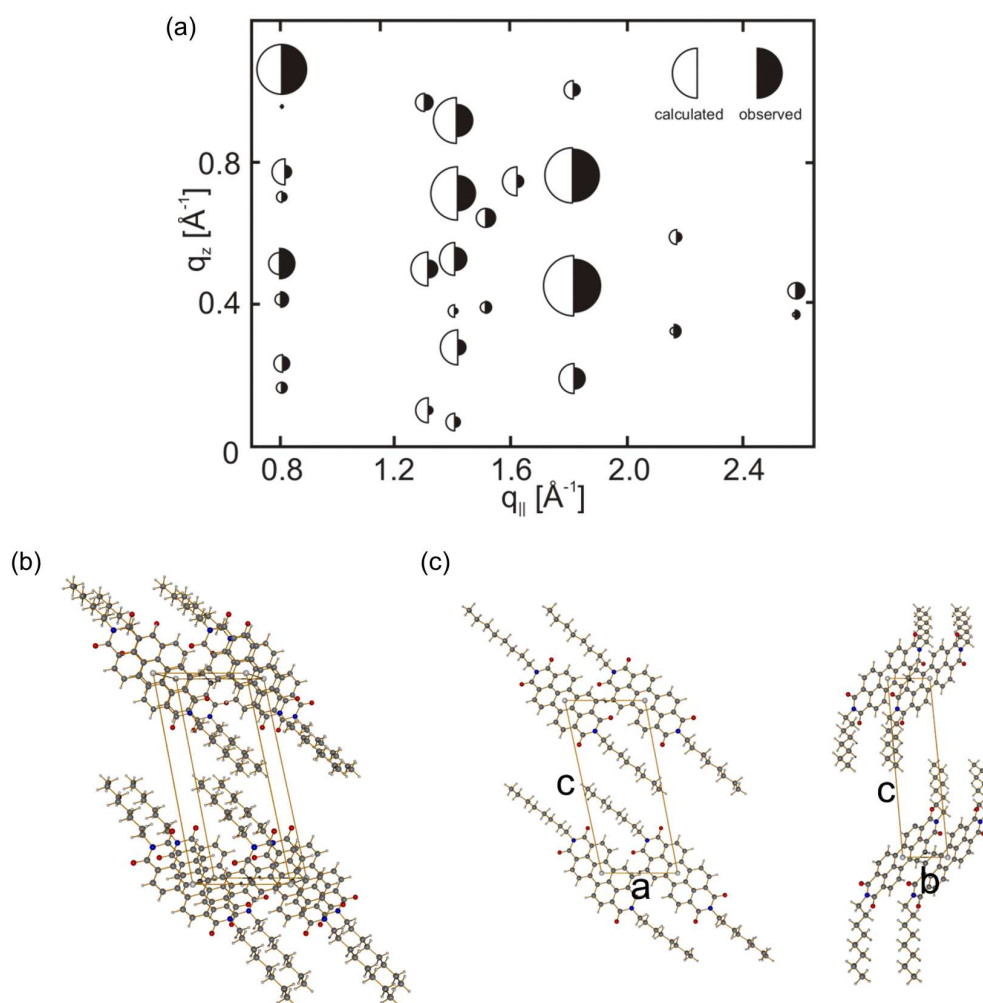


Figure 6.15: (a) Best agreement between the integrated intensity from the scan and the calculated intensity from the structural model. (b) This leads to a structural model where the aromatic PTCDI-C₈ core is tilted with respect to the surface by an angle of 67° . (c) Projections of the *a-c* and *b-c* plane.

intermolecular π - π overlap, differs slightly from that of the bulk phase (69.3° between the aromatic core and surface plane) [20].

In addition, the average size L_z of the crystallites perpendicular to the surface can be assessed from the full width at half maximum (Δq_z) of the Bragg reflections along q_z according to $L_z \approx 2\pi/\Delta q_z$ as mentioned before. The width of Bragg diffraction peaks in in-plane rods along q_z contains information about the size of the crystallites that are coherently ordered, as schematically shown Figure 6.16 (a), in contrast to specular x-ray reflectivity, where the width of the Bragg peaks and Laue oscillations gives only insight in the average height of the whole layered film regardless of the in-plane register among layers. Figure 6.16 (b) shows two representative rod scans along q_z belonging to the $(\bar{1}03)$, (102) and (101) Bragg diffraction peaks, respectively. A vertical coherence length L_z of ~ 180 Å is obtained that coincides with the film thickness implying that 3D crystallites extend across the entire thickness of the layered film.

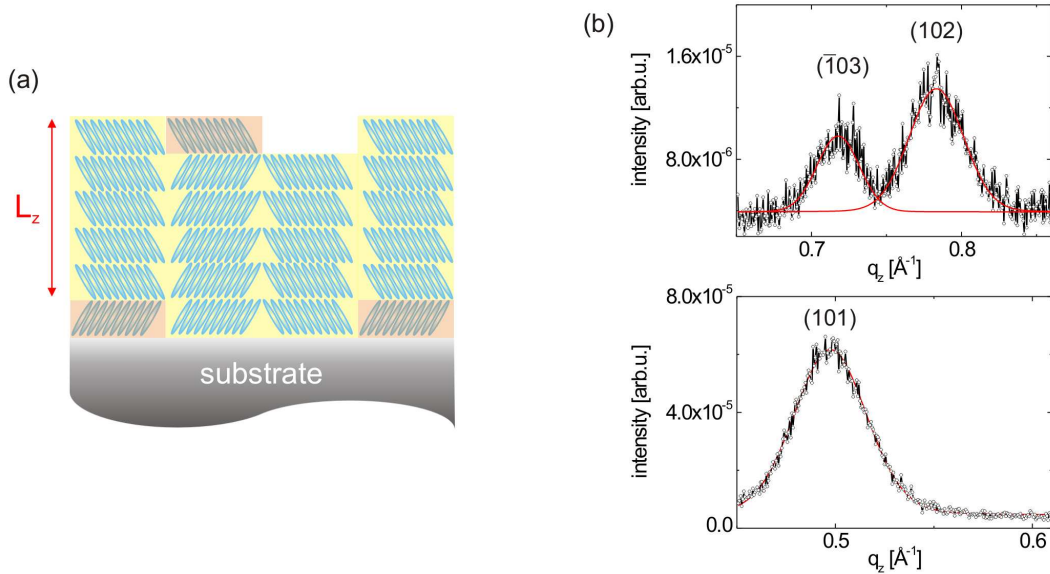


Figure 6.16: (a) Scheme showing the meaning of the coherence length L_z . (b) Two representative rod scans along q_z for the $(\bar{1}03)$, (102) and (101) Bragg diffraction peak. The red curves are the fits performed by applying Pseudo-Voigt functions.

6.2.2 Temperature Related Properties

As in the case of SiO₂, the dependence of different substrate temperatures on the film structure was investigated. Figure 6.17 shows the in-plane structure at room temperature for a film thickness D of ~ 326 Å and at 150 °C for $D \sim 163$ Å, respectively. Interestingly, from the position of the Bragg reflections, it can be seen that the in-plane lattice undergoes an expansion of the basis vector b from $b_{RT} = 4.80$ Å to $b_{150^\circ\text{C}} = 4.89$ Å whereas the a basis vector contracts from $a_{RT} = 9.03$ Å to $a_{150^\circ\text{C}} = 9.00$ Å. A similar behavior can be observed on SiO₂ [147]. The FWHM reveals again an increase in domain sizes with increasing substrate temperature from about ~ 400 Å to ~ 900 Å coinciding as well with the trend obtained from silicon substrates.

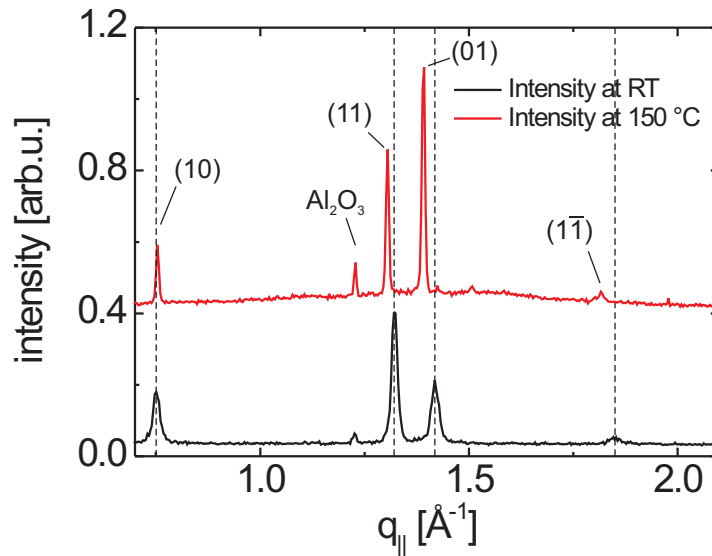


Figure 6.17: GIXD scan on Al₂O₃ (1120) at two different substrate temperatures.

6.3 Conclusions

A comprehensive structural study as a function of growth temperature of PTCDI-C₈ films on native SiO₂ was performed by combination of specular x-ray reflection, GIXD, and AFM. For all growth temperatures, PTCDI-C₈ forms smooth multilayer films in which

the molecules are cofacially oriented in an oblique cell (with one molecule per unit cell) within the layers with the π - π stacking along the b -axis. Accurate information of the vertical structure in the multilayer was provided and the tilt of the perylene cores within the layers was determined. Both, the in-plane unit cell and the tilt angle, evidence a thin-film structure similar to the one investigated on Al_2O_3 (11 $\bar{2}$ 0). It was shown that an adequate growth temperature followed by a mild post-annealing treatment leads to the best ordering in the multilayer structure. Although the increase of the growth temperature promotes an enlargement of the size of the terraces beyond several microns, GIXD reveals a comparable lateral crystalline size of ~ 280 Å. The presented results suggest that an improvement of PTCDI- C_8 OFETs performance with growth temperature is not due to an increase of the lateral size of the crystallites but is associated with a dramatic reduction in the density of grain boundaries and better vertical ordering in the multilayer.

On Al_2O_3 , a possible route to extract the information of the full three dimensional structure and molecular packing of PTCDI- C_8 films was presented. A primitive triclinic unit cell containing one molecule was disclosed which differs distinctively from the bulk structure recently reported [20]. The molecular core exhibits a tilt angle of $\sim 67^\circ$ with respect to the surface plane and has an intermolecular distance to adjacent aromatic PTCDI- C_8 planes of 3.58 Å along the π - π stacking direction which is pointing along the b -axis. This draws the conclusion that the overlap of the molecular π - π orbitals, which is crucial for charge transport, is expected to be larger along the [010] crystal direction. Furthermore, it was proven that the 3D crystallites extend across the entire thickness of the layered film. The determination of the molecular packing and microstructure of this organic thin film is a key input in calculating the associated electronic band structure and in modeling the charge-transport properties in organic thin film transistor devices. This is one of the essential key capabilities for a comprehensive understanding of the structure-property relationships and, ultimately, for control of the macroscopic electrical properties of polycrystalline organic thin films.

7 2D Self-Assembly of Pentacene and $F_{16}CuPc$ on $Cu(100)$ ¹

The nature of self-assembly can be described as the spontaneous association of constituents into regular patterns. This phenomenon is driven in the case of 3D supramolecular organic and biological architectures by non-covalent interactions such as van der Waals interactions, electrostatic interactions and hydrogen bonds. However, it should be taken into account that the concepts of 3D self-assembly cannot be automatically transferred to two dimensions. Here, beside intermolecular interactions, adsorbate-substrate interactions come into the play affecting or even dictating the self-assembly process. In the past decades, several investigations focused on self-assembly of monocomponent supramolecular systems on various substrates have been carried out [148–154]. Recently, a couple of studies on the mixing of small organic molecules with π -conjugated orbitals have appeared as promising route for the creation of 2D structures with tailored electronic and chemical properties [155–164]. Nevertheless, all strategies have the ultimate goal in common to control the self-assembly process from a molecular level up to a microscopic length scale to create bottom-up ensembles as functional surfaces or molecular templates [16, 165–168]. Of particular interest is the design of molecular matrices which can be used to accommodate guest molecules for the fabrication of sensors or further assembly of complex organic architectures [169–173].

This chapter elucidates the self-assembly behavior of pentacene, which is up to now probably the most important p-type semiconductor, and $F_{16}CuPc$, one of the few air stable n-type semiconductors, on a single crystalline $Cu(100)$ substrate. In addition, by the codeposition of both compounds on the $Cu(100)$ substrate, the successful 2D

¹The measurements presented in this chapter were performed at the National Institute for Materials Science (NIMS) in Tsukuba, Japan funded by the Japan Society for the Promotion of Science (JSPS).

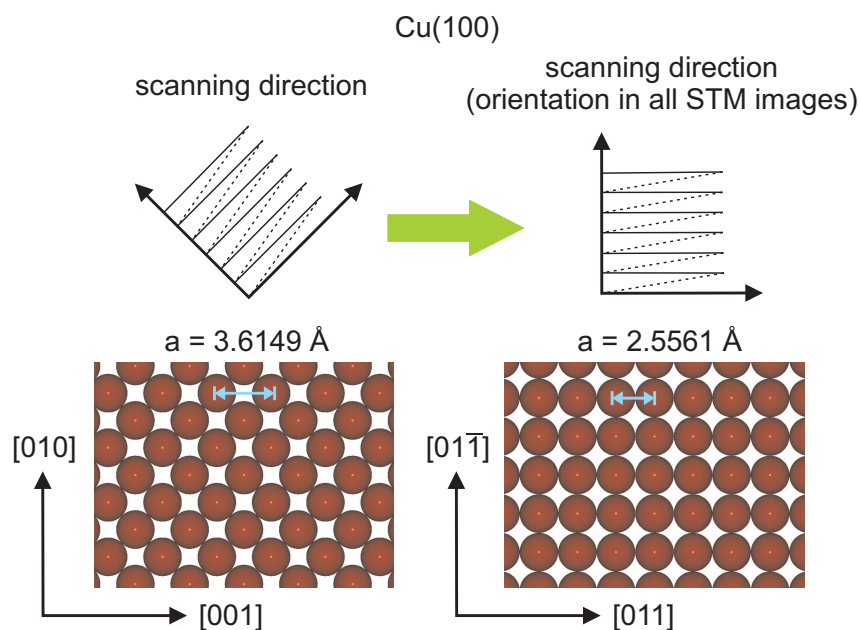


Figure 7.1: Orientation of the Cu(100) substrate for all STM scans performed in this chapter.

supramolecular growth of a binary pentacene- $F_{16}CuPc$ monolayer will be presented whose structural ordering shows the potential to act as a template. Cu has been chosen as a substrate due to its frequent implementation as contact material in organic devices. Cu(100) is one of the rarely investigated surfaces in contrast to frequently reported studies of molecular growth on Cu(111) and Cu(110) [174–178].

Both, pentacene and $F_{16}CuPc$ were evaporated with low rates from Knudsen cells at room temperature until the deposition of one monolayer was completed (between 10 to 15 minutes). The mixed monolayer was obtained by opening and closing the corresponding shutter of each molecule for particular intervals. The STM images were measured at room temperature by a JEOL system in constant current mode with a tunneling current I_T of 0.08 - 0.11 nA and a bias voltage V of 0.005 - 0.9 V.

Cu exhibits a face centered cubic (fcc) crystal structure with a lattice parameter of 3.6149 Å as demonstrated in Figure 7.1. The nearest-neighbor distance is therefore 2.5561 Å. All STM scans were performed at a tilt angle of 45° with respect to the [001] direction with the Cu substrate orientated as shown in Figure 7.1 on the right.

7.1 Self-Assembly of Pentacene

Figure 7.2 (a) shows a representative STM image of the molecular arrangement in the first monolayer of pentacene on Cu(100). Pentacene adsorbs in a lying down orientation with the molecular plane parallel to the substrate, a general feature often seen for the first monolayer of conjugated molecules on metals [174–176, 179–182]. The first monolayer of pentacene shows only short range ordering extended up to 3 to 4 molecules as illustrated in the insets of Figure 7.2 (a). The absence of long-range ordered domains at room temperature evidences a rather strong molecule-substrate interaction. This is consistent with ultra-violet photoemission spectroscopy experiments and density functional calculations performed on Cu(100) which have revealed important hybridization of the molecular π -orbitals of pentacene with copper states [183]. In addition, the strong substrate-molecule interaction also dictates the alignment of pentacene on the surface reflecting the two-fold symmetry of the Cu(100) substrate. The long molecular axis of pentacene orientates along the high symmetry axes of Cu(100), i.e [01-1] or [011] directions. Pentacene is observed

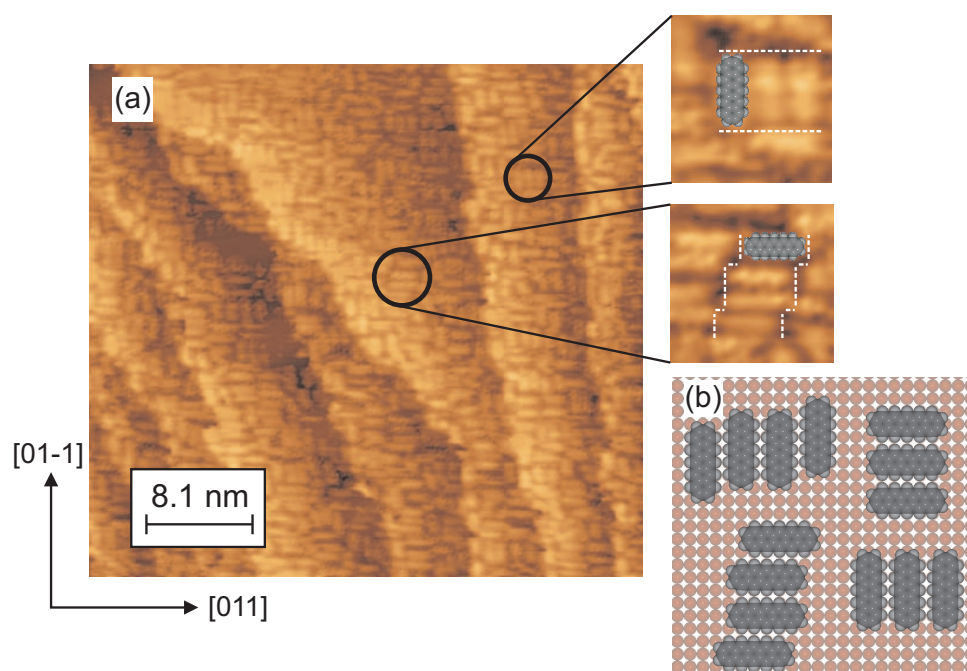


Figure 7.2: (a) STM image of a fully covered monolayer of pentacene on Cu(100) measured at room temperature ($I_T = 0.089$ nA, $V = 5$ mV) with zooms into regions of Figure 7.2 (a). (b) Model of the molecular arrangement. The pentacene molecules have been depicted with the central phenyl ring adsorbed on hollow sites according to reference [183].

to locally pack in two configurations, the so called line or wave topologies as depicted in the zooms of Figure 7.2 (a) and in Figure 7.2 (b). In the line configuration, pentacene molecules are close-packed in rows. In the wave topology, some molecules present a shift of 2.6 \AA along the direction of the long molecular axis. These two configurations have recently been predicted in a theoretical calculation of the equilibrium adsorption geometries of pentacene on $Cu(100)$ [184]. The distance between adjacent pentacene molecules measured from STM images is $7.6 \pm 1 \text{ \AA}$, which is in agreement with the expected separation of pentacene in a side-by-side close packing ($\sim 7.7 \text{ \AA}$). In addition, adjacent molecules separated by $\sim 10.2 \text{ \AA}$ and cross-like structures are visible but they represent rather the exception.

A look to the first stages of growth reveals that pentacene molecules align first along the step edges before adsorbing on the flat terraces (see Figure 7.3).

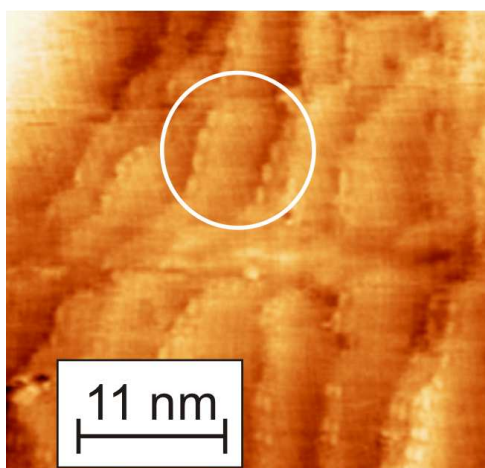


Figure 7.3: STM image of the early stage growth of pentacene ($I_T = 0.09 \text{ nA}$, $V = 4.4 \text{ mV}$). It can be seen that the molecules tend to adsorb along the step edges and not on the flat terraces.

7.2 Self-Assembly of $F_{16}CuPc$

On the contrary to the short range order of pentacene, $F_{16}CuPc$ tends to form highly ordered domains extended over several tens of nanometers, as can be seen in Figure 7.4 (a). The molecules lie flat on the substrate as previously observed on other sur-

faces [157, 178, 186] and pack according to a quadratic unit cell. The average distance between molecules measured from various STM images is $14.8 \pm 1 \text{ \AA}$. For $F_{16}CuPc$, the surface also acts as template dictating the azimuthal orientation of the domains. Two enantiomorphous chiral domains can be identified related to mirror symmetry along the [01-1] and [011] directions. The observed structure is consistent with a dense packing of the molecules in a commensurate cell with a lattice parameter of $\sim 14.9 \text{ \AA}$. Only one epitaxial relationship connecting the Cu(100) substrate with the $F_{16}CuPc$ compounds is able to describe the experimentally observed structure and is expressed, for each mirror domain, by the following matrices

$$M_1 = \begin{bmatrix} 5 & 3 \\ -3 & 5 \end{bmatrix}, \quad M_2 = \begin{bmatrix} 3 & 5 \\ -5 & 3 \end{bmatrix} \quad (7.1)$$

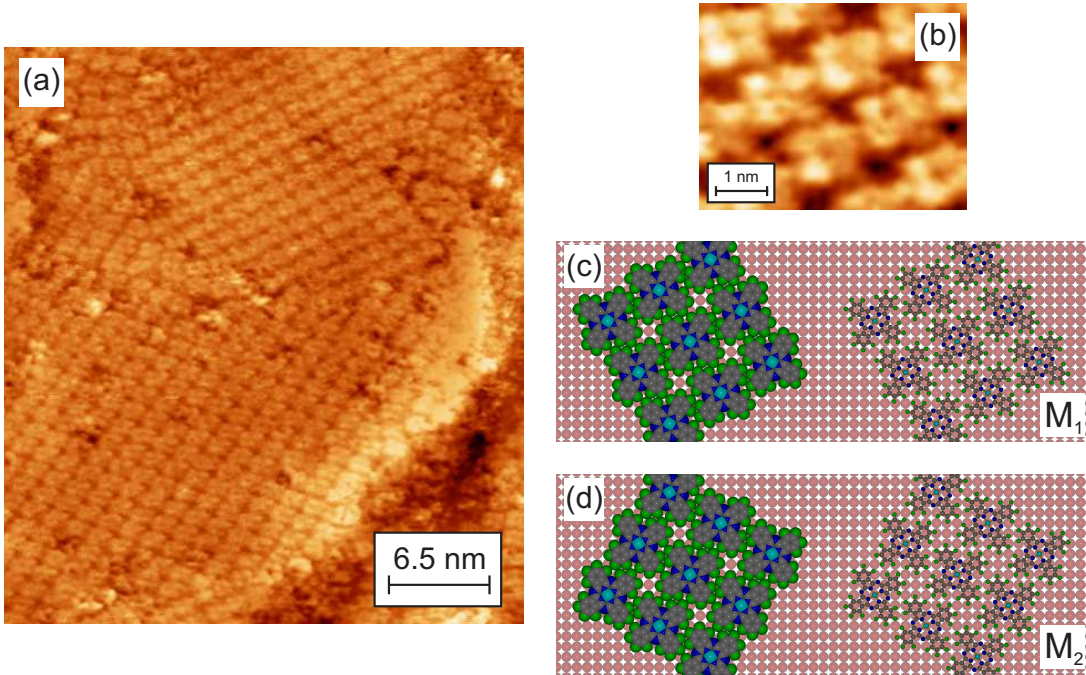


Figure 7.4: (a) STM image of a fully covered monolayer of $F_{16}CuPc$ on Cu(100) measured at room temperature. (b) High resolution image showing a slight tilt of each molecule with respect to the [01-1] direction ($I_T = 0.087 \text{ nA}$, $V = 0.875 \text{ V}$ for both images). (c) and (d) Model of the molecular arrangement in both domains with the epitaxial relationship according to M_1 and M_2 respectively, including and excluding the van der Waals radius for each atom.

which relates the basis vectors of the substrate s_1, s_2 along the high symmetry axes with the ones of the $F_{16}CuPc$ molecule m_1, m_2 via $m = M_i \cdot s$. With this unit cell at hand, each molecule has to be tilted by $13.5 \pm 1^\circ$ to avoid steric repulsion as shown in Figure 7.4 (b). The schemes in Figure 7.4 (c) and (d) depict the proposed model with and without the van der Waals radii and illustrate demonstratively that the molecules are ordered in a pinion fashion to allow a packing as dense as possible with the distance between closest F atoms at $\sim 2.7 \text{ \AA}$. The assembly in a commensurate structure suggests a strong interaction of $F_{16}CuPc$ with the $Cu(100)$ surface. Although there are so far no studies about the electronic coupling of $F_{16}CuPc$ on $Cu(100)$, this hypothesis is supported by a recent work of $F_{16}CuPc$ on $Cu(110)$ reporting a strong hybridization of the molecular orbital of $F_{16}CuPc$ with $Cu(110)$ [185].

Similarly to the early growth stages of pentacene, $F_{16}CuPc$ adsorbs first along the step edges of the Cu crystal (see Figure 7.5). However, the molecules seem not to lie flat on the terraces but growing in a standing up configuration forming a row of molecules parallel to the step edges.

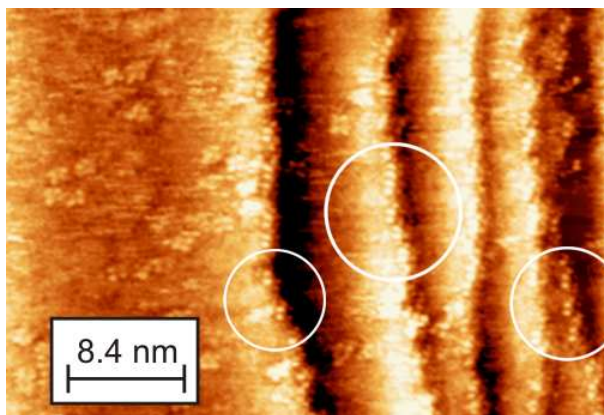


Figure 7.5: STM image of the early stage growth of $F_{16}CuPc$ ($I_T = 0.087 \text{ nA}$, $V = 0.833 \text{ V}$). It can be seen that the molecules seem not to lie flat on the terraces but growing in a standing up configuration forming a single row of molecules parallel to the step edge.

7.3 Self-Assembly of Pentacene and $F_{16}CuPc$ in a Mixing Ratio 2:1

Coevaporation of pentacene and $F_{16}CuPc$ in a ratio of 2:1 leads to highly ordered binary 2D structures, as can be seen in Figure 7.6 (a). Occasionally, crystalline domains are separated by a disordered region of mobile molecules in a 2D gas-like phase, as shown in Figure 7.6 (a), which can be attributed to a local coverage of below one monolayer. However, no evidence was found for crystalline phases of varying density as frequently

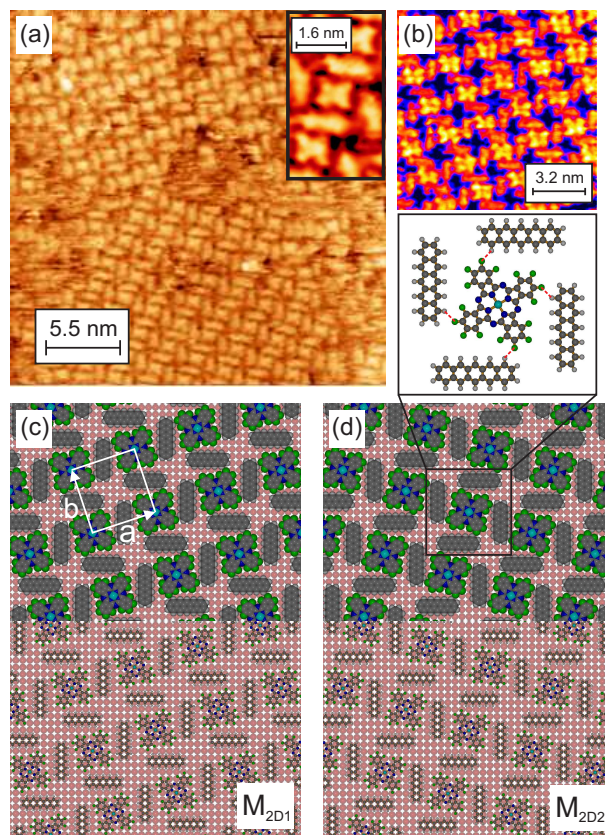


Figure 7.6: (a) STM image revealing highly ordered 2D binary structures with two mirror domains. The inset shows a high resolution STM image disclosing again a slight tilt of the $F_{16}CuPc$ molecule (b) Vacancies of $\sim 8 \text{ \AA}$ are visible (dark color) making this supramolecular arrangement a potential candidate for a template (all images measured at $I_T = 0.087 \text{ nA}$ and $V = 0.875 \text{ V}$). (c) and (d) Model of the 2D binary structure with showing the epitaxial relationship expressed by M_{2D1} and M_{2D2} with and without the corresponding van der Waals radii. The inset in Figure 7.6 (d) accentuates the potential C-F \cdots H bondings of the proposed arrangement.

observed for other molecular systems [187]. Previous studies on the self-assembly of DIP and F₁₆CuPc showed that the growth of the 2D close-packed mixed phase takes place via island condensation from a 2D lattice gas of mixed molecules [157]. The unit cell determined from STM images is square with a basis vector of $23.5 \pm 1 \text{ \AA}$ and is consistent with an epitaxial relationship with the substrate given by

$$M_{2D1} = \begin{bmatrix} 9 & 3 \\ -3 & 9 \end{bmatrix}, \quad M_{2D2} = \begin{bmatrix} 3 & 9 \\ -9 & 3 \end{bmatrix} \quad (7.2)$$

representing the two observed mirror domains with a basis vector of 24.3 \AA . As for F₁₆CuPc, two enantiomorphic chiral domains are formed in which pentacene orientates along the high symmetry directions of Cu(100) as in the pure layers, reflecting the still strong molecular interaction with the Cu substrate. STM images suggest that the F₁₆CuPc molecules are rotated in the same way as in the pure films, although this cannot be proven conclusively (see Figure 7.6 (a) and inset). Note that the closest distance between fluorine atoms of F₁₆CuPc and hydrogen atoms of pentacene is $\sim 2.40 \text{ \AA}$, making the C-F \cdots H bonds a plausible driving force for the mixed assembling (Figure 7.6 (c) and (d) with inset) as recently observed for mixtures of F₁₆CuPc and DIP molecules [157, 188, 189]. On the other hand, the interaction with the Cu(100) substrate here dictates the molecular orientation and imposes commensurability. As a result of the interplay between both, intermolecular and molecule-substrate interaction, the packing is not as close and vacancies in the range of $\sim 8 \text{ \AA}$ can be observed as shown in Figure 7.6 (c) and (d). A zoomed area of the STM image in Figure 7.6 (a) is depicted in 7.6 (b) with a different color code to allow a better observation of the porosity in the mixed F₁₆CuPc:pentacene structure

In contrast to the short-range order in the pure pentacene monolayer, the mixed assembly of pentacene and F₁₆CuPc results in long-range ordered domains. It is proposed that this is due to a weakening of the pentacene-Cu electronic coupling as a consequence of the enhanced intermolecular interactions by the formation of C-F \cdots H bonds. This effect has also been demonstrated for the assembly of F₁₆CuPc and DIP on Au(111), a system in which reduced charge transfer between F₁₆CuPc and Au occurs for the mixed layer [190]. In addition, a recent photoemission study performed for two adlayers of pentacene with different density on Cu(110) disclosed a stronger modification of the surface state of Cu(110) upon the adsorption of the densest pentacene structure [191]. In this case, the increase in binding energy is attributed to a combination of interactions including charge

transfer and hybridization of electronic states. Taking this observation into account, it is reasonable to expect that the coevaporation of pentacene and $F_{16}\text{CuPc}$ for other ratios with a lower amount of pentacene will still result in long-range ordered binary systems. The strong influence of intermolecular interactions affecting geometry, molecular conformation and electronic structure has been also demonstrated for PTCDA chemisorbed on $\text{Ag}(111)$ [192]. All above-mentioned aspects revealed by these recent studies show that profound theoretical models as well as further experimental investigations are necessary for a more fundamental understanding of 2D supramolecular self-assembling. For this purpose, comparing the self-assembly of single component and binary layers offers an excellent system to shed light on the intricate correlations between intermolecular and molecule-substrate interactions.

7.4 Conclusions

To conclude, the coevaporation of pentacene and $F_{16}\text{CuPc}$ on $\text{Cu}(100)$ results in a 2D binary network of a crystalline nanoporous structure with vacancies of about 8 Å in diameter. The supramolecular self-assembly of 2D binary structures demonstrated here opens the avenue, not only to the formation of multicomponent 2D patterns in a controlled manner, but also to nanoporous templates with potential for the complexation of other molecular species and further construction of 3D architectures. It is shown that $\text{C-F}\cdots\text{H}$ intermolecular interactions between both compounds promote the mixed self-assembly whereas the molecule-substrate interaction imposes the molecular orientation. The long-range ordering of the $F_{16}\text{CuPc}$ -pentacene binary structure versus the short-range order of pure pentacene layers evidently illustrates how the interplay between intermolecular and molecule-substrate interactions can tune and dictate the self-assembly properties of supramolecular structures.

8 1D Self-Assembly of Phthalocyanine Derivatives

As mentioned already, small conjugated organic molecules have become extremely attractive options for applications such as OFETs, OLEDs and OPVs. So far, enormous progress has been made in optimizing the structural properties of organic thin films to obtain improved device performance. However, one prerequisite for the design of nanoscale devices with novel functions is the bottom-up growth of one-dimensional (1D) structures as successfully demonstrated already for inorganic semiconductors. [193,194]. 1D organic nanostructures, such as nanowires, nanotubes, nanoribbons and nanofibers are expected to constitute a new class of multifunctional materials for a vast field of electronic applications including chemical sensors, phototransistors, solar cells, nanoscale lasers or miniaturized devices. Just recently, several groups have reported a significant improvement of the field-effect mobility in organic nanowire transistors that is attributed to the absence of crystalline boundaries and molecular disorder [20,195–197]. Recent studies have also proven that nanocrystalline donor/acceptor networks based on vertical 1D single-crystalline organic structures are very promising architectures for high efficient solar energy conversion since they fulfill the conditions necessary for both, an efficient exciton dissociation and an efficient charge carrier collection [8,27].

In spite of the increasing number of reports on 1D organic systems [20,195–201], the controlled growth of organic semiconducting nanostructures still remains an experimental challenge. The growth of 1D architectures with single crystalline structures, tunable dimensions and spatial control are severe key barriers which must be overcome to meet the requirements of future nanotechnology.

In a previous work, it was demonstrated that, in the case of $F_{16}CuPc$ compounds,

vertical growth of uniform organic 1D nanostructures deposited from vapor phase can be directed by templates of gold (Au) nanoparticles on silicon dioxide substrates [18]. This strategy enables precise localization and packing density of the 1D structures and promises an easy route for the controlled bottom-up fabrication of 1D organic architectures. This chapter tries to pursue the investigation in order to assess the suitability of this strategy to other organic molecules and to elucidate the role of the Au templates. The study has now been extended to other planar phthalocyanine derivatives, namely $H_{16}CuPc$, $F_{16}CoPc$ and $H_{16}CoPc$, which exhibit crucial different electronic properties [202]. Additionally, we have chosen two other molecules with strong crystalline anisotropy, para-sexiphenyl (p-6P) and PTCDI- C_8 which was characterized in chapter 6. Both compounds were reported to form needle-like structures under appropriate conditions [20, 203]. It is shown that a selective and precise 1D growth mode is in general possible for the aforementioned phthalocyanine derivatives. Scanning electron microscopy (SEM) and transmission electron microscopy (TEM) measurements have been performed to give a detailed insight into the structural properties of the 1D structures. Furthermore, the impact of different morphologies of Au templates has been investigated as well as the influence of the substrate temperature on the 1D nanostructures.

8.1 1D Self-Assembly of Phthalocyanine Derivatives on Gold Nanoparticles

8.1.1 Growth Mode and Structure

Since SiO_2 is a flat and rather inert surface, organic molecules generally form a multilayer system with nearly vertical orientation. Previous studies of $F_{16}CuPc$ illustrated that this growth mode is profoundly affected by the presence of Au nanoparticles which act as nucleation sites, collecting diffusing molecules on the surface and promoting their 1D growth mode. Silicon wafers with a native oxide layer were coated by micellar lithography with pseudo-hexagonal arrays of highly homogeneous Au nanoparticles whose diameter d_{part} and interparticle distance l are adjustable as shown in Figure 8.1. Figure 8.1 (c) and (d) are the corresponding micrographs of the schemes depicted in 8.1 (a) and (b) recorded by SEM in the back-scattered electron imaging mode. It can be seen that no 1D growth takes place in regions where the surface is not covered by Au nanoparticles. The sub-

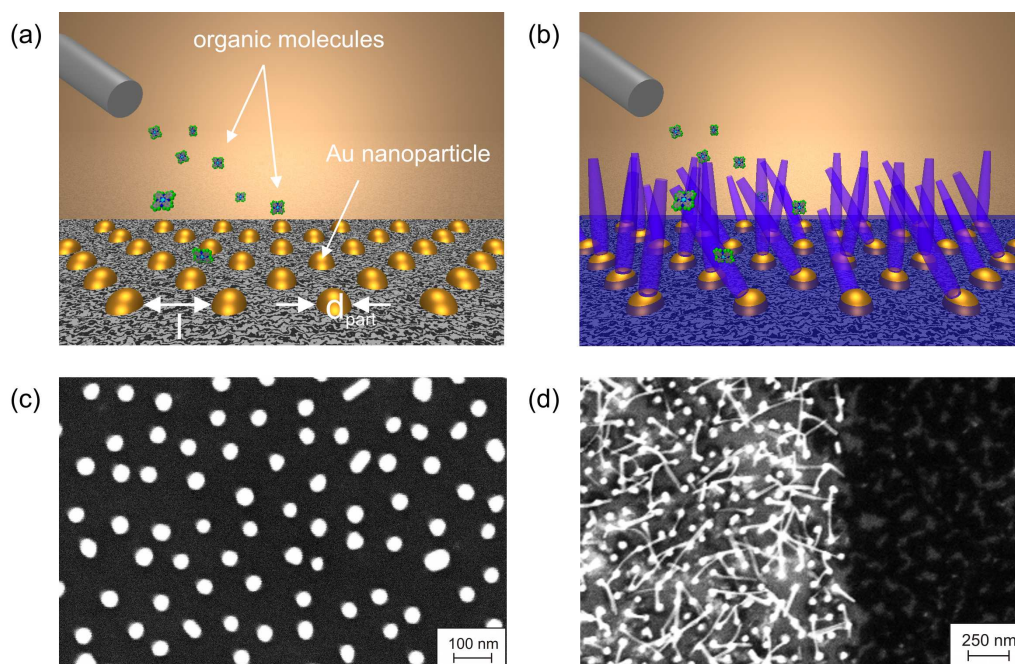


Figure 8.1: (a) Scheme of the deposition process of the organic compound on a decorated sample surface with Au nanoparticles whose interparticle distance l and nanoparticle diameter D is controllable. (b) The Au nanoparticles act as nucleation sites and trigger a 1D growth mode. (c) and (d) Corresponding SEM images collected in the back-scattered electron imaging mode. No 1D growth takes place in regions where the surface is not covered by Au nanoparticles.

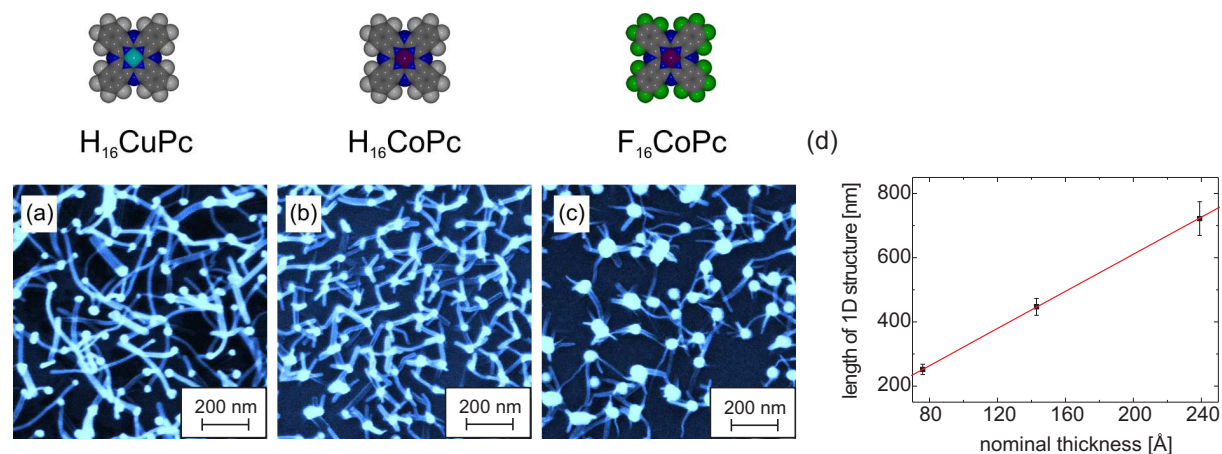


Figure 8.2: (a) - (c) SE micrographs showing the growth modes of different phthalocyanine compounds. It can be seen that 1D structures exhibit widths ranging between 15 to 35 nm. (d) The length of the 1D structures as a function of the nominal thickness is shown. A linear dependence can be observed.

strate temperature is a critical parameter and should be chosen in such a way, that it is sufficiently high for enhancing an 1D growth mode but being below the temperature at which competing desorption processes occur. To explore whether this strategy works successfully for other small weight aromatic molecules, the growth of $H_{16}CuPc$, $F_{16}CoPc$ and $H_{16}CoPc$ on Au nanoparticle templates has been investigated for different temperatures ranging from room temperature to 140 °C. Figure 8.2 (a) - (c) shows representative SEM images illustrating the resulting morphology of the different organic materials onto the arrays of Au nanoparticles. All phthalocyanine derivatives considered here show a selective 1D growth on top of the Au nanoparticles which is favored at substrate temperatures of ~ 120 °C. Whereas the length of these 1D structures can be tuned by the amount of deposited material, as demonstrated by Figure 8.2 (d), their widths seem to be an intrinsic parameter of the specific molecule. A linear dependence of the length of the 1D structures on the nominal thickness is observed for $H_{16}CuPc$ as analyzed from several SEM images. In general, it is for all the phthalocyanine compounds visible that their widths comprise dimensions between 10 and 35 nm regardless of the Au particle size. However, as we will show later, the 1D growth is not completely insensitive to the Au particle size. The role of the overall morphology regarding the Au template will be discussed in detail later.

The generality of the 1D growth for different phthalocyanines and the extremely high uniformity of the organic nanostructures suggest that the template-induced 1D growth is an intrinsic self-assembly property rather than a purely kinetically determined growth

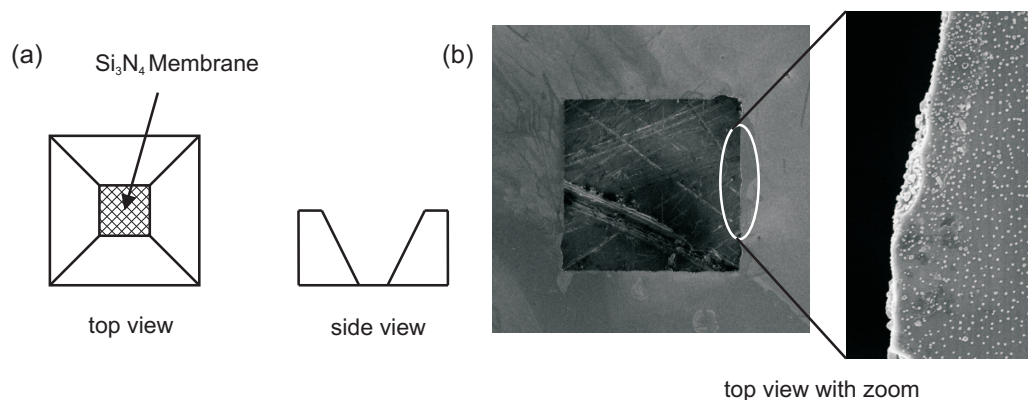


Figure 8.3: (a) Schematic top and side view of the Si_3N_4 membrane. (b) SEM image with a zoom into the region at the edge. It can be clearly seen that arrays of the Au nanoparticles are present at the surface (bright spots) and that the membrane itself is removed (dark area).

mode.

In order to get a deeper insight into the structural properties of the phthalocyanine nanostructures, high resolution TEM was performed. If not otherwise stated, all samples investigated have been grown at a substrate temperature of 120 °C. The process of transferring the 1D nanostructures from the substrate to a copper grid covered with an amorphous carbon film for TEM inspection is rather inefficient and eventually leads to damage the 1D structures. As an alternative approach to analyze the as-grown structures, we have employed Au nanoparticle templates deposited on thin Si_3N_4 membranes suitable for TEM examination. During the coating process with Au nanoparticles the membrane was partly perforated. However, this turned out to be very advantageous since it was now possible to measure the 1D structures growing at the edges. Figure 8.3 shows a schematic top and side view and in addition, a top view recorded by SEM of a typical Si_3N_4 TEM sample before any deposition of the organic compounds took place. A zoom into the region of the membrane edge reveals demonstratively that sufficient gold nanoparticles still cover the surface.

Typical TEM images after evaporation of the specific organic compound are shown in Figure 8.4 for H_{16}CuPc , H_{16}CoPc , F_{16}CoPc and F_{16}CuPc . The inspection by TEM of the 1D architectures grown on the Si_3N_4 samples reveals similar nanowire-like structures

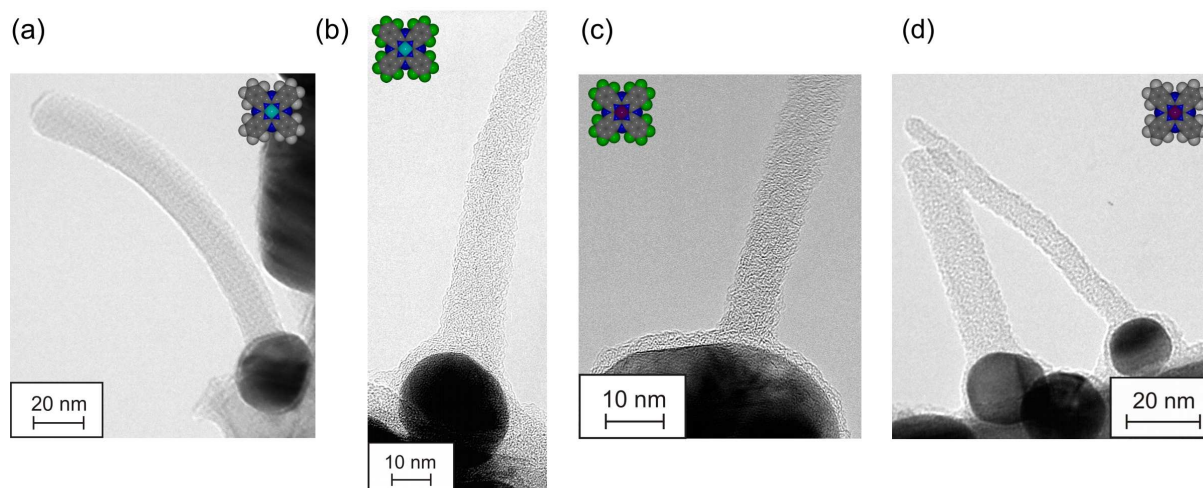


Figure 8.4: (a) - (d) Typical TEM images of four different phthalocyanine derivatives (H_{16}CuPc , F_{16}CuPc , F_{16}CoPc and H_{16}CoPc) on Si_3N_4 membranes. Note that Figure (b), (c) and (d) reveal an organic wetting layer of a thickness between 2 to 3.5 nm which grows around the Au nanoparticles.

in a standing-up configuration. In general, both roughly spherical Au nanoparticles and well faceted particles with hexagonal shapes are present. However, the analysis of 1D structures grown on different particles do not show any clear trend or correlation with the particle shape. An interesting feature manifested by high-resolution TEM is the formation of an organic wetting layer of a thickness between 2 to 3.5 nm around the Au nanoparticles. This layer is visible for instance in Figure 8.4 (b), (c) and (d) surrounding the Au particles. Yet, it cannot be unambiguously determined whether the growth of the 1D architectures occurs on top of the organic wetting layer or on the bare Au since the 2D TEM projection does not enable a reliable identification of the exact location from where the 1D growth starts.

High-resolution TEM discloses that the organic 1D architectures are monocrystalline. Figure 8.5 (a) shows a high resolution TEM image of a H_{16}CuPc 1D structure. A period-

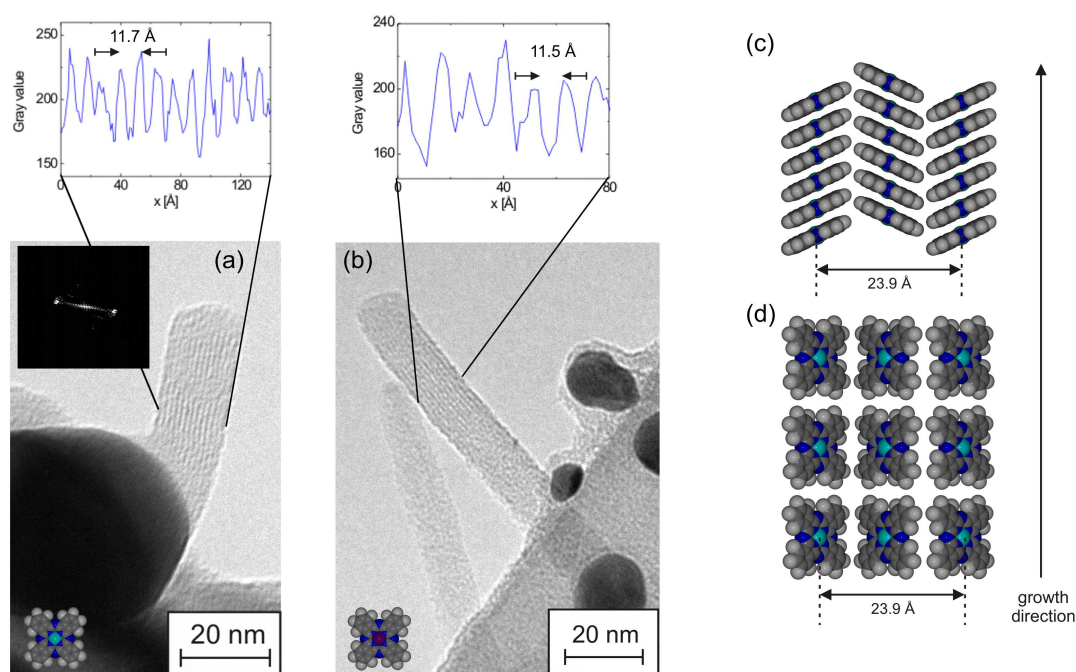


Figure 8.5: (a) High resolution TEM image disclosing a periodicity between adjacent H_{16}CuPc molecules of $\sim 11.7 \text{ \AA}$ determined from both, the profile and the Fourier transform (inset) of the 1D structure. (b) In the case of H_{16}CoPc , an intermolecular distance of $\sim 11.5 \text{ \AA}$ is observed. Figure (b) and (c) present schemes which illustrate two possible structural arrangements of H_{16}CuPc with the π - π stacking parallel to the growth direction or with an assembly of standing up molecules.

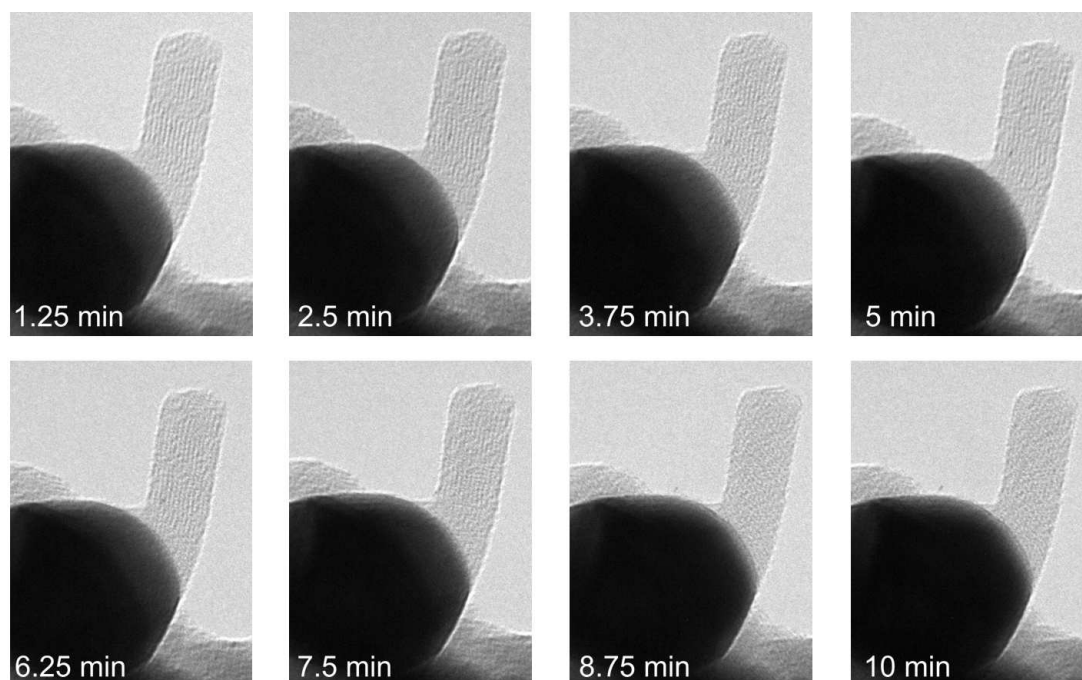


Figure 8.6: Structural features of the H_{16}CuPc nanowire vanish within 10 minutes as a consequence of the interaction between the electron beam and the organic material.

icity of adjacent molecules of $\sim 11.7 \text{ \AA}$ is clearly visible from both, the TEM image and its Fourier transform which can be seen in the inset of Figure 8.5 (a). For H_{16}CoPc , a periodic structure corresponding to a spacing of $\sim 11.5 \text{ \AA}$ was determined as displayed in 8.5 (b). Special care was taking in recording the measurements during the first minute of electron exposure since the structural features completely vanish in a time scale of ~ 10 minutes due to electron beam damage as illustrated in the sequence of TEM images in Figure 8.6. In addition, the TEM was operated at high voltages of only 120 kV which guaranteed on the one hand that the beam damage of the organic material was kept as low as possible but on the other hand to still resolve the molecular lattice parameters. The observed spacing evidences a columnar stack of molecules parallel to the growth direction. Because no other periodicity could be revealed, two potential packing geometries are in accordance with this data, with the π - π stacking direction parallel to the axial direction, as illustrated in Figure 8.5 (c), or parallel to the radial direction, as depicted in Figure 8.5 (d). Both configurations require a molecular tilt, a common growth scenario frequently observed for phthalocyanines [55, 56, 79]. In particular, the measured dimension is in perfect agreement with the distance between molecular columns of the α -form of H_{16}CuPc , where a

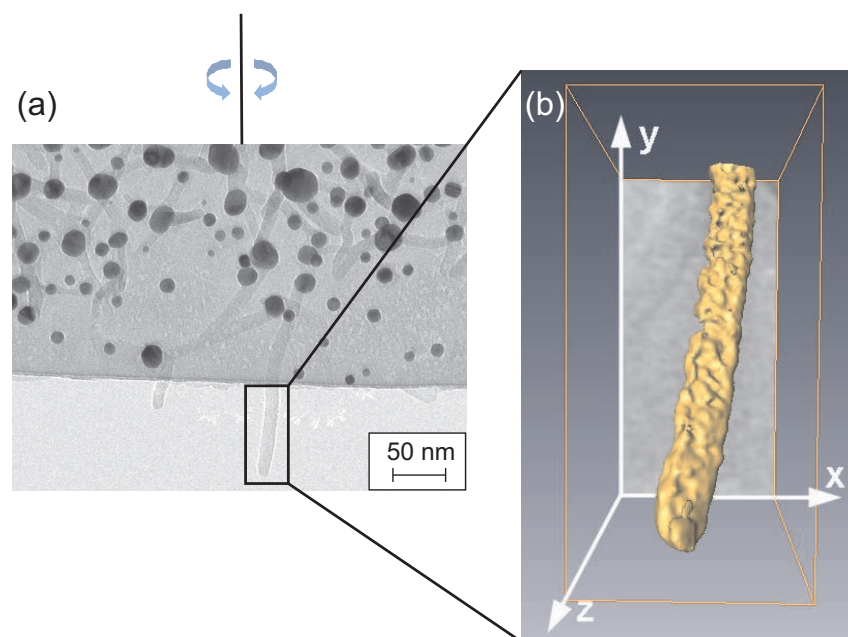


Figure 8.7: (a) Electron tomography can be used to build up a 3D representation of the 1D structure by rotating the sample around the indicated axis. (b) The shape of the grown 1D $F_{16}CuPc$ structure is in this case wire-like and not belt-like.

lattice parameter of 23.9 \AA is reported for two molecules per unit cell [57], with alternating molecular tilts as shown in Figure 8.5 (c) and (d). Because π - π stacking is a strong driving force for the 1D assembling of phthalocyanines, the configuration with the π - π stacking parallel to the axial direction seems to be the most reasonable and in agreement with previous structural reports on the growth of CuPc nanoribbons [196,200]. This configuration would also satisfy the expectations of the strong interaction between molecule and Au substrate. On the other hand, the mitigation of the molecule-gold interaction by an organic wetting layer would favor the assembly of standing up molecules, as shown in Figure 8.5 (d), similar to the packing for $F_{16}CuPc$ nanotubes recently reported [204].

By means of electron tomography, a 3D reconstruction of the 1D objects can be accomplished to elucidate the shape of the 1D structures¹. This is done by rotating the sample around the axis indicated in Figure 8.7 (a) and by evaluating the contrast differences in the different rotational positions. From the reconstructed 3D image shown in Figure 8.7 (b), it can be seen that the shape of the 1D $F_{16}CuPc$ structure is wire-like and not

¹Measurements performed by Dr. Yun-Jin Phillipp from the StEM department at the Max-Planck-Institute for Metals Research in the frame of a collaboration.

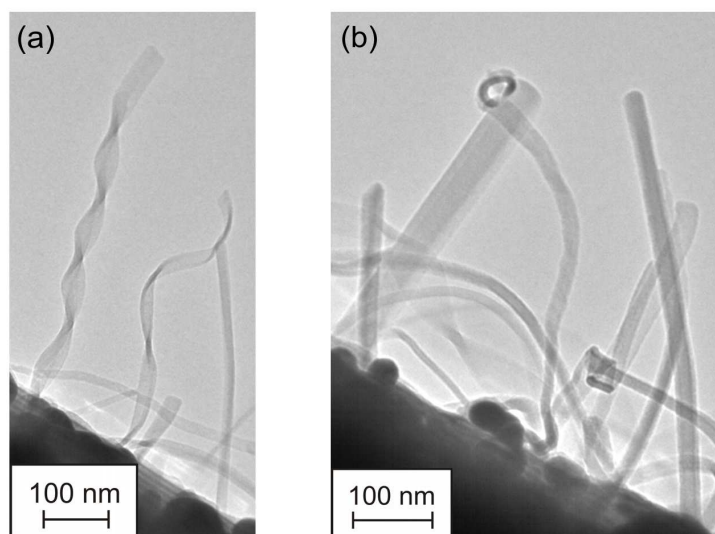


Figure 8.8: (a) and (b) TEM images of $F_{16}CoPc$. Several morphologies coexist and beside nanowires, nanobelts and nanoribbons can be identified.

belt-like. The elongation along the z -axis arises because it is not possible to fully rotate the Si_3N_4 sample 180° (the bright field image series stretches across $\pm 58^\circ$ in steps of 2°) and the missing part is calculated and modeled by a corresponding computer program. For $H_{16}CoPc$, as illustrated in the TEM images in Figure 8.8 (a) and (b), additional 1D structures as for instance nanobelts and nanoribbons are present and even coexist with the wire-like morphologies. The origin of such a diversity can be attributed to the substrate temperature which has a strong influence on the different phase evolution of the respective phthalocyanine compound [200, 201].

8.1.2 Influence of Particle Size and Shape

A more statistical approach was performed to shed light on the role of the particle size. Although the width of 1D structures is not strictly determined by the particle size, a detailed analysis by TEM discloses that the Au particle size does play a role in the growth process. A detailed analysis for $F_{16}CuPc$ has been accomplished. Figure 8.9 (a) - (d) shows representative TEM images of $F_{16}CuPc$ deposited on Au particles of different diameters. By evaluating the width of the 1D structures grown on Au particles with varying size in more than 90 examples, three distinct regions can be distinguished in the corresponding plot of Figure 8.9 (e). A region with Au particle sizes stretching from 0

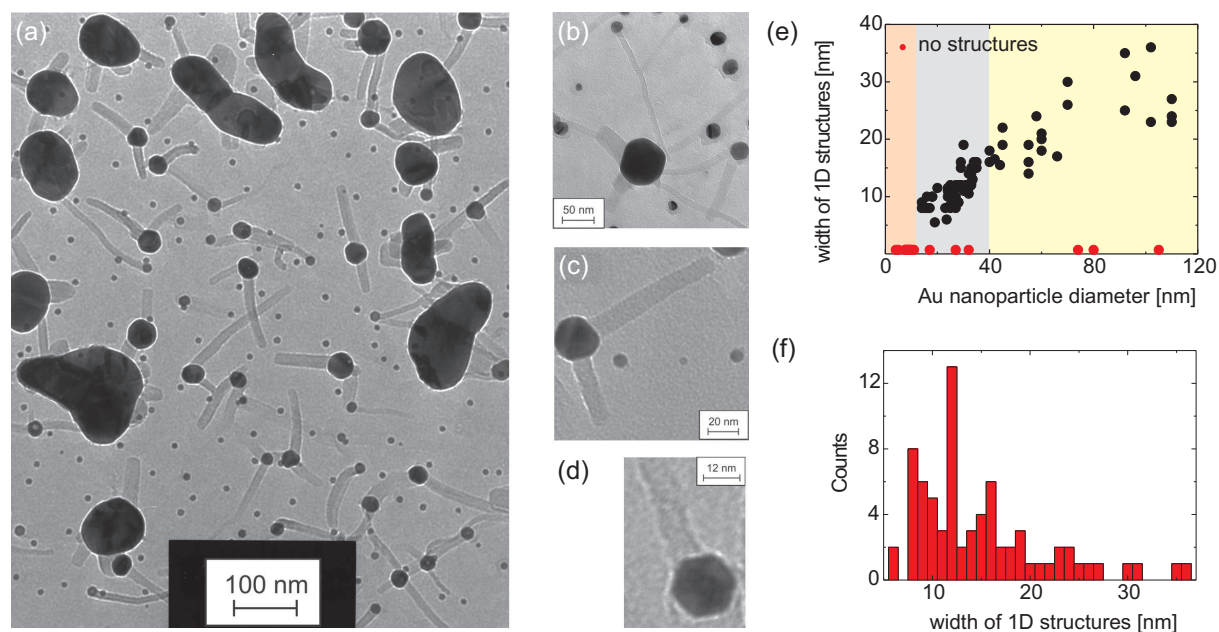


Figure 8.9: (a) - (d) Representative TEM images of F₁₆CuPc deposited on Au particles of different diameters. (e) The widths of the 1D structures of F₁₆CuPc as a function of Au particle diameter. (f) Histogram showing the distribution of the corresponding widths.

nm to ~ 14 nm can be identified where no 1D structures are evolving. For Au particles with diameters between ~ 14 nm and ~ 40 nm, 1D structures with rather uniform widths are observed increasing from 6 to 19 nm with particle size. For particles with diameters above 40 nm, the values of the widths spread much more and the growth of two or more 1D structures takes place as recorded for instance in Figure 8.9 (c). In general, multiple (and thicker) 1D architectures grow from the same particle having in general a shorter length as expected from mass conservation arguments. The histogram in Figure 8.9 (f) illustrates the distribution of the widths. It can be seen that most counts gather around values between 8 and 20 nm with a peak at 12 nm emphasizing again the quite uniform widths of the 1D structures.

The investigation of the effect of the particle shape and in particular the influence of the facets and facet boundaries are of interest since these parameters provide information about the initial growth process. Up to now, it is not known at which exact site of the Au particle the growth begins. High resolution TEM images as presented in Figure 8.10 (a) and (b) cannot answer this question. Although it is possible to resolve some of the facets of the respective Au particles in these TEM micrographs, it is still not

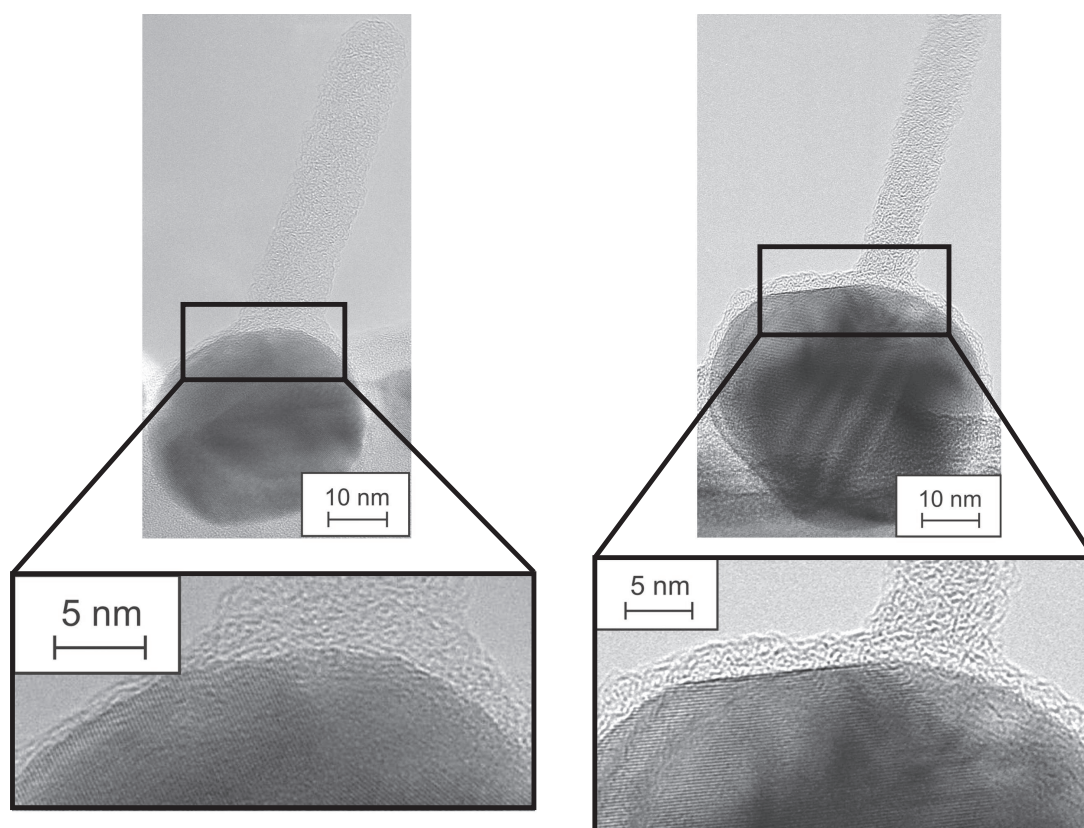


Figure 8.10: (a) and (b) Representative high resolution TEM micrographs showing 1D structures of $F_{16}CuPc$ and $F_{16}CoPc$. Some of the Au facets are visible (as shown in the respective zooms) but these images are not sufficient enough to answer the question whether the organic compounds initially assemble on the Au facet itself or at the facet boundaries.

sufficient to determine whether the organic compounds start to assemble on the facet itself or at the facet boundaries. A 3D view is necessary to overcome this issue and again, electron tomography is a helpful tool to give more insight. Figure 8.11 illustrates the 3D reconstruction from a $F_{16}CuPc$ nanostructure grown on a Au particle². Again, the sample was rotated in steps of 2° from $\pm 58^\circ$ around the axis denoted in Figure 8.11 (a). Each image in this series was recorded in bright-field imaging mode. By evaluating different snapshots at different perspectives of the 3D reconstruction it is possible to arrive at the conclusion that this $F_{16}CuPc$ nanowire starts to grow from the edge of the Au nanoparticle where a Au facet boundary is likely to be found. However, it is not yet

²Measurements performed by Dr. Yun-Jin Phillipp from the StEM department at the Max-Planck-Institute for Metals Research in the frame of a collaboration.

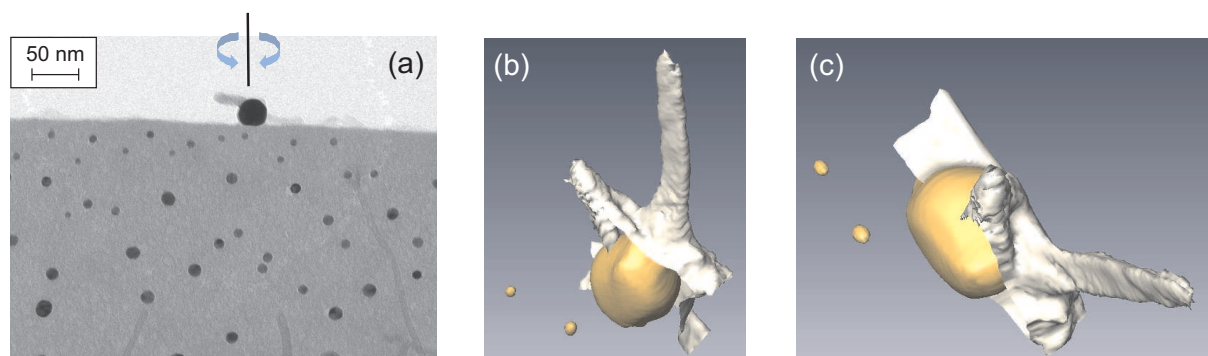


Figure 8.11: (a) Au particle with a $F_{16}CuPc$ nanostructure whose 3D reconstruction is depicted via two snapshots in (b) and (c).

possible to generalize this observation to other molecular compounds or architectures since no statistical investigations have been performed until now as this technique is very time-consuming. In addition, the high contrast ratio between Au nanoparticle and background and the low contrast difference between organic nanostructure and background produces artifacts and makes this analysis very complicated.

8.2 Role of the Gold Substrate

To clarify in general the influence of the gold substrate and especially the role of the polycrystalline domain sizes on the growth mode, various Au surfaces were employed as substrates for the growth of phthalocyanine compounds. In the limit case of a large facet, that is for example the surface of a Au single crystal as shown in Figure 8.12 (a), phthalocyanines lie flat on the surface due to the interaction of the molecular π system with the substrate as commonly observed on other metal surfaces [157, 160, 161, 178, 186]. On flame-annealed Au films which exhibit a polycrystalline structure with grains extended over several microns, the formation of large 3D crystallites can be seen as demonstrated by Figure 8.12 (b). This growth mode has been reported and it obeys to the completion of few layers with the molecules oriented parallel to the surface as a result of the interaction with the metal substrate, which is followed by the growth of molecules in an energetically preferred standing-upright orientation [205, 206]. The situation changes however if the grains decrease in size. On non-annealed polycrystalline Au films with typical grain sizes below ~ 100 nm, the assembly of 1D structures is indeed observed as illustrated in Figure

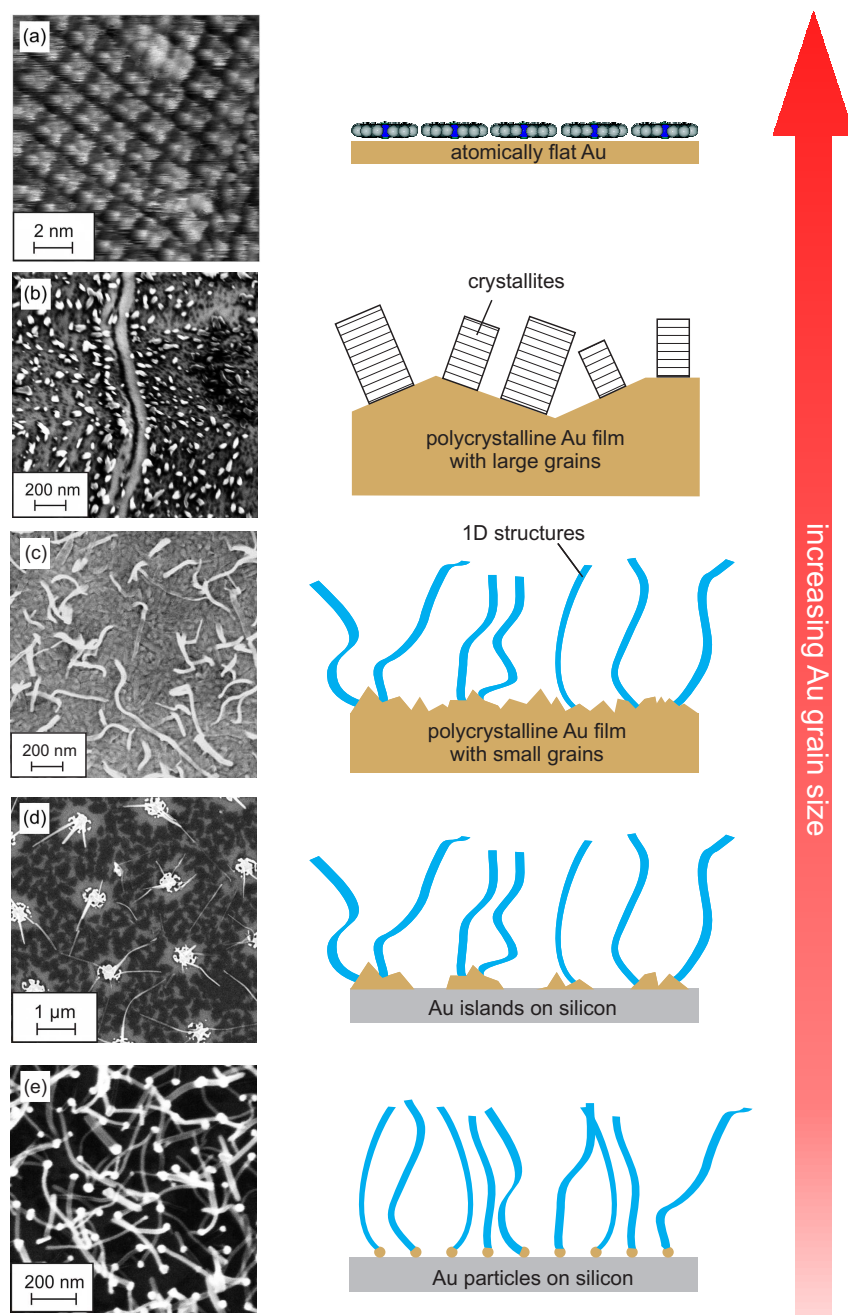


Figure 8.12: (a) - (e) SEM images of phthalocyanines grown on different Au morphologies. (a) On atomically flat Au, the phthalocyanine derivatives lie flat on the surface. (b) Organic 3D crystallites form on Au films with micron-sized grains. (c) A reduction of the Au grain size (~ 100 nm) leads to a 1D growth mode. (d) Hence, patterned Au nanostructures offer a route for the growth of 1D organic structures with spatial control. (e) Templates of gold nanoparticles allow both, precise control of the nucleation site and uniform widths of the respective phthalocyanine nanostructures.

8.12 (c). In order to have spatial control, silicon substrates were patterned by electron beam lithography fabricating nanostructures which consist in islands of polycrystalline Au. From Figure 8.12 (d), it can be seen that the 1D growth occurs selectively on top of the Au islands while a smooth film grows onto the surrounding silicon substrate. The depletion zone around the Au islands reflects the collection area for this temperature due to molecular diffusion which will be discussed in detail in section 8.3. In general, the amount of 1D structures increase with the size of the respective Au island diameter. In addition, as demonstrated on the Au nanoparticles, longer 1D structures form on smaller Au islands. For completeness, Figure 8.12 (e) depicts again the scenario for the Au nanoparticles which allow a precise control of the nucleation site and uniform widths of the respective phthalocyanine nanostructures.

8.3 Influence of Substrate Temperature

By a careful inspection of Figure 8.13 (a), which shows again the sample with patterned Au islands from Figure 8.12 (d), a brighter region can be recognized around each Au island

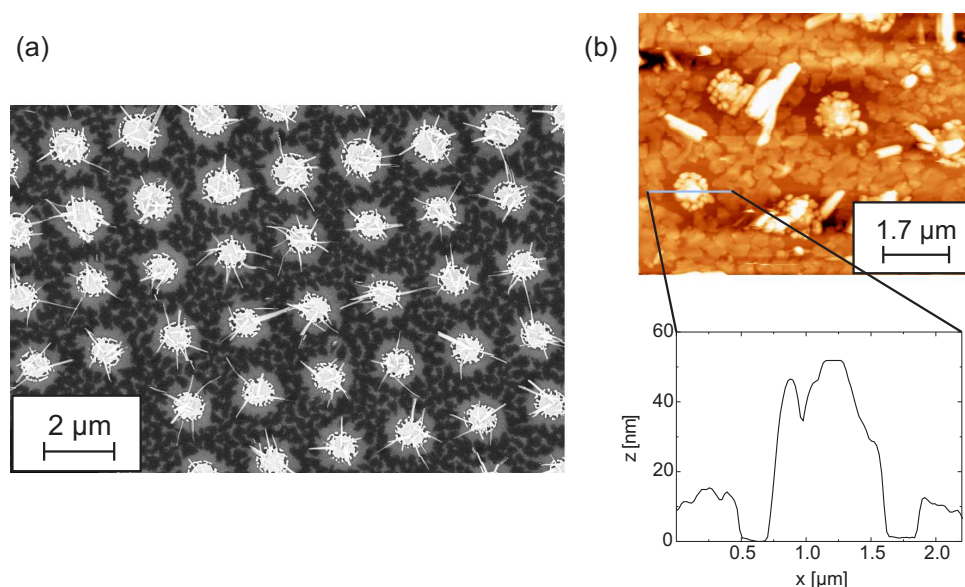


Figure 8.13: (a) SEM image of the sample patterned with Au islands. Brighter regions are visible around each Au island proposing a surface diffusion of the molecular compounds. (b) AFM image with height profile which also illustrates the loss in organic material close to the Au islands.

which corresponds to a depletion area due to surface diffusion of the molecular compounds to the respective Au island. The AFM image with the corresponding height profile of the Au template in Figure 8.13 (b) supports this suggestion since less organic material is found around areas close to the Au islands as compared to areas more distant to the Au islands. More detailed measurements are not possible due to the strong interaction between the 1D structures and the tip which finally destroy it. However, from these results it can be seen that the 1D growth will be largely determined by an interplay of diffusion processes (between and on top of the Au islands).

The effect of the substrate temperature on the growth and diffusion process of $H_{16}CuPc$ was studied in detail on silicon wafers modified by arrays of Au nanoparticles. Here, the diffusion length of $H_{16}CuPc$ is expected to be in a similar range than the distance of adjacent Au nanoparticles (~ 70 nm), in contrast to the sample with the patterned Au islands where the diffusion length (as estimated from the depleted region around the Au islands) is much shorter than the distance between Au islands (~ 1 μ m). Substrate temperatures between ~ 48 $^{\circ}C$ and ~ 140 $^{\circ}C$ during deposition were chosen with rates of ~ 0.4 $\text{\AA}/\text{min}$ and a nominal thickness of ~ 200 \AA . In order to correct possible deviations of the thickness measured by the quartz crystal micro balance during growth at 48 $^{\circ}C$ and 140 $^{\circ}C$, two calibration samples were prepared at these temperatures. A scheme of the structural parameters analyzed is demonstrated in Figure 8.14. Beside the length L_{1D} of the 1D structures which were analyzed by SEM in back-scattered electron imaging mode, the thickness D of the wetting film was measured by x-ray reflectivity. The SEM images (left) together with the x-ray reflectivity data (right) can be seen in Figure 8.15. The

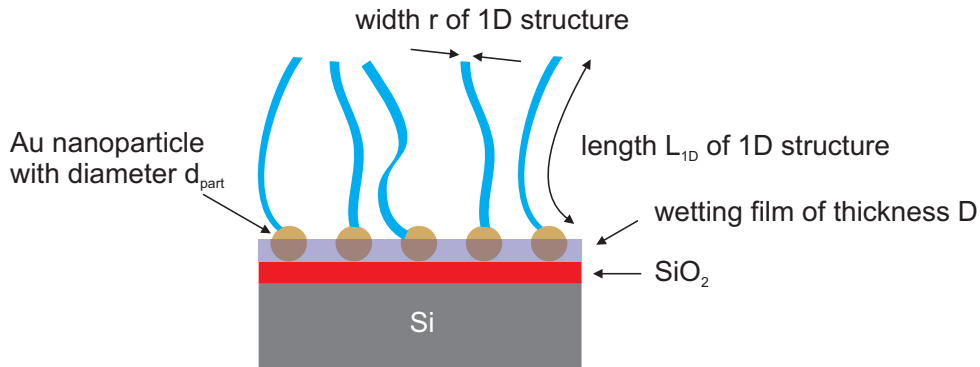


Figure 8.14: Schematic side view of the samples illustrated in Figure 8.15. A wetting film of thickness D is forming in addition to the 1D structures of length L_{1D} .

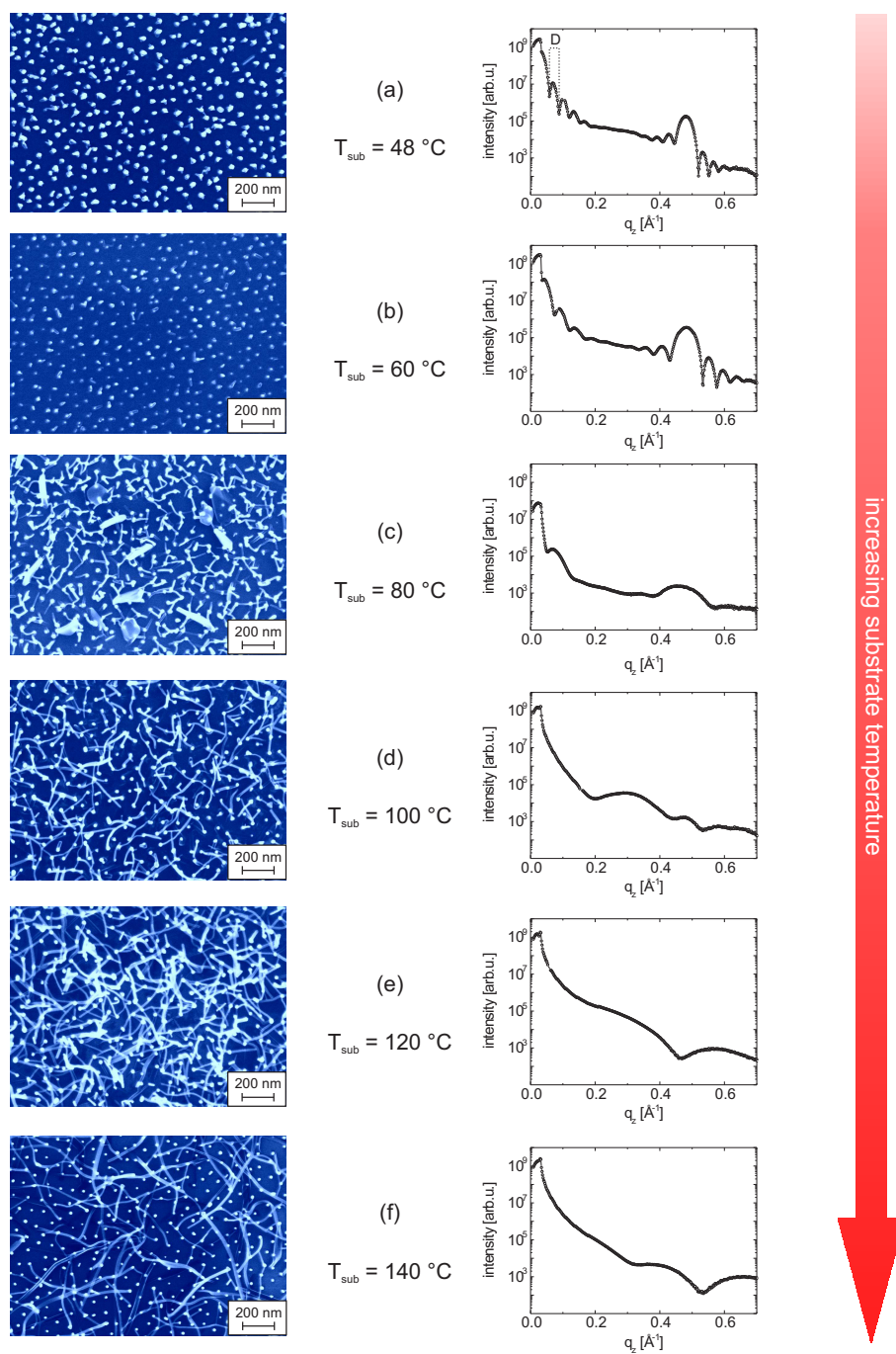


Figure 8.15: (a) - (f) SEM images (left) of $H_{16}CuPc$ grown at different substrate temperatures T_{sub} with the corresponding x-ray reflectivity measurements (right). The 1D structures are increasing while the thickness of the wetting film is decreasing with increasing T_{sub} .

growth mode as a function of T_{sub} can be seen in Figure 8.15. At $T_{sub} = 48$ °C, only few wire-like structures with very short lengths (below 40 nm) form as depicted in Figure 8.15 (a). The x-ray reflectivity data indeed show that the $H_{16}CuPc$ molecules grow forming a film. Similarly to the growth on bare SiO_2 , the (001) Bragg reflection is observed together with the Laue oscillations indicating a well-ordered layered structure with an interlayer spacing of 13.06 Å. The thickness D of the wetting film estimated from the Kiessig fringes indicates a thickness of 206 Å. For the sample grown at $T_{sub} = 60$ °C, the length of the 1D structures is still rather short as illustrated in Figure 8.15 (b). However, the thickness of the wetting film is noticeable smaller than at 48 °C as proven by the expansion of width of the Kiessig fringes. At $T_{sub} = 80$ °C, shown in Figure 8.15 (c), there is a remarkable onset of the 1D growth mode accompanied by a reduction in the thickness of the wetting film which is again manifested by the larger width of the Kiessig fringes. This trend, i.e. larger 1D structures and thinner wetting film, continues with increasing T_{sub} , as can be seen from Figure 8.15 (d) - (f). When the growth takes place at $T_{sub} = 140$ °C, the 1D structures finally exhibit lengths in the micrometer length scale. A wetting film is still present but with a thickness equivalent to about one monolayer of standing $H_{16}CuPc$ molecules.

To attain precise knowledge about the length L_{1D} of the 1D structures, a statistical analysis of various SEM micrographs was carried out. Accurate information on the thickness D of the wetting film was gained by fitting once again all x-ray reflectivity curves

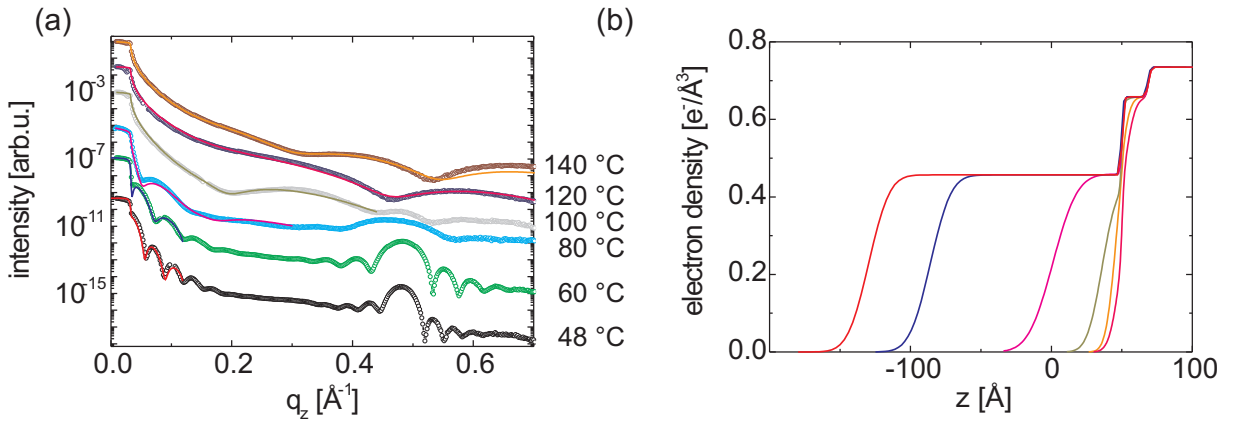


Figure 8.16: (a) Fits of the x-ray reflectivity curves obtained at substrate temperatures T_{sub} between 48 and 140 °C. The data sets are shifted for clarity. (b) Corresponding electron density profiles showing the decreasing thickness of the wetting film with increasing T_{sub} .

using the Parratt formalism [101]. The fits together with the corresponding electron density profiles can be seen in Figure 8.16. Only the part containing the Kiessig fringes is fitted to keep each fit simple with few parameters. One box is applied to describe the H_{16}CuPc film and two boxes for the substrate (SiO_2 and silicon). This simple model allows to fit the x-ray reflectivity data with a good agreement. In addition, the mean electron density $\bar{\rho}_{fit} = 0.46 \text{ e}^-/\text{\AA}^3$ is also consistent with the one deduced from the volume of the unit cell ($\bar{\rho}_{mol} = 0.49 \text{ e}^-/\text{\AA}^3$) [60]. A summary of all parameters which generate the fits can be found in the appendix C.2. If the length of the 1D structures as a function of substrate temperature is plotted, as shown in Figure 8.17 (a), an exponential dependence can be identified. An exponential decrease is found for the thickness of the wetting film with increasing T_{sub} as demonstrated in Figure 8.17 (b).

At first sight, there seems to be a contradiction as one would expect the thickness of the wetting film to decrease with T_{sub} in the same way as the length of the 1D structures increases, as indicated by the dashed line in Figure 8.17 (b) obtained assuming mass conservation. But this gives already a hint that the growth scenario is more complex and has to be investigated in more detail. The actual question is where the molecules can be found which are neither contributing to the 1D growth nor forming a wetting film on the substrate. To get an insight about the morphology, a TEM characterization was carried

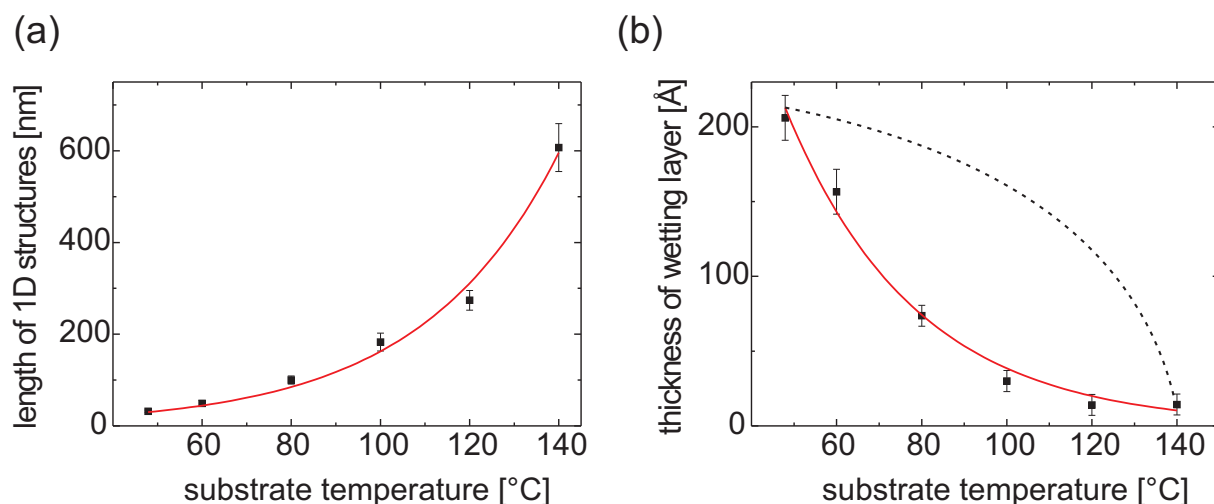


Figure 8.17: (a) An exponential growth mode can be identified when the length of the 1D structures is plotted as a function of T_{sub} . (b) In the case of the wetting film, an exponential decay is observed by increasing T_{sub} . The dashed line indicates the expected behavior of the film thickness.

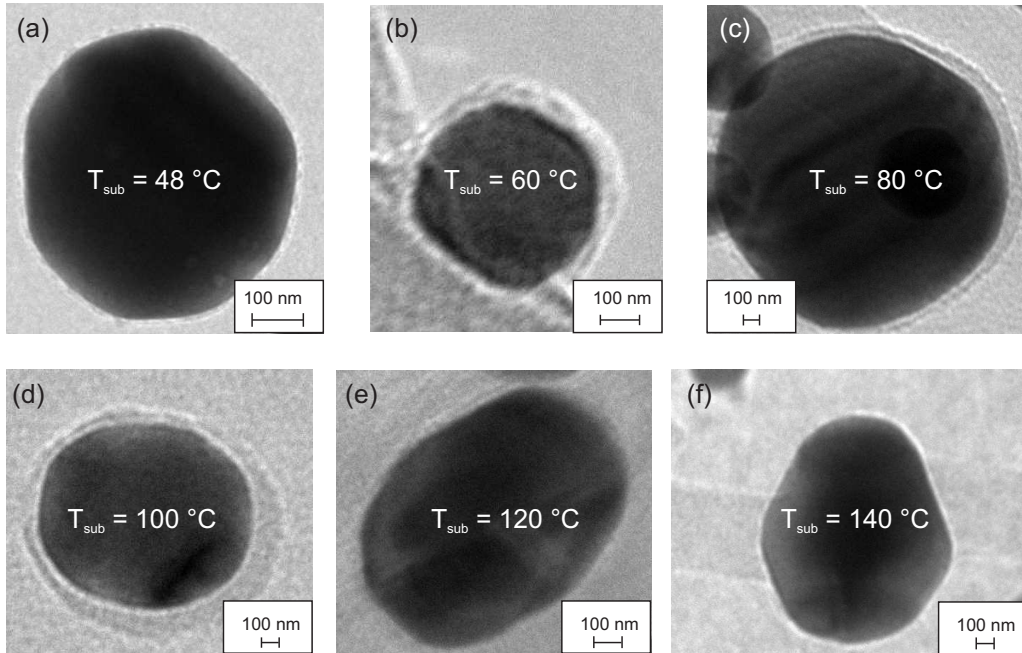


Figure 8.18: (a) - (f) Representative TEM images of the wetting layer surrounding the Au nanoparticles at different T_{sub} .

out on Si_3N_4 membranes modified with Au nanoparticles which were simultaneously grown with the Au nanoparticle samples analyzed above (see Figure 8.18). Figure 8.18 (a) - (f) reveals that the Au nanoparticles are covered by a wetting layer whose thickness varies with increasing substrate temperatures. The graph in Figure 8.19 (a) depicts the outcome by performing a statistical evaluation of the thickness of the wetting layer at each T_{sub} . It can be seen that the wetting layer around the Au nanoparticles is increasing until $T_{sub} = 100$ °C. It indicates that for this temperature window, from room temperature to 100 °C, not all organic material contributes to the growth of the 1D structures since a considerable amount diffuses to the Au nanoparticles and forms a wetting layer. This is the origin of the strong decline of the film thickness shown in Figure 8.17 (b) for this temperature range. Above $T_{sub} = 100$ °C, a big drop of the thickness of the wetting layer around the Au nanoparticles is observed which ends up in virtually 0 ± 8 Å. This means that now almost all incoming molecules grow forming 1D structures which is the favored mode as T_{sub} increases. The scheme in Figure 8.19 (b) summarizes the growth mode at different substrate temperatures.

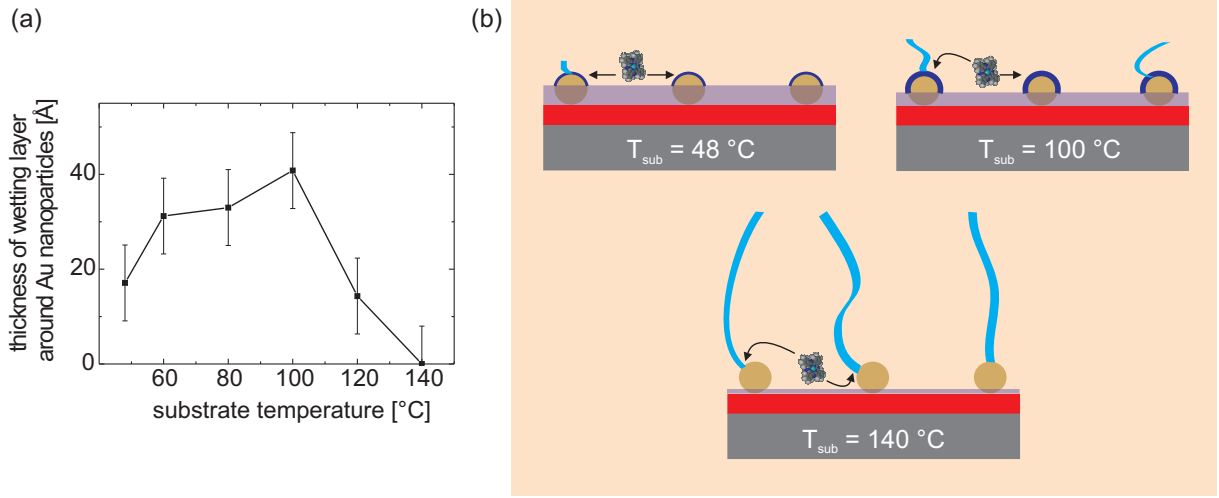


Figure 8.19: (a) The graph shows the results of a statistical evaluation of the thickness of the wetting layer surrounding the Au nanoparticles at different T_{sub} . The thickness of the wetting layer is increasing till $T_{sub} = 100$ °C. Above $T_{sub} = 100$ °C, a big drop is visible. (b) Scheme summarizing the growth mode.

To check the consistency of the found values, a simple model given by

$$M = \rho\pi (r/2)^2 L_{1D} + \rho D A_D + 4\rho\pi (d_{part}/2)^2 D_{Au} \quad (8.1)$$

can be attributed to the total mass per unit area M deposited at different T_{sub} which takes into account the involved mass in the 1D structures, the wetting film and the wetting layer around each Au nanoparticle. ρ is the density, r the mean width of the 1D $H_{16}CuPc$ structures as denoted in Figure 8.14, L_{1D} the average length of the 1D structures, D the mean film thickness and A_D the average area of the unit cell deduced from the Au nanoparticle array. D_{Au} is the thickness of the wetting layer around each Au nanoparticle displayed in Figure 8.19 (a). Dividing M by ρ results in the fitted volume. A_D can be determined by assuming an oblique unit cell of $a = b = 70$ nm and $\gamma = 60^\circ$ and subtracting the projected area $\pi(d_{part}/2)^2$ with a particle diameter $d_{part} = 35$ nm. The overall volume which consists of the volume from the film thickness, the volume from the 1D structures and the volume from the wetting layer surrounding the Au nanoparticle can be estimated at each T_{sub} using a mean width r of 20 nm. The overall volume at room temperature is $\sim 84 \mu m^3$ and at 100 °C $\sim 83 \mu m^3$. The total volume per area is equal to 198 Å and 196 Å respectively, equivalent to the nominal thickness of the deposited film.

Note that at 100 °C, more than 23 % of the total volume is aggregating around the Au nanoparticles.

It can only be speculated about the reasons of such a growth behavior. One aspect which might play a pivotal role in this complex scenario, is the interplay between different physical processes related to different activation energies. It seems that, for T_{sub} below 100 °C, the kinetic energy to diffuse along the surface is in most cases only sufficient to form a wetting layer on the Au nanoparticles coexisting with a film on the substrate. It is suggested that, only after the formation of the wetting layer, several 1D structures are growing whose number is increasing with elevated substrate temperatures. At even higher substrate temperatures (above $T_{sub} = 100$ °C) the molecules are able to diffuse on the SiO_2 , to reach the Au nanoparticles and to assemble immediately in the 1D structures before any thick wetting layer is formed.

This assumption is supported when plotting the natural logarithm of the length of the 1D structures against the inverse of the substrate temperature T_{sub} , as demonstrated in Figure 8.20, also known as Arrhenius plot. The activation energy E_A can be determined from the exponent $-E_A/k_b T_{sub}$ whose prefactor $-E_A/k_b$ corresponds to the gradients shown in Figure 8.20. Here, k_b represents the Boltzmann constant. The activation en-

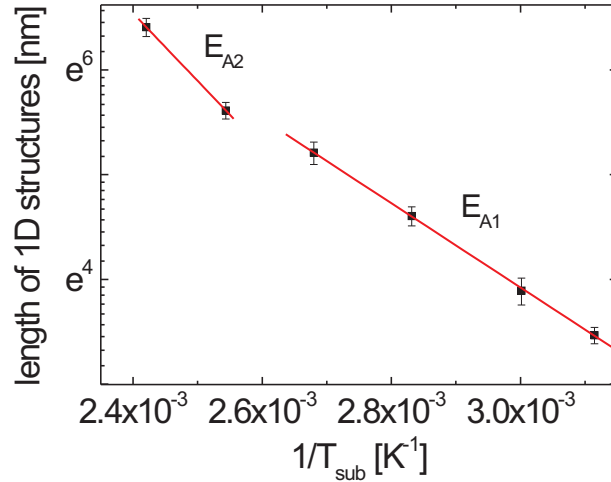


Figure 8.20: Arrhenius plot of the length of the 1D structures as a function of the inverse of the substrate temperature T_{sub} .

ergy can be attributed to a series of thermally activated physical processes that include molecular diffusion on the wetting film surface and along the 1D structures. Thereby, the activation energy can be related to the sum of energy barriers involved in the molecular diffusion towards the Au nanoparticle, on top of the Au nanoparticle and to the 1D structures. From Figure 8.20, two different activation energies can be observed suggesting that there are two growth modes present. From the regime corresponding to the lower T_{sub} it follows, that $E_{A1} = 0.35$ eV which is in good accordance to calculations of diffusion barriers from $H_{16}CuPc$ crystals which are in the range of 0.25-0.35 eV [207]. For the regime above 100 °C, an activation energy of $E_{A2} = 0.56$ eV is found. This seems to indicate an onset of a new mechanism associated to the diffusion of the molecules on the Au directly towards the 1D structures.

8.4 How General Is This Phenomenon?

To test the generality of the growth phenomenon of organic compounds on substrates coated by arrays of Au nanoparticles, the studies were extended to other molecules which exhibit strong crystalline anisotropy like in the case of PTCDI- C_8 and p-6P. The growth

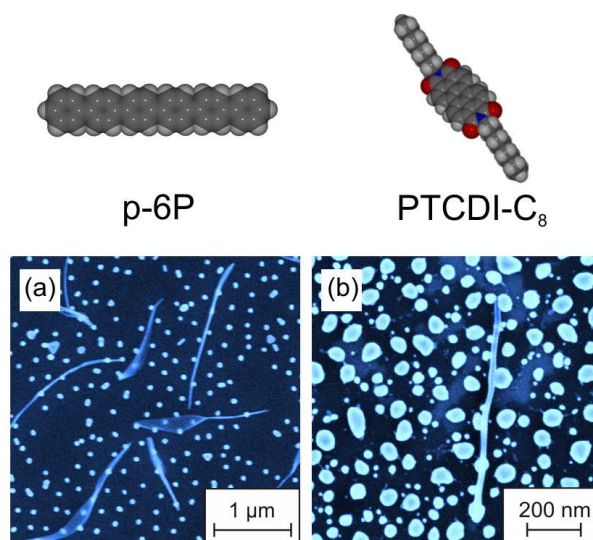


Figure 8.21: SE micrographs showing the growth modes of (a) p-6P and (b) PTCDI- C_8 on silicon wafers modified by arrays of Au nanoparticles measured at $T_{sub} = 120$ °C. Only very few 1D nanostructures are evolving in comparison to the scenario observed for phthalocyanine compounds.

on the Au templates was investigated for various substrate temperatures. As illustrated in Figure 8.21 (a), para-sexiphenyl (p-6P) ignores the Au particles growing mainly in a thin film morphology with the formation of only a few 1D structures. A similar scenario is observed for PTCDI-C₈ but here, the quantity of 1D architectures is even less as can be seen in Figure 8.21 (b). The formation of 1D nanostructures appears to be exclusive for the family of phthalocyanines and it is suggested that the template-induced 1D growth is an intrinsic self-assembly property rather than a purely kinetically determined growth mode.

The growth on nanoparticle templates of other metals (Pt and Pd) was investigated in order to probe if this is a specific property of the interaction of phthalocyanines with Au (see Figure 8.22). The evaporation of H₁₆CuPc on Pt nanoparticles at $T_{sub} = 120$ °C also results in 1D structures as proven by Figure 8.22 (a). However, the quantity of 1D structures is less than in the case of the surfaces modified by Au nanoparticles. The less effective 1D growth might be attributed to the smaller diameter of the Pt nanoparticles which is around the critical diameter of the Au nanoparticles below no 1D growth occurs. The widths of the observed 1D structures comprise dimensions between 20 and 40 nm and are very similar to the ones found on the Au nanoparticles. In contrast, the templates of Pd nanoparticles do not lead to the formation of 1D structures as shown in Figure 8.22 (b). Up to now, it is not clear if this is due to the small diameter of all Pd nanoparticles which is below the critical diameter or if it is a material specific property.

Beside silicon wafers, glass substrates coated by an indium tin oxide (ITO) layer were

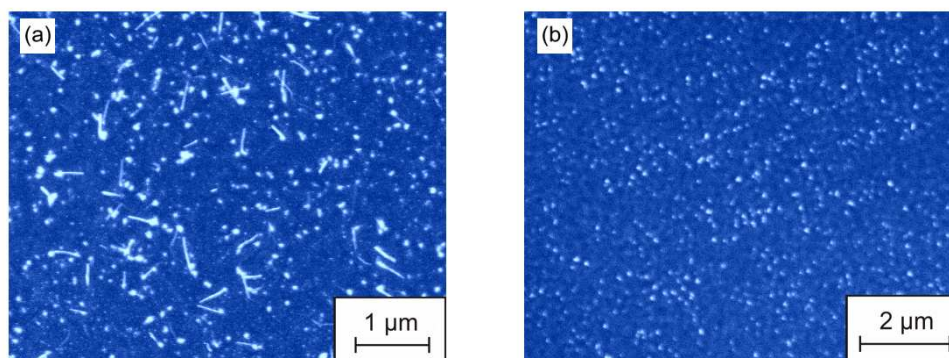


Figure 8.22: SEM images of silicon wafers covered by (a) Pt nanoparticles and (b) Pd nanoparticles which were subsequently evaporated by H₁₆CuPc at $T_{sub} = 120$ °C. On the Pt nanoparticles, 1D structures assemble in contrast to the Pd nanoparticles where no 1D growth mode is observed.

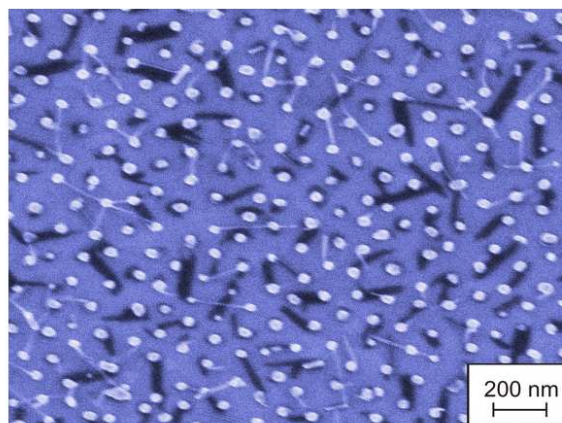


Figure 8.23: SEM image of a glass substrate coated by an indium tin oxide layer on which Au nanoparticles were deposited. Afterwards, $H_{16}CuPc$ was evaporated at a substrate temperature of $100\text{ }^{\circ}C$ which form 1D structures.

used as substrates on which Au nanoparticles were deposited. This is of high technological interest since ITO substrates play an important role in the fabrication process of organic solar cells as transparent electrical electrode. The growth mode of $H_{16}CuPc$ is demonstrated in Figure 8.23. Again, 1D structures are forming with a high selectivity. The widths range between 10 and 35 nm, exactly the same dimensions found on the silicon wafers. Therefore, it is demonstrated that this strategy can be employed to fabricate highly interpenetrated and crystalline comb-shaped p-n heterojunctions for solar cells.

8.5 Conclusions

It is shown that the growth of 1D structures on templates of Au nanoparticles is a general process for planar phthalocyanine derivatives. Such selective 1D growth does not occur for other anisotropic organic molecules such as p-6P or PTCDI- C_8 suggesting a self-assembly property attributed to phthalocyanine compounds. It is proven that the 1D architectures have a monocrystalline structure. From a statistical study of the impact of the nanoparticle size, it can be concluded that a minimum Au nanoparticle diameter is necessary to trigger a 1D growth mode. It is demonstrated that the 1D assembly can be promoted by polycrystalline Au films if sufficiently small crystalline grains are present. Thus, the patterning of silicon substrates with polycrystalline Au islands can be used as a second route for directing the growth of 1D phthalocyanine structures. Although the

role of the crystallinity and Au facets is still not totally clarified, this work shows that both, size of the facets and curvature are crucial factors to induce the 1D assembling of phthalocyanines. The effect of the substrate temperature reveals a more complex growth scenario in which the wetting of the Au nanoparticles plays a pivotal role. Eventually, it is shown that this 1D growth process can be induced by templates of other metal nanoparticles and even on different substrates such as ITO which are relevant in the organic photovoltaics manufacture.

With the ability at hand to grow 1D organic monocrystalline structures with precise localization and tunable dimensions of both, n- and p-type materials on various substrates opens exciting possibilities for the bottom-up fabrication of nanodevices and in particular, for attaining highly efficient charge carrier collection and exciton diffusion efficiencies in nanostructured solar cells.

9 Summary and Outlook

This thesis has pursued the understanding and control of growth and self-assembly mechanisms of technologically relevant organic semiconductors in different dimensionalities for an optimum implementation into organic field effect transistors (OFETs) and organic photovoltaic cells (OPVs).

The preparation and structural characterization of organic n- and p-type semiconductors forming various architectures was in the focus of this work. By means of atomic force microscopy (AFM), in-situ and ex-situ x-ray reflectivity (XRR) and grazing incidence x-ray diffraction (GIXD), the structural properties of 3D PTCDI-C₈ thin films on SiO₂ and Al₂O₃ were revealed. Pentacene, F₁₆CuPc and their 2D binary systems on Cu(100) were studied employing scanning tunneling microscopy (STM). Finally, the 1D assembly of phthalocyanine compounds on silicon wafers and indium tin oxide (ITO) modified by metal nanoparticles were elucidated by the use of scanning electron microscopy (SEM) and transmission electron microscopy (TEM) in combination with XRR.

A detailed structural investigation of PTCDI-C₈ thin films on SiO₂ was performed including the determination of the oblique in-plane unit cell [12]. A model for the molecular orientation along the surface normal is described which suggests a tilted configuration of the PTCDI-C₈ molecule with respect to surface plane. In contrast to a previous study of a PTCDI derivative where the alkyl chains of vicinal molecules are reported to interdigitate [14], no interdigitation of the alkyl chain takes place in the growth scenario analyzed for PTCDI-C₈. In addition, it was found that the topmost layer of the PTCDI-C₈ film is smaller in thickness than the layers below which can be attributed to a more tilted orientation of the alkyl chains away from the surface normal to compensate the loss in cohesive energy at the organic-air interface. The increase of substrate temperature resulted

in smoother films with an expansion of the needle terraces. The domain size estimated for the film grown at room temperature is considerably smaller than the characteristic island (and grain) length observed by AFM. Moreover, similar widths of the (100) and (010) peaks indicate a rather isotropic growth along the different crystallographic directions, which differs from the expectation of a faster growth along the π - π stacking direction, i.e. along the [010] direction, as observed in the growth of PTCDI-C₈ single-crystals. It is also observed that, with increasing growth temperature, there is an enlargement of islands sizes without any significant growth of the lateral crystalline domains. Finally, a post-thermal treatment leads to the best ordering in the multilayer structure proposing an improved electron mobility in OFETs under such conditions. The presented results propose that a considerable reduction in the density of grain boundaries together with a better vertical ordering in the thin film structure are responsible for an enhancement of the PTCDI-C₈ OFETs performance.

On Al₂O₃, the full 3D molecular packing of PTCDI-C₈ was for the first time characterized by GIXD using a linear detector [13]. The square modulus of the structure factor as a function of the rotation of the PTCDI-C₈ molecule within the unit cell was simulated and compared to the measured experimental data to obtain the molecular orientation. From the best fit, it could be deduced that the molecular plane of the aromatic core is tilted with respect to the surface plane and that the PTCDI-C₈ molecules stack in a cofacial packing along the *b*-axis. Interestingly, the in-plane unit cell and the tilt angle evidence a thin-film structure similar to the one investigated on SiO₂ which indicates that the molecule-substrate interactions are less dominant than the molecular interactions. Furthermore, a vertical coherence length is obtained that coincides with the film thickness implying that 3D crystallites extend across the entire thickness of the layered film on Al₂O₃. The characterization of the molecular packing of this organic thin film is one of the basic requirements in calculating the associated electronic band structure and in modeling the charge-transport properties in organic thin film transistor devices. This could shed light on a more comprehensive understanding of the correlation between structural and electrical properties.

The studies of binary systems of F₁₆CuPc and pentacene have shown highly ordered 2D supramolecular structures promoted by intermolecular interactions [17]. A crystalline nanoporous network has been tailored by a pentacene:F₁₆CuPc ratio of 2:1. The mixed

layers of pentacene/ F_{16} CuPc and the F_{16} CuPc films show two enantiomorphic chiral domains with high structural order in contrast to pentacene which exhibits no long range order in pure films. A model of the epitaxial relationship on Cu(100) is given which suggests C-F \cdots H bondings as possible driving force for the bimolecular self-assembly in addition to the still strong interaction between substrate and organic bilayer. These results illustrate demonstratively how the interplay between intermolecular and molecule-substrate interactions can tune and dictate the self-assembly properties of supramolecular structures. Furthermore, the nanoporous system offers the possibility to act as template for the complexation of other molecular species and the formation of 3D architectures.

Finally, it was shown how to induce a 1D growth mode of various phthalocyanine derivatives by the use of silicon wafers coated by Au nanoparticles. The structural properties and the growth process of this phenomenon was analyzed for H_{16} CuPc, H_{16} CoPc, F_{16} CoPc and F_{16} CuPc [19]. Beside nanobelts, nanowire-like structures could be observed whose monocrystalline architectures could be determined by high resolution TEM. From a statistical investigation, it could be proven that a minimum diameter of the Au nanoparticle is necessary to provoke the 1D growth behavior. It could be demonstrated that, instead of employing Au nanoparticles, polycrystalline Au films can trigger as well a 1D growth mode if sufficiently small grains are present. Therefore, the patterning of silicon substrates with polycrystalline Au islands offers an alternative way for the formation of 1D structures. The influence of the substrate temperature on the growth scenario was characterized by SEM and TEM in combination with XRR. It could be observed that the thickness of the organic wetting film (which is present at any substrate temperature) decreased whereas the length of the 1D structures increased with increasing substrate temperature. A model was developed to describe this complex growth process which also takes into account the organic wetting layer surrounding each Au nanoparticle whose thickness is also dependent on the substrate temperature. Finally, the generality of the 1D growth mode was probed for Pt and Pd nanoparticles and indium tin oxide (ITO) substrates, which are crucially relevant for the fabrication of OPVs. The given results are very promising for an optimum performance of OPVs since it is now possible to create highly selective, monocrystalline 1D architectures of organic p- and n-type semiconductors with precise localization and tunable dimensions on technologically significant substrates such as SiO_2 or ITO.

A thesis should be never considered as complete. Some open questions could be tackled within this work but at the same time, new unsolved questions arose which might pave the way to interesting studies in the near future. In the following, some of the most intriguing issues are listed.

It is of great interest to apply and refine the presented method for the determination of a full 3D molecular packing to other organic compounds in thin films. For almost all oligomers, the molecular orientation in thin films is still unknown which is a bottle neck for a theoretical modeling of the electrical and optical performance in devices.

Regarding the supramolecular 2D assembly, further research could be done for other molecular ratios of pentacene and F₁₆CuPc. For a more comprehensive description of the involved interactions, different substrates might be also employed. In addition, the observed mixed nanoporous layer of pentacene and F₁₆CuPc may be used as a template for further growth of a third component to build highly ordered 3D structures.

Several questions are still open concerning the origin in the diversity of the 1D structures. Furthermore, a statistical investigation has to be performed to support the observation that the nucleation of the 1D structure takes mainly place on the Au facet boundaries. The role of the Au nanoparticles' curvature is still unknown. It is also not understood why phthalocyanine derivatives allow such a selective 1D growth mode on Au nanoparticles whereas other compounds with strong anisotropic crystallinity do not show such a behavior. Nevertheless, the 1D growth phenomenon has the potential to be implemented into organic solar cells. It was shown that this growth mode is successfully reproduced on ITO substrates with a p-type semiconductor. Now, the next step which is planned will include the filling of the volume between the 1D p-type structures of H₁₆CuPc on ITO with an n-type material such as the fullerene C₆₀ to form a donor-acceptor comb-shaped architecture. Finally, a capping layer of aluminum should be evaporated to make the organic solar cell complete for efficiency measurements. Additional buffer layers, such as lithium fluoride, between the active film and the aluminum electrode could be employed to further enhance the performance in organic solar cells.

A Transformation from Real Space to Reciprocal Space

In order to explain the transformation of the collected data from real space to reciprocal space, the parameters depicted in Figure A.1 are introduced. Here, the x-ray beam travels in y-direction and the surface normal is aligned along the z-direction. The incoming and outgoing wave vectors in the surface frame are expressed via

$$\mathbf{k}_i = \begin{pmatrix} 0 \\ k \\ 0 \end{pmatrix} \quad (\text{A.1})$$

and

$$\mathbf{k}_f = \Delta\Omega \begin{pmatrix} 0 \\ k \\ 0 \end{pmatrix} \quad (\text{A.2})$$

respectively, with $k = 2\pi/\lambda$ being the wave vector.¹ Note that the inner circle is the ϵ -circle for the diffractometer at the beamline ID10B implying that the rotation around the x-axis always takes place before a rotation around the z-axis.

Therefore, the order of the orientation matrices in equation A.2 is such that the incoming wave vector has first to be multiplied by matrix Ω before any multiplication is done with Δ . The orientation matrices Δ and Ω are calculated by the angular settings for the

¹For a complete description, the incoming and outgoing wave vectors have to be multiplied by an additional matrix M which takes the angular settings of the sample with respect to the surface frame into account. Here, this matrix can be neglected due to small incoming angles.

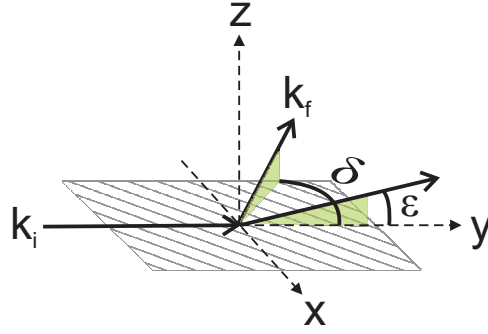


Figure A.1: Introduction of the parameters used in the text to derive the transformation from real space into reciprocal space.

detector (δ, ϵ) by

$$\Delta = \begin{pmatrix} \cos \delta & \sin \delta & 0 \\ -\sin \delta & \cos \delta & 0 \\ 0 & 0 & 1 \end{pmatrix} \quad (\text{A.3})$$

$$\Omega = \begin{pmatrix} 1 & 0 & 0 \\ 0 & \cos \epsilon & \sin \epsilon \\ 0 & -\sin \epsilon & \cos \epsilon \end{pmatrix}. \quad (\text{A.4})$$

The scattering vector is determined in the usual way by

$$\mathbf{q} = \mathbf{k}_f - \mathbf{k}_i = k \begin{pmatrix} \sin \delta \cos \epsilon \\ \cos \delta \cos \epsilon - 1 \\ -\sin \epsilon \end{pmatrix}. \quad (\text{A.5})$$

This relation can now be exploited to deduce the modulus of q_{\parallel} and q_z resulting in

$$q_{\parallel} = k \sqrt{\cos^2 \epsilon - 2 \cos \delta \cos \epsilon + 1} \quad (\text{A.6})$$

and

$$q_z = k \sin \epsilon. \quad (\text{A.7})$$

B Correction Factors

In scattering experiments the measured intensity differs from the theoretically calculated intensity due to several geometrical reasons. In order to obtain the total intensity, some considerations and corrections have to be accomplished.

B.1 Offset Scan and Footprint

As a consequence of the earlier mentioned interface roughness, the specularly reflected intensity is reduced since a part is scattered into other (non-specular) directions. Whereas the specular scattering contains information on the structure projected to the surface normal, the non-specularly reflected or diffuse intensity is sensitive to the roughness correlation of surfaces and interfaces due to the non-zero component of the momentum transfer in the plane. In order to subtract the diffuse scattering from the specular scattering, a so-called offset-scan is performed where the scattered intensity is measured at a position $\theta_i = \theta_f \pm \theta_{off}$ near the specular position since the diffuse scattering varies on a larger length scale than the specular scattering.

In this thesis, the data of the offset-scan are always subtracted from the measured intensity prior to any fit by the Parratt algorithm.

The intensity has also to be corrected concerning the illumination area due to the footprint of the x-ray beam which is larger than the sample dimension for low incident angles. The measured intensity I_{mes} has to be modified by

$$I_{mes} = I_{calc} \cdot \sin \theta_i \cdot \frac{L_s}{s} \quad (\text{B.1})$$

where I_{calc} is the theoretically calculated intensity, s the slit setting of the incoming beam and L_s the length of the sample.

B.2 Geometrical Correction Factors

Beside the aforementioned modifications of the measured intensity, some additional correction factors have to be included, especially when integrated intensities are determined [142,143]. For the experiments performed in this thesis, a geometrical area correction factor C_A has to be applied. In addition, a polarization correction factor C_P has to be included depending on the scattering geometry and the polarization of the x-ray beam. In the stationary geometry, i.e. the sample is not rotated during the scan with respect to the incoming beam, a geometrical correction factor has to be added which takes into account that the integration is performed in reciprocal space. The necessary transformation of the angular integration variables to reciprocal space variables implies a geometrical correction in the integration volume (C_L). In this thesis, the measured intensity is related to the theoretically calculated one by

$$I_{mes} = I_{calc} \cdot C_A \cdot C_P \cdot C_L \quad (\text{B.2})$$

where

$$C_A = \frac{1}{\sin \delta} \quad (\text{B.3})$$

$$C_P = \cos^2 \epsilon \cdot \cos^2 \delta + \sin^2 \epsilon \quad (\text{B.4})$$

$$C_L = \frac{1}{\sin \epsilon} . \quad (\text{B.5})$$

C Relevant Parameters of the Fits

C.1 Fit Parameters of the PTCDI-C₈ Multilayer Film on SiO₂

The following table summarizes all parameters which generate the fit to the multilayer system of PTCDI-C₈ on SiO₂.

	ρ [e ⁻ /Å ³]				h_1 [Å]			σ [Å]	
Si	0.714								
SiO ₂	0.657				18.6				
	ρ_1	ρ_2	ρ_3	ρ_4	h_1	h_2	h_3	h_4	
interf. layer	0.441	0.286	0.105	0.529	5.12	4.04	6.47	1.50	
PTCDI-C ₈ (first 10 l.)	0.529	0.267	0.056	0.284	8.81	4.80	3.35	3.73	
PTCDI-C ₈ (2nd last l.)	0.522	0.196	0.047	0.253	9.46	4.67	3.26	3.39	
PTCDI-C ₈ (last l.)	0.444	0.355	0.001	0.176	7.87	2.75	7.93	7.59	1.55

C.2 Fit Parameters of the H₁₆CuPc Multilayer Film on SiO₂ at Different T_{sub}

The following table summarizes all parameters which generate the fits to the multilayer system of H₁₆CuPc on SiO₂ coated by Au nanoparticles at different substrate temperatures T_{sub} .

	ρ [e ⁻ /Å ³]	h_1 [Å]	σ [Å]
Si	0.735		1.513
SiO ₂	0.659	18.54	1.146
H ₁₆ CuPc at $T_{sub} = 48$ °C	0.451	186.13	14.555
H ₁₆ CuPc at $T_{sub} = 60$ °C	0.457	135.5	11.649
H ₁₆ CuPc at $T_{sub} = 80$ °C	0.459	49.34	13.694
H ₁₆ CuPc at $T_{sub} = 100$ °C	0.439	14.06	8.389
H ₁₆ CuPc at $T_{sub} = 120$ °C	0.502	0.29	6.135
H ₁₆ CuPc at $T_{sub} = 140$ °C	0.619	3.89	5.967

D Atomic Form Factors

Table D.1 lists all values of the dispersion and absorption correction factors at an energy of 7998.99 eV which have been used to deduce the structure factor F of PTCDI-C₈ thin films.

	N	C	O
f'	0.0294	0.0171	0.0469
f''	0.0183	0.0092	0.0327

Table D.2 summarizes the parameters a_i , b_i and c used in equation 4.3 for each type of atom [100].

	H	N	C	O
a_1	0.493002	12.2126	2.31000	3.04850
b_1	10.5109	0.005700	20.8439	13.2771
a_2	0.322912	3.13220	1.02000	2.28680
b_2	26.1257	9.89330	10.2075	5.70110
a_3	0.140191	2.01250	1.58860	1.54630
b_3	3.14236	28.9975	0.568700	0.323900
a_4	0.040810	1.16630	0.865000	0.867000
b_4	57.7997	0.582600	51.6512	32.9089
c_0	0.003038	-11.529	0.215600	0.250800

List of Publications

D. G. de Oteyza, T. N. Krauss, E. Barrena, S. Sellner, and H. Dosch, J. O. Ossó, *Towards controlled bottom-up architectures in organic heterostructures*, Appl. Phys. Lett. **90**, 243104 (2007), Cover Picture.

E. Barrena, X. N. Zhang, B. N Mbenkum, T. Lohmueller, T. N. Krauss, M. Kelsch, P. A. van Aken, J. P. Spatz, and H. Dosch, *Self-Assembly of Phthalocyanine Nanotubes by Vapor-Phase Transport*, ChemPhysChem **9**, 1114 (2008).

T. N. Krauss, E. Barrena, X. N Zhang, D. G. de Oteyza, J. Major, V. Dehm, F. Würthner, L. P. Cavalcanti, and H. Dosch, *Three-Dimensional Molecular Packing of Thin Organic Films of PTCDI-C₈ Determined by Surface X-ray Diffraction*, Langmuir **24**, 12742 (2008).

T. N. Krauss, E. Barrena, D. G. de Oteyza, X. N Zhang, J. Major, V. Dehm, F. Würthner, and H. Dosch, *X-ray/Atomic Force Microscopy Study of the Temperature-Dependent Multilayer Structure of PTCDI-C₈ Films on SiO₂*, J. Phys. Chem. C **113**, 4502 (2009).

D. G. de Oteyza, E. Barrena, Y. Zhang, T. N. Krauss, A. Turak, A. Vorobiev, and H. Dosch, *Experimental Relation between Stranski-Krastanov Growth of DIP/F₁₆CoPc Heterostructures and the Reconstruction of the Organic Interface*, J. Phys. Chem. C **113**, 4234 (2009), Cover Picture.

T. N. Krauss, E. Barrena, H. Dosch, and Y. Wakayama, *Supramolecular Assembly of a 2D Binary Network of Pentacene and Phthalocyanine on Cu(100)*, ChemPhysChem **10**, 2445 (2009).

List of Publications

T. N. Krauss, E. Barrena, T. Lohmüller, A. Breitling, M. Kelsch, P. A. van Aken, J. P. Spatz, and H. Dosch, *One Dimensional Phthalocyanine Nanostructures Directed by Gold Templates*, Chem. Mater. **DOI:** 10.1021/cm901103f (2009).

List of Symbols

$a, b, c, \alpha, \beta, \gamma$	Parameters of the Unit Cells
a_i, b_i, c_0	Form Factor Interpolation Coefficients
A	Amplitude
A_D	Average Area of the Unit Cell From the Au Nanoparticle Array
A_{eva}	Amplitude of the Evanescent Wave
C_A	Area Correction Factor
C_L	Geometrical Correction Factor in the Integration Volume
C_P	Polarization Correction Factor
d	Lattice Spacing
d_b	Barrier Width Between Tip and Sample
d_{part}	Diameter of the Nanoparticle
D	Film Thickness
D_{Au}	Thickness of the Wetting Layer Surrounding the Au Nanoparticle
E	Energy
E_A	Activation Energy
E_F	Fermi Energy
f	Corrected Atomic Scattering Form Factor
f', f''	Real and Imaginary Part of the Atomic Scattering Form Factor
f_0	Atomic Scattering Form Factor
f_F	Fermi Function
F	Structure Factor
F_z	Normal Force
h, k, l	Miller Indices
\hbar	Planck Constant

List of Symbols

h_j	Thickness/Height of a Box in the Parratt Formalism
I	Scattered Intensity
I_T	Tunneling Current
j	Integer
k_b	Boltzmann Constant
K	Elastic Constant
l	Interparticle Distance
L	Mean Size of the Crystalline Domains
L_I	Island Length
L_s	Length of the Sample
L_z	Size of Crystallites Perpendicular to the Surface
L_{1D}	Length of 1D Structures
m	Mass
M	Total Mass per Unit Area
n	Index of Refraction
N	Integer
N_x, N_y, N_z	Number of Unit Cells
Q	Quality Factor
r	Mean Width of the 1D H ₁₆ CuPc Structures
r_e	Classical Electron Radius
R	Reflectivity
R_j	Reflected Wave Amplitude
s	Slit Size
T_j	Transmitted Wave Amplitude
T_{sub}	Substrate Temperature
V	Voltage
V_b	Potential Barrier
Z	Number of Molecules Within the Unit Cell
$\alpha_r, \beta_r, \gamma_r, \delta_r, \epsilon_r, \zeta_r$	Set of Rotation Angles for the PTCDI-C ₈ Molecule
β_a	Imaginary Part of the Optical Constant
γ_{fs}	Film-Substrate Surface Energy
γ_{fv}	Film-Vacuum Surface Energy
γ_{sv}	Substrate-Vacuum Surface Energy

δ, ϵ	Angular Settings of the Detector
δ_d	Real Part of the Optical Constant
2θ	Angle Between the Incident and Diffracted Beam
θ_{crit}	Critical Angle of Total Reflection
θ_f	Exit Angle
θ_i	Angle of Incidence
θ_{rock}	Rocking Angle
κ	Decay Constant of the Wave Function
λ	Wavelength
Λ	Penetration Depth
μ	Parameter Normalizing the Gaussian Function
μ_a	Mass Attenuation Coefficient
ρ	Electron Density
ϱ	Density
σ	Root Mean Square Roughness
Σ	Surface
τ	Time After Which the Steady Term Dominates the Cantilever Movement
φ_μ, φ_ν	States of the Tip and the Surface
ϕ	Phase
ψ_μ, ψ_ν	Wave Functions of the Unperturbed Sample and Tip
ω	Frequency
ω_0	Resonance Frequency
ω_r	van-der Waals Radius
$\mathbf{a}_x, \mathbf{a}_y, \mathbf{a}_z$	Lattice Vectors in the Three Crystallographic Directions
\mathbf{k}_f	Final Wave Vector
\mathbf{k}_i	Incidence Wave Vector
\mathbf{k}_\parallel	Wave vector Parallel to the Surface
$\mathbf{s}_1, \mathbf{s}_2$	Basis Vectors of the Substrate Unit Cell
\mathbf{q}	Momentum Transfer of the Scattering Process
\mathbf{r}	Position Vector
$\mathbf{m}_1, \mathbf{m}_2$	Basis Vectors of the Monolayer Unit Cell
$M_{\mu\nu}$	Transfer Matrix between States of the Tip and the Surface

List of Symbols

- Δ Rotation Matrix in the δ -Circle
 Ω Rotation Matrix in the ϵ -Circle

References

- [1] R. P. Feynman, *There's plenty of room at the bottom*, Eng. Sci. **23**, 22 (1960).
- [2] G. Binnig, H. Rohrer, Ch. Gerber, and E. Weibel, *Tunneling through a controllable vacuum gap*, Appl. Phys. Lett. **40**, 178 (1982).
- [3] G. Binnig, H. Rohrer, Ch. Gerber, and E. Weibel, *Surface Studies by Scanning Tunneling Microscopy*, Phys. Rev. Lett. **49**, 57 (1982).
- [4] G. Binnig, H. Rohrer, *Scanning tunneling microscopy*, Helv. Phys. Acta **55**, 726 (1982).
- [5] C. W. Tang, *Two-layer organic photovoltaic cell*, Appl. Phys. Lett. **48**, 183 (1986).
- [6] C. W. Tang and S. A. VanSlyke, *Organic electroluminescent diodes*, Appl. Phys. Lett. **51**, 913 (1987).
- [7] A. Tsumura, H. Koezuka, and T. Ando, *Macromolecular electronic device: Field-effect transistor with a polythiophene thin film*, Appl. Phys. Lett. **49**, 1210 (1986).
- [8] F. Yang, M. Shtein, and S. R. Forrest, *Controlled growth of a molecular bulk heterojunction photovoltaic cell*, Nat. Mater. **4**, 37 (2005).
- [9] C. Rost, D. J. Gundlach, S. Karg, and W. Riess, *Ambipolar organic field-effect transistor based on an organic heterostructure*, J. Appl. Phys. **95**, 5782 (2004).
- [10] P. R. L. Malenfant, C. D. Dimitrakopoulos, J. D. Gelorme, L. L. Kosbar, and T. O. Graham, A. Curioni and W. Andreoni, *N-type organic thin film transistor with high field-effect mobility based on a N,N'-dialkyl-3,4,9,10-perylene tetracarboxylic diimide derivative*, Appl. Phys. Lett. **80**, 2517 (2002).

- [11] R. J. Chesterfield, J. C. McKeen, C. R. Newman, P. C. Ewbank, D. A. da Silva Filho, J.-L. Brédas, L. L. Miller, K. R. Mann, and C. D. Frisbie, *Organic Thin Film Transistors Based on N-Alkyl Perylene Diimides: Charge Transport Kinetics as a Function of Gate Voltage and Temperature*, J. Phys. Chem. B **108**, 19281 (2004).
- [12] T. N. Krauss, E. Barrena, D. G. de Oteyza, X. N Zhang, J. Major, V. Dehm, F. Würthner, and H. Dosch, *X-ray/Atomic Force Microscopy Study of the Temperature-Dependent Multilayer Structure of PTCDI-C₈ Films on SiO₂*, J. Phys. Chem. C **113**, 4502 (2009).
- [13] T. N. Krauss, E. Barrena, X. N Zhang, D. G. de Oteyza, J. Major, V. Dehm, F. Würthner, L. P. Cavalcanti, and H. Dosch, *Three-Dimensional Molecular Packing of Thin Organic Films of PTCDI-C₈ Determined by Surface X-ray Diffraction*, Langmuir **24**, 12742 (2008).
- [14] C. W. Struijk, A. B. Sieval, J. E. J. Dakhorst, M. van Dijk, P. Kimkes, R. B. M. Koehorst, H. Donker, T. J. Schaafsma, S. J. Picken, A. M. van de Craats, J. M. Warman, H. Zuilhof, and E. J. R. Sudhölter, *Liquid Crystalline Perylene Diimides: Architecture and Charge Carrier Mobilities*, J. Am. Chem. Soc. **122**, 11057 (2000).
- [15] B. D. Gates, Q. Xu, M. Stewart, D. Ryan, C. G. Wilson, and G. M. Whitesides, *New Approaches to Nanofabrication: Molding, Printing, and Other Techniques*, Chem. Rev. **105**, 1171 (2005).
- [16] J. V. Barth, G. Constantini & K. Kern, *Engineering atomic and molecular nanostructures at surfaces*, Nature **437**, 671 (2005).
- [17] T. N. Krauss, E. Barrena, H. Dosch, and Y. Wakayama, *Supramolecular Assembly of a 2D Binary Network of Pentacene and Phthalocyanine on Cu(100)*, ChemPhysChem **10**, 2445 (2009).
- [18] B. N. Mbenkum, E. Barrena, X. Zhang, M. Kelsch, and H. Dosch, *Selective Growth of Organic 1-D Structures on Au Nanoparticle Arrays*, Nano Lett. **6**, 2852 (2006).
- [19] T. N. Krauss, E. Barrena, T. Lohmüller, A. Breitling, M. Kelsch, P. A. van Aken, J. P. Spatz, and H. Dosch, *One Dimensional Phthalocyanine Nanostructures Directed by Gold Templates*, Chem. Mater. DOI: 10.1021/cm901103f (2009).

-
- [20] A. L. Briseno, S. C. B. Mannsfeld, C. Reese, J. M. Hancock, Y. Xiong, S. A. Jenekhe, Z. Bao, and Y. Xia, *Perylenediimide Nanowires and Their Use in Fabricating Field-Effect Transistors and Complementary Inverters*, *Nano Lett.* **7**, 2847 (2007).
- [21] D. M. Eigler and E. K. Schweizer, *Positioning single atoms with a scanning tunneling microscope*, *Nature* **344**, 524 (1990).
- [22] S. R. Forrest, *The path to ubiquitous and low-cost organic electronic appliances on plastic*, *Nature* **428**, 911 (2004).
- [23] S. Liu, W. M. Wang, A. L. Briseno, S. C. B. Mannsfeld, and Z. Bao, *Controlled Deposition of Crystalline Organic Semiconductors for Field-Effect-Transistor Applications*, *Adv. Mater.* **21**, 1217 (2009).
- [24] H. E. Katz, *Recent Advances in Semiconductor Performance and Printing Processes for Organic Transistor-Based Electronics*, *Chem. Mater.* **16**, 4748 (2004).
- [25] M. E. Gershenson and V. Podzorov, A. F. Morpurgo, *Electronic transport in single-crystal organic transistors*, *Rev. Mod. Phys.* **78**, 973 (2006).
- [26] C. D. Dimitrakopoulos, D. J. Mascaro, *Organic thin-film transistors: A review of recent advances*, *IBM J. Res. & Dev.* **45**, 11 (2001).
- [27] F. Yang, S. R. Forrest, *Photocurrent Generation in Nanostructured Organic Solar Cells*, *ACS Nano* **2**, 1022 (2008).
- [28] P. Y. Bruice, *Essential Organic Chemistry* (Pearson Education, Upper Saddle River, New Jersey, 2006).
- [29] J. A. Venables, *Introduction to Surface and Thin Film Processes* (Cambridge University Press, United Kingdom, 2000).
- [30] J. A. Venables, G. D. T. Spiller and M. Hanbücken, *Nucleation and growth of thin films*, *Rep. Prog. Phys.* **47**, 399 (1984).
- [31] Z. Zhang and M. G. Lagally, *Atomistic Processes in the Early Stages of Thin-Film Growth*, *Science* **276**, 377 (1984).

- [32] E. Bauer, *Phänomenologische Theorie der Kristallabscheidung an Oberflächen*, Z. Kristall. **110**, 372 (1958).
- [33] G. Ehrlich and F. G. Hudda, *Atomic View of Surface Self-Diffusion: Tungsten on Tungsten*, J. Chem. Phys. **44**, 1039 (1966).
- [34] R. L. Schwoebel and E. J. Shipsey, *Step Motion on Crystal Surfaces*, J. Appl. Phys. **37**, 3682 (1966).
- [35] F. Schreiber, *Organic molecular beam deposition: Growth studies beyond the first monolayer*, phys. stat. sol. (a) **201**, 1037 (2004).
- [36] G. Witte and C. Wöll, *Growth of aromatic molecules on solid substrates for applications in organic electronics*, J. Mater. Res. **19**, 1889 (2004).
- [37] G. Hlawacek, P. Puschnig, P. Frank, A. Winkler, C. Ambrosch-Draxl, C. Teichert, *Characterization of Step-Edge Barriers in Organic Thin-Film Growth*, Science **321**, 108 (2008).
- [38] A. C. Dürr, F. Schreiber, M. Münch and N. Karl, B. Krause and V. Kruppa, H. Dosch, *High structural order in thin films of the organic semiconductor diindenoperylene*, Appl. Phys. Lett. **81**, 2276 (2002).
- [39] D. G. de Oteyza, E. Barrena, S. Sellner, J. O. Ossó, and H. Dosch, *Structural Rearrangements During the Initial Growth Stages of Organic Thin Films of F₁₆CuPc on SiO₂*, J. Phys. Chem. B **110**, 16618 (2006).
- [40] H. Yoshida, K. Inaba, N. Sato, *X-ray diffraction reciprocal space mapping study of the thin film phase of pentacene*, Appl. Phys. Lett. **90**, 181930 (2007).
- [41] C. D. Dimitrakopoulos and P. R. L. Malenfant, *Organic Thin Film Transistors for Large Area Electronics*, Adv. Mat. **14**, 99 (2002).
- [42] R. J. Chesterfield, J. C. McKeen, C. R. Newman, and C. D. Frisbie, P. C. Ewbank, K. R. Mann, and L. L. Miller, *Variable temperature film and contact resistance measurements on operating n-channel organic thin film transistors*, J. Appl. Phys. **95**, 6396 (2004).

-
- [43] D. J. Gundlach, K. P. Pernstich, G. Wilckens, M. Grüter, S. Haas, and B. Batlogg, *High mobility n-channel organic thin film transistors and complementary inverters*, J. Appl. Phys. **98**, 064502 (2005).
- [44] S. Tatemichi, M. Ichikawa, T. Koyama, Y. Taniguchi, *High mobility n-type thin-film transistors based on N,N'-ditridecyl perylene diimide with thermal treatments*, Appl. Phys. Lett. **89**, 112108 (2006).
- [45] C. Rolin, K. Vasseur, S. Schols, M. Jouk, G. Duhoux, R. Müller, J. Genoe, and P. Heremans, *High mobility electron-conducting thin-film transistors by organic vapor phase deposition*, Appl. Phys. Lett. **93**, 033305 (2008).
- [46] B. A. Jones, M. J. Ahrens, M.H. Yoon, A. Facchetti, T. J. Marks, and M. R. Wasielewski, *High-Mobility Air-Stable n-Type Semiconductors with Processing Versatility: Dicyanoperylene-3,4:9,10-bis(discarboximides)*, Angew. Chem. Int. Ed. **43**, 6363 (2004).
- [47] J. H. Oh, S. Liu, and Z. Bao, R. Schmidt, and F. Würthner, *Air-stable n-channel organic thin-film transistors with high field-effect mobility based on N,N'-bis(heptafluorobutyl)-3,4:9,10-perylene diimide*, Appl. Phys. Lett. **91**, 212107 (2007).
- [48] R. T. Weitz, K. Amsharov, U. Zschieschang, E. Barrena Villas, D. K. Goswami, M. Burghard, H. Dosch, M. Jansen, K. Kern, and H. Klauk, *Organic n-Channel Transistors Based on Core-Cyanated Perylene Carboxylic Diimide Derivatives*, J. Am. Chem. Soc. **130**, 4637 (2008).
- [49] D. D. Eley, *Phthalocyanines as Semiconductors*, Nature **612**, 816 (1948).
- [50] Z. Bao, A. Lovinger, and A. Dodabalapur, *Organic field-effect transistors with high mobility based on copper phthalocyanine*, Appl. Phys. Lett. **69**, 3066 (1996).
- [51] R. Zeis, T. Siegrist, and Ch. Kloc, *Single-crystal field-effect transistors based on copper phthalocyanine*, Appl. Phys. Lett. **86**, 022103 (2005).
- [52] S. Uchida, J. Xue, B. P. Rand, and S. R. Forrest, *Organic small molecule solar cells with a homogeneously mixed copper phthalocyanine:C₆₀ active layer*, Appl. Phys. Lett. **84**, 4218 (2004).

- [53] P. Sullivan, S. Heutz, S. M. Schultes, and T. S. Jones *Influence of codeposition on the performance of CuPc-C₆₀ heterojunction photovoltaic devices*, Appl. Phys. Lett. **84**, 1210 (2004).
- [54] R. Ye, M. Baba, Y. Oishi, and K. Mori, K. Suzuki, *Air-stable ambipolar organic thin-film transistors based on organic homostructure*, Appl. Phys. Lett. **86**, 253505 (2005).
- [55] J. M. Robertson, *An X-Ray Study of the Structure of the Phthalocyanines. Part I. The Metal-free, Nickel, Copper, and Platinum Compounds.*, J. Chem. Soc. 615 (1935).
- [56] C. J. Brown, *Crystal Structure of β -Copper Phthalocyanine*, J. Chem Soc. (A) 2488 (1968).
- [57] M. Ashida, N. Uyeda, and E. Suito, *Thermal Transformation of Vacuum-Condensed Thin Films of Copper-Phthalocyanine*, J. Cryst. Growth **8**, 45 (1971).
- [58] M. Ashida, N. Uyeda, and E. Suito, *Unit Cell Metastable-form Constants of Various Phthalocyanines*, Bull. Chem. Soc. Jpn. **39**, 2616 (1966).
- [59] R. D. Gould, *Structure and electrical conduction properties of phthalocyanine thin films*, Coord. Chem. Rev. **156**, 237 (1996).
- [60] O. Berger, W.-J. Fischer, B. Adolphi, S. Tierbach, V. Melev, J. Schreiber, *Studies on phase transformations of Cu-phthalocyanine thin films*, J. Mater. Sci.-Mater. Electron. **11**, 331 (2000).
- [61] B. N. Achar and K. S. Lokesh, *Studies on polymorphic modifications of copper phthalocyanine*, J. Solid State Chem. **177**, 1987 (2004).
- [62] Z. Bao, A. J. Lovinger, and J. Brown, *New Air-Stable n-Channel Organic Thin Film Transistors*, J. Am. Chem. Soc. **120**, 207 (1998).
- [63] D. G. de Oteyza and E. Barrena, J. O. Ossó, H. Dosch, S. Meyer and J. Pflaum, *Controlled enhancement of the electron field-effect mobility of F₁₆CuPc thin-film transistors by use of functionalized SiO₂ substrates*, Appl. Phys. Lett. **87**, 183504 (2005).

-
- [64] Y. Oh, S. Pyo, M. H. Yi, S.-K. Kwon, *N-type organic field-effect transistor using polymeric blend gate insulator with controlled surface properties*, *Org. Electron.* **7**, 77 (2006).
- [65] J. Wang, H. Wang, X. Yan, H. Huang, D. Yan, *Organic heterojunction and its application for double channel field-effect transistors*, *Appl. Phys. Lett.* **87**, 093507 (2205).
- [66] J. Wang, H. Wang, X. Yan, H. Huang, D. Jin, J. Shi, Y. Tang, and D. Yan, *Heterojunction Ambipolar Organic Transistors Fabricated by a Two-Step Vacuum-Deposited Process*, *Adv. Funct. Mat.* **16**, 824 (2006).
- [67] H. Wang, J. Wang, X. Yan, J. Shi, H. Tian, Y. Geng, and D. Yan, *Ambipolar organic field-effect transistors with air stability, high mobility, and balanced transport*, *Appl. Phys. Lett.* **88**, 133508 (2006).
- [68] X. Jiang, J. Dai, H. Wang, Y. Geng, D. Yan, *Organic photovoltaic cells using hexadecafluorophthalocyaninatocopper ($F_{16}CuPc$) as electron acceptor material*, *Chem. Phys. Lett.* **446**, 329 (2007).
- [69] J. Dai, X. Jiang, H. Wang, D. Yan, *Organic photovoltaic cell employing organic heterojunction as buffer layer*, *Thin Solid Films* **516**, 3320 (2008).
- [70] R. P. Linstead and J. M. Robertson, *The Stereochemistry of Metallic Phthalocyanines*, *J. Chem. Soc.* 1736 (1936).
- [71] J. O. Ossó, *Growth, Structure, and Optical Properties of Highly Ordered Organic Thin Films of Phthalocyanine and Diindenoperylene*, PhD Thesis (2004).
- [72] D. G. de Oteyza, E. Barrena, J. O. Ossó, S. Sellner, and H. Dosch, *Thickness-Dependent Structural Transitions in Fluorinated Copper-phthalocyanine ($F_{16}CuPc$) Films*, *J. Am. Chem. Soc.* **128**, 15052 (2006).
- [73] J. Zhang, J. Wang, H. Wang, and D. Yan, *Organic thin-film transistors in sandwich configuration*, *Appl. Phys. Lett.* **84**, 142 (2004).
- [74] A. R. Harutyunyan, *Hyperfine structure in the EPR spectra of an organometallic magnet based on doped cobalt phthalocyanine*, *Chem. Phys. Lett.* **246**, 615 (1995).

- [75] X. Chen, Y.-S. Fu, S.-H. Ji, T. Zhang, P. Cheng, X.-C. Ma, X.-L. Zou, W.-H. Duan, J.-F. Jia, and Q.-K. Xue, *Probing Superexchange Interaction in Molecular Magnets by Spin-Flip Spectroscopy and Microscopy*, Phys. Rev. Lett. **101**, 197208 (2008).
- [76] J. Wang, Y. Shi, J. Cao, and R. Wu, *Magnetization and magnetic anisotropy of metallophthalocyanine molecules from the first principles calculations*, Appl. Phys. Lett. **94**, 122502 (2009).
- [77] R. Mason and G. A. Williams, P. E. Fielding, *Structural Chemistry of Phthalocyaninato-cobalt(II) and -manganese(II)*, J. Chem. Soc., Dalton Trans. 676 (1979).
- [78] G. A. Williams and B. N. Figgis, R. Mason, S. A. Mason, P. E. Fielding, *Structure of Phthalocyaninatocobalt(II) at 4.3 K: A Neutron-diffraction Study*, J. Chem. Soc., Dalton Trans. 1688 (1980).
- [79] P. Ballirano, R. Caminiti, C. Ercolani, A. Maras, and M. A. Orrù, *X-ray Powder Diffraction Structure Reinvestigation of the α and β Forms of Cobalt Phthalocyanine and Kinetics of the $\alpha \rightarrow \beta$ Phase Transition*, J. Am. Chem. Soc. **120**, 12798 (1998).
- [80] D. G. de Oteyza, E. Barrena, Y. Zhang, T. N. Krauss, A. Turak, A. Vorobiev, and H. Dosch, *Experimental Relation between Stranski-Krastanov Growth of DIP/ F_{16} CoPc Heterostructures and the Reconstruction of the Organic Interface*, J. Phys. Chem. C **113**, 4234 (2009).
- [81] Y. Y. Lin, D. J. Gundlach, S. F. Nelson, T. N. Jackson, *Pentacene-based organic thin film transistors*, IEEE Trans. Electron Devices **44**, 1325 (1997).
- [82] S. F. Nelson, Y.-Y. Lin, D. J. Gundlach, and T. N. Jackson, *Temperature-independent transport in high-mobility pentacene transistors*, Appl. Phys. Lett. **72**, 1854 (1998).
- [83] R. Ruiz, B. Nickel, N. Koch, L. C. Feldman, R. F. Haglund, A. Kahn, and G. Scoles, *Pentacene ultrathin film formation on reduced and oxidized Si surfaces*, Phys. Rev. B **67**, 125406 (2003).
- [84] R. Ruiz, B. Nickel, N. Koch, L. C. Feldman, R. F. Haglund, Jr., A. Kahn, F. Family, and G. Scoles, *Dynamic Scaling, Island Size Distribution, and Morphology in the*

-
- Aggregation Regime of Submonolayer Pentacene Films*, Phys. Rev. Lett. **91**, 136102 (2003).
- [85] C. C. Mattheus, A. D. Dros, J. Baas, G. T. Oostergetel, A. Meetsma, J. L. de Boer, T. T. M. Palstra, *Identification of polymorphs of pentacene*, Synth. Met. **138**, 475 (2003).
- [86] R. Ruiz, D. Choudhary, B. Nickel, T. Toccoli, K.-C. Chang, A. C. Mayer, P. Clancy, J. M. Blakely, R. L. Headrick, S. Iannotta, and G. G. Malliaras, *Pentacene Thin Film Growth*, Chem. Mat. **16**, 4497 (2004).
- [87] A. C. Mayer, R. Ruiz, R. L. Headrick, A. Kazimirov, G. G. Malliaras, *Early stages of pentacene film growth on silicon dioxide*, Org. Electron. **5** 257 (2004).
- [88] R. Ruiz, A. C. Mayer, and G. G. Malliaras, B. Nickel, and G. Scoles, A. Kazimirov, H. Kim, R. L. Headrick, Z. Islam, *Structure of pentacene thin films*, Appl. Phys. Lett. **85**, 4926 (2004).
- [89] S. E. Fritz, S. M. Martin, C. D. Frisbie, M. D. Ward, and M. F. Toney, *Structural Characterization of a Pentacene Monolayer on an Amorphous SiO₂ Substrate with Grazing Incidence X-ray Diffraction*, J. Am. Chem. Soc. **126**, 4084 (2004).
- [90] S. Schiefer, M. Huth, A. Dobrinevski, and B. Nickel, *Determination of the Crystal Structure of Substrate-Induced Pentacene Polymorphs in Fiber Structured Thin-Films*, J. Am. Chem. Soc. **129**, 10316 (2007).
- [91] R. B. Campbell and J. M. Robertson, and J. Trotter, *The crystal structure of hexacene, and a revision of the crystallographic data for tetracene and pentacene*, Acta Cryst. **15**, 289 (1962).
- [92] W. C. Röntgen, *On A New Kind Of Rays*, Nature **53**, 274 (1896).
- [93] W. Friedrich, P. Knipping und M. Laue, *Interferenzerscheinungen bei Röntgenstrahlen*, Ann. Physik **346**, 971 (1913).
- [94] J. Als-Nielsen, D. McMorrow, *Elements of Modern X-ray Physics* (John-Wiley & Sons, Ltd, Springer, Berlin, Heidelberg, 1992).

- [95] M. Tolan, *X-Ray Scattering from Soft-Matter Thin Films* (Springer, Berlin, 1999).
- [96] H. Dosch, *Critical Phenomena at Surfaces and Interfaces: Evanescent X-ray and Neutron Scattering from thin films and multilayers*, Vol. 126 of Springer Tracts in Modern Physics (Springer, Berlin, Heidelberg, 1992).
- [97] B. E. Warren, *X-ray diffraction* (Dover Publications, inc, 1990).
- [98] U. Pietsch, V. Holý, and T. Baumbach, *High-Resolution X-Ray Scattering: From Thin Films to Lateral Nanostructures* (Springer, Berlin, 2004).
- [99] R. Feidenhans'l, *Surface Structure Determination By X-ray Diffraction*, Surf. Sci. Rep. **10**, 105 (1989).
- [100] J. A. Ibers and W. C. Hamilton eds., *International Tables of X-Ray Crystallography* (Kynoch Press, Birmingham, 1974); atomic scattering factors are in Vol. IV, chapter 2.2, by D.T. Cromer and J.T. Waber.
- [101] L. G. Parratt, *Surface Studies of Solids by Total Reflection of X-rays*, Phys. Rev. **95**, 359 (1954).
- [102] G. Binnig, H. Rohrer, Ch. Gerber, and E. Weibel, *7×7 Reconstruction on Si(111) Resolved in Real Space*, **50**, 120 (1983).
- [103] G. Binnig and H. Rohrer, *Scanning Tunneling Microscopy*, Surf. Sci. **126**, 236 (1983).
- [104] J. Tersoff and D. R. Hamann, *Theory and Application for the Scanning Tunneling Microscope*, Phys. Rev. Lett. **50**, 1998 (1983).
- [105] J. Tersoff and D. R. Hamann, *Theory of the scanning tunneling microscope*, Phys. Rev. B **31**, 805 (1985).
- [106] J. Bardeen, *Tunneling From A Many-Particle Point Of View*, Phys. Rev. Lett. **6**, 57 (1961).
- [107] C. J. Chen, *Introduction to Scanning Tunneling Microscopy* (Oxford University Press, New York, 1993).

-
- [108] G. Binnig, and C. F. Quate and Ch. Gerber, *Atomic Force Microscope*, Phys. Rev. Lett. **56**, 930 (1986).
- [109] B. Bhushan, *Handbook of Nanotechnology* (Springer, Heidelberg, 2004).
- [110] F. Moreno-Herrero, and P. J. de Pablo, R. Fernández-Sánchez, J. Colchero, J. Gómez-Herrero, and A. M. Baró, *Scanning force microscopy jumping and tapping modes in liquids*, Appl. Phys. Lett. **81**, 2620 (2002).
- [111] Y. Martin, C. C. Williams, and H. K. Wickramasinghe, *Atomic force microscopy-force mapping and profiling on a sub 100-Å scale*, J. Appl. Phys. **61**, 4723 (1987).
- [112] T. R. Albrecht, P. Grütter, D. Horne, and D. Rugar, *Frequency modulation detection using high-Q cantilevers for enhanced force microscope sensitivity*, J. Appl. Phys. **69**, 668 (1991).
- [113] Q. Zhong, D. Inniss, K. Kjoller and V. B. Elings, *Fractured polymer/silica fiber surface studied by tapping mode atomic force microscopy*, Surf. Sci. **290**, L688 (1993).
- [114] P. K. Hansma, J. P. Cleveland, M. Radmacher, D. A. Walters, P. E. Hillner, M. Bezanilla, M. Fritz, D. Vie, and H. G. Hansma, C.B. Prater, J. Massie, L. Fukunaga, J. Gurley, and V. Elings, *Tapping mode atomic force microscopy in liquids*, Appl. Phys. Lett. **64**, 1738 (1994).
- [115] C. A. J. Putman, K. O. Van der Werf, B. G. De Groot, N. F. Van Hulst, and J. Greve, *Tapping mode atomic force microscopy in liquid*, Appl. Phys. Lett. **64**, 2454 (1994).
- [116] L. de Broglie, *Recherches sur la théorie des quanta*, PhD Thesis (1924).
- [117] M. Knoll und E. Ruska, *Beitrag zur geometrischen Elektronenoptik. I*, Ann. Physik **12**, 607 (1932).
- [118] M. Knoll und E. Ruska, *Beitrag zur geometrischen Elektronenoptik. II*, Ann. Physik **12**, 641 (1932).
- [119] M. v. Heimendahl, *Einführung in die Elektronenmikroskopie* (Vieweg, Braunschweig, 1970).

- [120] D. B. Williams and C. B. Carter, *Transmission Electron Microscopy* (Plenum Press, New York, 1996).
- [121] P. F. Schmid, *Praxis der Rasterelektronenmikroskopie und Mikrobereichsanalyse* (expert verlag, Renningen-Malmsheim, 1994).
- [122] D. Brandon and W. D. Kaplan, *Microstructural Characterization of Materials* (Wiley, London, 2001).
- [123] J. P. Le Poole, *New electron microscope with continuously variable magnification*, Philips techn. Rdsch. **9**, 33 (1947).
- [124] R. Glass, M. Arnold, J. Blümmel, A. Küller, M. Möller, and J. P. Spatz, *Micro-Nanostructured Interfaces Fabricated by the Use of Inorganic Block Copolymer Micellar Monolayers as Negative Resist for Electron-Beam Lithography*, Adv. Funct. Mat. **13**, 569 (2003).
- [125] R. Glass, M. Möller and J. P. Spatz, *Block copolymer micelle nanolithography*, Nanotechnology **14**, 1153 (2003).
- [126] T. Lohmüller, E. Bock, and J. P. Spatz, *Synthesis of Quasi-Hexagonal Ordered Arrays of Metallic Nanoparticles with Tuneable Particle Size*, Adv. Mater. **20**, 2297 (2008).
- [127] T. Lohmüller, M. Helgert, M. Sundermann, R. Brunner, and J. P. Spatz, *Biomimetic Interfaces for High-Performance Optics in the Deep-UV Light Range*, Nano Lett. **8**, 1429 (2008).
- [128] I. Haller, M. Hatzakis, R. Srinivasan, *High-resolution Positive Resists for Electron-Beam Exposure*, IBM J. Res. Develop. **12**, 251 (1968).
- [129] B. Krause, *Growth and Structure of the Organic Molecule PTCDA on Ag(111)*, PhD Thesis (2002).
- [130] I. Horcas, and R. Fernández, J. M. Gómez-Rodríguez, J. Colchero, J. Gómez-Herrero, A. M. Baro, *WSXM: A software for scanning probe microscopy and a tool for nanotechnology*, Rev. Sci. Instrum. **78**, 013705 (2007).

-
- [131] A. C. Dürr, N. Koch, M. Kelsch, A. Rühm, J. Ghijsen, R. L. Johnson, J.-J. Pireaux, J. Schwartz, F. Schreiber, H. Dosch, and A. Kahn, *Interplay between morphology, structure, and electronic properties at diindenoperlyene-gold interfaces*, Phys. Rev. B **68**, 115428 (2003).
- [132] H. Yang, T. J. Shin, M.-M. Ling, K. Cho, C. Y. Ryu, and Z. Bao, *Conducting AFM and 2D GIXD Studies on Pentacene Thin Films*, J. Am. Chem. Soc. **127**, 11542(2005).
- [133] D. Nabok, P. Putschnig, and C. Ambrosch-Draxl, O. Werzer, and R. Resel, D.-M. Smilgies, *Crystal and electronic structure of pentacene thin films from grazing incidence x-ray diffraction and first-principles calculations*, Phys. Rev. B **76**, 235322 (2007).
- [134] Q. Yuan, S. C. B. Mannsfeld, M. L. Tang, M. F. Tooney, J. Luning, and Z. Bao, *Thin Film Structure of Tetraceno[2,3-b]thiophene Characterized by Grazing Incidence Xray Scattering and Near-Edge X-ray Absorption Fine Structure Analysis*, J. Am. Chem. Soc. **130**, 3502 (2008).
- [135] Q. Yuan, S. C. B. Mannsfeld, M. L. Tang, M. Roberts, M. F. Tooney, D. M. DeLongchamp, and Z. Bao, *Microstructure of Oligofluorene Asymmetric Derivatives in Organic Thin Film Transistors*, Chem. Mater. **20**, 2763 (2008).
- [136] Superfit program based on the Parratt formalism downloadable from the following web page: http://www.mf.mpg.de/en/abteilungen/dosch/software/software_en.shtml.
- [137] J. T. Sadowski, G. Sazaki, S. Nishikata, A. Al-Mahboob, Y. Fujikawa, K. Nakajima, R. M. Tromp, and T. Sakurai, *Single-Nucleus Polycrystallization in Thin Film Epitaxial Growth*, Phys. Rev. Lett. **98**, 046104 (2007).
- [138] V. Kalihari, E. B. Tadmor, G. Haugstad, and C. D. Frisbie, *Grain Orientation Mapping of Polycrystalline Organic Semiconductor Films by Transverse Shear Microscopy*, Adv. Mater. **20**, 4033 (2008).
- [139] K. Doi, K. Yoshida, H. Nakano, and A. Tachibana, T. Tanabe, Y. Kojima and

- K. Okazaki, *Ab initio calculation of electron effective masses in solid pentacene*, J. Appl. Phys. **98**, 113709 (2005).
- [140] P. Parisse, L. Ottaviano, B. Delley and S. Picozzi, *First-principles approach to the electronic structure in the pentacene thin film polymorph*, J. Phys.:Condens. Matter **19**, 106209 (2007).
- [141] F. Würthner and R. Schmidt, *Electronic and Crystal Engineering of Acenes for Solution-Processible Self-Assembling Organic Semiconductors*, ChemPhysChem **7**, 793 (2006).
- [142] E. Vlieg, *Integrated Intensities Using a Six-Circle Surface X-ray Diffractometer*, J. Appl. Cryst. **30**, 532 (1997).
- [143] D.-M. Smilgies, *Geometry-independent intensity correction factors for grazing-incidence diffraction*, Rev. Sci. Instrum. **73**, 1706 (2002).
- [144] E. Hädicke and F. Graser, *Structures of Eleven Perylene-3,4:9,10-bis(dicarboximide) Pigments*, Acta Cryst. **C42**, 189 (1986).
- [145] E. Hädicke and F. Graser, *Structures of Three Perylene-3,4:9,10-bis(dicarboximide) Pigments*, Acta Cryst. **C42**, 195 (1986).
- [146] G. Klebe, F. Graser, E. Hädicke and J. Berndt, *Crystallochromy as a Solid-State Effect: Correlation of Molecular Conformation, Crystal Packing and Colour in Perylene-3,4:9,10-bis(dicarboximide) Pigments*, Acta Cryst. **B45**, 69 (1989).
- [147] T. N. Krauss, *Structure and Morphology of Organic Films of PTCDI-C₈ on Silicon Dioxide*, Diplomarbeit (2006).
- [148] S. De Feyter and F. C. De Schryver, *Two-dimensional supramolecular self-assembly probed by scanning tunneling microscopy*, Chem. Soc. Rev. **32**, 139 (2003).
- [149] J. V. Barth *Molecular Architectonic on Metal Surfaces*, Annu. Rev. Phys. Chem. **58**, 375 (2007).
- [150] M. Stöhr, M. Wahl, C. H. Galka, T. Riehm, T. A. Jung, and L. H. Gade, *Controlling Molecular Assembly in Two Dimensions: The Concentration Dependence of*

-
- Thermally Induced 2D Aggregation of Molecules on a Metal Surface*, *Angew. Chem. Int. Ed.* **44**, 7394 (2005).
- [151] Y. Wang, M. Alcamí, and F. Martín, *Understanding the Supramolecular Self-Assembly of the Fullerene PCBM on Gold Surfaces*, *ChemPhysChem* **9**, 1030 (2008).
- [152] J. Méndez, R. Caillard, G. Otero, N. Nicoara, and J. A. Martín-Gago, *Nanostructured Organic Material: From Molecular Chains to Organic Nanodots*, *Adv. Mater.* **18**, 2048 (2006).
- [153] M. Böhringer, K. Morgenstern, and W.-D. Schneider, R. Berndt, F. Mauri, A. De Vita, and R. Car, *Two-Dimensional Self-Assembly of Supramolecular Clusters and Chains*, *Phys. Rev. Lett.* **83**, 324 (1999).
- [154] J. V. Barth, J. Weckesser, C. Cai, P. Günter, L. Bürgi, O. Jeandupeux, and K. Kern, *Building Supramolecular Nanostructures at Surfaces by Hydrogen Bonding*, *Angew. Chem. Int. Ed.* **39**, 1230 (2000).
- [155] D. Bonifazi, H. Spillmann, A. Kiebele, M. de Wild, P. Seiler, F. Cheng, H.-J. Güntherodt, T. Jung, and F. Diederich, *Supramolecular Patterned Surfaces Driven by Cooperative Assembly of C₆₀ and Porphyrins on Metal Substrates*, *Angew. Chem. Int. Ed.* **43**, 4759 (2004).
- [156] B. Xu, C. Tao, E. D. Williams, and J. E. Reutt-Robey, *Coverage Dependent Supramolecular Structures: C₆₀:ACA Monolayers on Ag(111)*, *J. Am. Chem. Soc.* **128**, 8493 (2006).
- [157] E. Barrena, D. G. de Oteyza, H. Dosch, and Y. Wakayama, *2D Supramolecular Self-Assembly of Binary Organic Monolayers*, *ChemPhysChem* **8**, 1915 (2007).
- [158] E. Mena-Osteritz and P. Bäuerle, *Complexation of C₆₀ on a Cyclothiophene Monolayer Template*, *Adv. Mater.* **18**, 447 (2006).
- [159] P. A. Staniec, L. M. A. Perdigão, A. Saywell, N. R. Champness, and P. H. Beton, *Hierarchical Organisation on a Two-Dimensional Supramolecular Network*, *ChemPhysChem* **8**, 2177 (2007).

- [160] K. W. Hipps, L. Scudiero, D. E. Barlow, and M. P. Cooke, Jr., *A Self-Organized 2-Dimensional Bifunctional Structure Formed by Supramolecular Design*, J. Am. Chem. Soc. **124**, 2126 (2002).
- [161] C. Bobisch, Th. Wagner, A. Bannani, and R. Möller, *Ordered binary monolayer composed of two organic molecules: Copper-phthalocyanine and 3,4,9,10-perylene-tetra-carboxylic-dianhydride on Cu(111)*, J. Chem. Phys. **119**, 9804 (2003).
- [162] W. Chen, H. Li, H. Huang, Y. Fu, H. L. Zhang, J. Ma, and A. T. S. Wee, *Two-Dimensional Pentacene:3,4,9,10-Perylenetetracarboxylic Dianhydride Supramolecular Chiral Networks on Ag(111)*, J. Am. Chem. Soc. **130**, 12285 (2008).
- [163] L. Scudiero, K. W. Hipps, and D. E. Barlow, *A Self-Organized Two-Dimensional Bimolecular Structure*, J. Phys. Chem. B **107**, 2903 (2003).
- [164] S. Yoshimoto, Y. Honda, O. Ito, and K. Itaya, *Supramolecular Pattern of Fullerene on 2D Bimolecular "Chessboard" Consisting of Bottom-up Assembly of Porphyrin and Phthalocyanine Molecules*, J. Am. Chem. Soc. **130**, 1085 (2008).
- [165] J.-M. Lehn, *Toward Self-Organization and Complex Matter*, Science **295**, 2400 (2002).
- [166] G. M. Whitesides and B. Grzybowski, *Self-Assembly at All Scales*, Science **295**, 2418 (2002).
- [167] S. Hecht, *Welding, Organizing, and Planting Organic Molecules on Substrate Surfaces - Promising Approaches towards Nanoarchitectonics from the Bottom up*, Angew. Chem. Int. Ed. **42**, 24 (2003).
- [168] P. Samorí, N. Severin, C. D. Simpson, K. Müllen, and J. P. Rabe, *Epitaxial Composite Layers of Electron Donors and Acceptors from Very Large Polycyclic Aromatic Hydrocarbons*, J. Am. Chem. Soc. **124**, 9454 (2002).
- [169] J. A. Theobald, N. S. Oxtoby, M. A. Phillips, N. R. Champness & P. H. Beton, *Controlling molecular deposition and layer structure with supramolecular surface assemblies*, Nature **424**, 1029 (2003).

-
- [170] S. Stepanow, M. Lingenfelder, A. Dmitriev, H. Spillmann, E. Delvigne, N. Lin, X. Deng, C. Cai, J. V. Barth and K. Kern, *Steering molecular organization and host-guest interactions using two-dimensional nanoporous coordination systems*, Nat. Mater. **3**, 229 (2004).
- [171] H. Spillmann, A. Kiebele, M. Stöhr, T. A. Jung, D. Bonifazi, F. Cheng, and F. Diederich, *A Two-Dimensional Porphyrin-Based Porous Network Featuring Communicating Cavities for the Templated Complexation of Fullerenes*, Adv. Mater. **18**, 275 (2006).
- [172] B. Calmettes, S. Nagarajan, A. Gourdon, M. Abel, L. Porte, and R. Coratger, *Bicomponent Supramolecular Packing in Flexible Phthalocyanine Networks*, Angew. Chem. Int. Ed. **47**, 6994 (2008).
- [173] M. Treier, M.-T. Nguyen, N. V. Richardson, C. Pignedoli, D. Passerone, and R. Fasel, *Tailoring Low-Dimensional Organic Semiconductor Nanostructures*, Nano Lett. **9**, 126 (2009).
- [174] Q. Chen, A. J. McDowall, and N. V. Richardson, *Ordered Structures of Tetracene and Pentacene on Cu(110) Surfaces*, Langmuir **19**, 10164 (2003).
- [175] S. Lukas, S. Söhnchen, G. Witte, and C. Wöll, *Epitaxial Growth of Pentacene Films on Metal Surfaces*, ChemPhysChem **5**, 266 (2004).
- [176] S. Söhnchen, S. Lukas, and G. Witte, *Epitaxial growth of pentacene films on Cu(110)*, J. Chem. Phys. **121**, 525 (2004).
- [177] S. Söhnchen, K. Hänel, A. Birkner, G. Witte, and C. Wöll, *Molecular Beam Deposition of Perylene on Copper: Formation of Ordered Phases*, Chem. Mater. **17**, 5297 (2005).
- [178] Y. Wakayama, *Assembly Process and Epitaxy of the F₁₆CuPc Monolayer on Cu(111)*, J. Phys. Chem C **111**, 2675 (2007).
- [179] P. G. Schroeder, C. B. France, J. B. Park, and B. A. Parkinson, *Energy level alignment and two-dimensional structure of pentacene on Au(111) surfaces*, J. Appl. Phys. **91**, 3010 (2002).

- [180] C. B. France, P. G. Schroeder, and B. A. Parkinson, *Direct Observation of a Widely Spaced Periodic Row Structure at the Pentacene/Au(111) Interface Using Scanning Tunneling Microscopy*, Nano Lett. **2**, 693, 2002.
- [181] J. H. Kang and X.-Y. Zhu, *Pi-stacked pentacene thin films grown on Au(111)*, Appl. Phys. Lett. **82**, 3248 (2003).
- [182] O. McDonald, A. A. Cofalla, D. Carty, G. Sheerin, G. Hughes, *Photoemission, NEXAFS and STM studies of pentacene thin films on Au(100)*, Surf. Sci. **600**, 3217 (2006).
- [183] A. Ferretti, C. Baldacchini, A. Calzolari, R. Di Felice, A. Ruini, E. Molinari, and M. G. Betti, *Mixing of Electronic States in Pentacene Adsorption on Copper*, Phys. Rev. Lett. **99**, 046802 (2007).
- [184] M. Satta, S. Iacobucci, and R. Larciprete, *Molecular adsorption and multilayer growth of pentacene on Cu(100): Layer structure and energetics*, Phys. Rev. B **75**, 155401 (2007).
- [185] D. G. de Oteyza, J. M. García-Lastra, M. Corso, B. P. Doyle, L. Floreano, A. Morgante, Y. Wakayama, A. Rubio, and J. E. Ortega, submitted.
- [186] H. Huang, W. Chen, and A. T. S. Wee, *Low-Temperature Scanning Tunneling Microscopy Investigation of Epitaxial Growth of F₁₆CuPc Thin Films on Ag(111)*, J. Phys. Chem. C **112**, 14913 (2008).
- [187] T. Samuely, S.-X. Liu, N. Wintjes, M. Haas, S. Decurtins, T. A. Jung and M. Stöhr, *Two-Dimensional Multiphase Behavior Induced by Sterically Hindered Conformational Optimization of Phenoxy-Substituted Phthalocyanines*, J. Phys. Chem. C. **112**, 6139 (2008).
- [188] V. R. Thalladi, H.-C. Weiss, D. Bläser, R. Boese, A. Nangia, and G. R. Desiraju, *C-H...F Interactions in the Crystal Structures of Some Fluorobenzenes*, J. Am. Chem. Soc. **120**, 8702 (1998).
- [189] A. DerHovanessian, J. B. Doyon, A. Jain, P. R. Rablen, and A.-M. Sapse, *Models of F-H Contacts Relevant to the Binding of Fluoroaromatic Inhibitors to Carbonic Anhydrase II*, Org. Lett. **1**, 1359 (1999).

-
- [190] D. G. de Oteyza, I. Silanes, M. Ruiz-Osés, E. Barrena, B. P. Doyle, A. Arnau, H. Dosch, Y. Wakayama, and J. E. Ortega, *Balancing Intermolecular and Molecule-Substrate Interactions in Supramolecular Assemblies*, *Adv. Funct. Mater.* **19**, 259 (2009).
- [191] A. Scheybal, K. Müller, R. Berschinger, M. Wahl, A. Bendounan, P. Aebi, and T. A. Jung, *Modification of the Cu(110) Shockley surface state by an adsorbed pentacene monolayer*, *Phys. Rev. B* **79**, 115406 (2009).
- [192] L. Kilian, A. Hauschild, R. Temirov, S. Soubatch, A. Schöll, A. Bendounan, F. Reinert, T.-L. Lee, F. S. Tautz, M. Sokolowski, and E. Umbach, *Role of Intermolecular Interactions on the Electronic and Geometric Structure of a Large π -Conjugated Molecule Adsorbed on a Metal Surface*, *Phys. Rev. Lett.* **100**, 136103 (2008).
- [193] S. Ju, K. Lee, and D. B. Janes, M.-Y. Yoon, A. Facchetti, and T. J. Marks, *Low Operating Single ZnO Nanowire Field-Effect Transistors Enabled by Self-Assembled Organic Nanodielectrics* *Nano Lett.* **5**, 2281 (2005).
- [194] H. Klauk, *Nanowires' display of potential*, *Nature* **451**, 533 (2008).
- [195] Q. Tang, H. Li, Y. Liu, and W. Hu, *High-Performance Air-Stable n-Type Transistors with an Asymmetrical Device Configuration Based on Organic Single-Crystalline Submicrometer/Nanometer Ribbons*, *J. Am. Chem. Soc.* **128**, 14634 (2006).
- [196] Q. Tang, H. Li, Y. Song, W. Xu, W. Hu, L. Jiang, Y. Liu, X. Wang, and D. Zhu, *In Situ Patterning of Organic Single-Crystalline Nanoribbons on a SiO₂ Surface for the Fabrication of Various Architectures and High-Quality Transistors*, *Adv. Mater.* **18**, 3010 (2006).
- [197] A. L. Briseno, S. C. B. Mannsfeld, S. A. Jenekhe, Z. Bao, and Y. Xia, *Introducing organic nanowire transistors*, *Mater. Today* **11**, 38 (2008).
- [198] Y. Yamamoto, T. Fukushima, Y. Suna, N. Ishii, A. Saeki, S. Seki, S. Tagawa, M. Taniguchi, T. Kawai, T. Aida, *Photoconductive Coaxial Nanotubes of Molecularly Connected Electron Donor and Acceptor Layers*, *Science* **314**, 1761 (2006).

- [199] K. Balakrishnan, A. Datar, R. Oitker, H. Chen, J. Zuo, and L. Zang, *Nanobelt Self-Assembly from an Organic n-Type Semiconductor: Propoxyethyl-PTCDI*, J. Am. Chem. Soc. **127**, 10496 (2005).
- [200] W. Y. Tong, A. B. Djurišić, M. H. Xie, A. C. M. Ng, and K. Y. Cheung, W. K. Chan and Y. H. Leung, H. W. Lin and S. Gwo, *Metal Phthalocyanine Nanoribbons and Nanowires*, J. Phys. Chem. B **110**, 17406 (2006).
- [201] S. Karan and B. Mallik, *Templating Effects and Optical Characterization of Copper (II) Phthalocyanine Nanocrystallites Thin Film: Nanoparticles, Nanoflowers, Nanocabbages, and Nanoribbons*, J. Phys. Chem. C **111**, 7352 (2007).
- [202] C. C. Leznoff, A. B. P. Lever, *Phthalocyanines: Properties and Applications, Vol. 4* (VCH Publishers, Inc. USA, 1996).
- [203] G. Koller, S. Berkebile, J. R. Krenn, G. Tzvetkov, G. Hlawacek, O. Lengyel, F. P. Netzer, C. Teichert, R. Resel, and M. G. Ramsey, *Oriented Sexiphenyl Single Crystal Nanoneedles on TiO₂ (110)*, Adv. Mater. **16**, 2159 (2004).
- [204] E. Barrena, X. N. Zhang, B. N Mbenkum, T. Lohmueller, T. N. Krauss, M. Kelsch, P. A. van Aken, J. P. Spatz, and H. Dosch, *Self-Assembly of Phthalocyanine Nanotubes by Vapor-Phase Transport*, ChemPhysChem **9**, 1114 (2008).
- [205] D. Käfer, L. Ruppel, and G. Witte, *Growth of pentacene on clean and modified gold surfaces*, Phys. Rev. B **75**, 085309 (2007).
- [206] I. Biswas, H. Peisert, M. Nagel, and M. B. Casu, S. Schuppler and P. Nagel, E. Pellgrin, T. Chassé, *Buried interfacial layer of highly oriented molecules in copper phthalocyanine thin films on polycrystalline gold*, J. Chem. Phys. **126**, 174704 (2007).
- [207] D.-J. Liu, R. L. Blumberg Selinger, and J. D. Weeks, *Representing molecular shape and interactions: A reduced intermolecular potential for copper phthalocyanine*, J. Chem. Phys. **105**, 4751 (1996).

Danksagung

Das Gelingen dieser Arbeit war nur durch die Mithilfe und Unterstützung mehrerer Personen möglich, bei denen ich mich herzlich bedanken möchte.

Die zwei Personen, ohne die diese Arbeit nicht zustande gekommen wäre und die ich speziell hervorheben möchte, sind Frau **Dr. Esther Barrena** und Herr **Prof. Dr. Helmut Dosch**. Esthers positive Ausstrahlung hat mir geholfen, so manche schwere Hürden zu nehmen und immer neue Motivation zu liefern. Dank ihr war die Stimmung und die Atmosphäre innerhalb der Gruppe immer gut und es machte viel Spaß, mit ihr zusammen zu arbeiten. Menschlich wie auch fachlich konnte ich sehr viel von ihr lernen, was auch für Herrn Dosch gilt, der mir die Möglichkeit gab, in seiner herzlichen Abteilung aufgenommen zu werden und diese Doktorarbeit durchzuführen. Für die finanzielle Unterstützung wie auch für die Bereitstellung der exzellenten experimentellen Bedingungen möchte ich mich bei ihm bedanken. Seine stets offene Art und Hilfsbereitschaft sei hier noch extra zu bemerken.

Herrn **Prof. Dr. Jörg Wrachtrup** danke ich für die Übernahme des Mitberichts sowie Herrn **Prof. Dr. Manfred Rühle** für die problemlose Weiterführung der Abteilung.

Bei **Dr. Yutaka Wakayama**, der mir einen unvergesslichen Forschungsaufenthalt in Japan ermöglichte, möchte ich mich ebenfalls bedanken. Nicht nur die hervorragenden experimentellen Voraussetzungen am National Institute for Materials Science, sondern auch die kulturellen (Tokio, Kyoto, Sumo-Ringen, ...) wie auch kulinarischen (Yakitori, Tempura, Asahi, ...) Erfahrungen werden mir immer im Gedächtnis bleiben. In diesem Zusammenhang möchte ich auch der Japan Society for the Promotion of Science für die finanzielle Unterstützung danken.

Herrn **Dr. János Major** und **Dr. Mélissa Delheusy** bin ich sehr dankbar für die Lösung vieler offener Programmierfragen. Ohne die Hilfe von **Dr. Theobald Lohmüller**

und der Kollaboration mit der Abteilung von Herrn **Prof. Dr. Joachim Spatz**, wäre ein Großteil der Probenherstellung nicht möglich gewesen. **Marion Kelsch** sowie Frau **Dr. Yun Jin-Phillipp** danke ich herzlich für die produktive wie auch nette Zusammenarbeit im Rahmen einer Kollaboration mit dem Stuttgarter Zentrum für Elektronenmikroskopie unter der Leitung von **PD Dr. Peter van Aken**.

Für die exzellente technische Unterstützung möchte ich mich bei **Taufan Zimmer**, **Ralf Weigel**, **Frank Adams**, **Annette Weisshardt**, **Ioannis Grigoris** und **Maria Sycha** bedanken.

Ein ganz besonderer Dank gilt den Arbeitskollegen der organischen Dünnschichtgruppe. **Dr. Dimas Garcia de Oteyza Feldermann** danke ich für die zahlreichen Diskussionen und wertvollen Tipps, **Dr. Xue Na Zhang** für die Beantwortung vieler Fragen und für die schöne Zeit als Zimmerkollegen. Bei **Dr. Carmen Munuera** bedanke ich mich für die Beantwortung zahlreicher Fragen rund um das AFM sowie für die ‘perfekte’ Navigation bei diversen Konferenzen. **Felix Maye** möchte ich meinen Dank aussprechen für das Korrekturlesen der deutschen Zusammenfassung. Ohne die tatkräftige Mithilfe von (in alphabetischer Reihenfolge) **Dr. Dipak Goswami**, **Jonathan Heidkamp**, **Peter Lienerth**, **Minh Nguyen**, **Ajay Perumal**, **Markos Paradinas**, **Monamie Sanyal**, **Dr. Claudia Sorg**, **Dr. Ayse Turak** und **Dr. Yi Zhang** auf Strahlzeiten, bei Arbeiten im Labor, an der OMBE oder am AFM wären viele dieser Ergebnisse nicht zustande gekommen. Der ganzen Gruppe möchte ich für die Unterstützung und der schönen Zeit (nicht nur während der Arbeit) danken.

Schließlich bedanke ich mich bei der **ganzen Abteilung**, die mich freundlich aufgenommen hat und in der es Spaß machte, zu arbeiten.

Mein größter Dank gilt **Ana** und **meinen Eltern**, die mir das nötige Vertrauen entgegengebracht und mich immer in all den Jahren tatkräftig unterstützt haben.